Title

Functionalized Mesoporous Silica Nanoparticles and their Applications in Drug Delivery and Magnetic Resonance Imaging Contrast Enhancement

Author

Deng, Tian

Publication Date

2021

Peer reviewed|Thesis/dissertation

UNIVERSITY OF CALIFORNIA

Los Angeles

Functionalized Mesoporous Silica Nanoparticles and their Applications in Drug Delivery and Magnetic Resonance Imaging Contrast Enhancement

A dissertation submitted in partial satisfaction of the

requirements for the degree Doctor of Philosophy

in Chemistry

by

Tian Deng

2021

ABSTRACT OF THE DISSERTATION

Functionalized Mesoporous Silica Nanoparticles and their Applications in Drug Delivery and Magnetic Resonance Imaging Contrast Enhancement

by

Tian Deng

Doctor of Philosophy in Chemistry

University of California, Los Angeles, 2021

Professor Jeffrey I. Zink, Chair

This dissertation makes contributions to the fields of functionalized mesoporous silica nanoparticles (MSNs) designed for magnetic resonance imaging (MRI) contrast enhancement and high-intensity focused ultrasound (HIFU) triggered cargo release. MRI-guided HIFU (MRIgHIFU) has been applied as a therapeutic tool in the clinic, and enhanced MRI contrast will improve the precision and applicability of HIFU therapy. In Chapter 2, the ultrasound responsive MSNs carriers are reviewed. In Chapter 3, the proof-of-concept spotlight technique based on MRIgHIFU and MSNs is introduced. With periodic HIFU modulation, the functionalized MSNs generated reversible MRI T_1 relaxivity changes at the 1.5 mm^3 focal point. Fourier analysis was used to

extract signal changes at the modulation frequency, and a modulation enhancement map spotlights the precise region of interest by increasing contrast almost 100-fold. In Chapter 4, another functionalized MSNs were designed for the spotlight technique, and the spectral analysis was further studied to maximize the contrast enhancement. In particular, a framework was presented to analyze the trade-offs between different parameter choices for the signal processing method. In Chapter 5, the application of the spotlight technique was demonstrated at human body temperature. The MSNs were functionalized with the tailored poly(2-oxazoline)s with a lower critical solution temperature (LCST) at 40 °C, so that it could generate reversible MRI contrast change at human body temperature. The temperature oscillation range was small (3 °C), and the data acquisition was relatively fast (in 100 s), which made it a step closer to the biomedical applications in the clinic. The HIFU-responsive cargo delivery was studied in Chapters 6 and 7. The large pore MSNs (LPMSNs) were studied as the nanocarriers to load a large drug molecule, Docetaxel. With the loading procedure and HIFU parameters tuned, the HIFU-responsive release was demonstrated in a biologically relevant solvent. HIFU-responsive MRI contrast agent delivery was studied using MSNs capped with thermo-responsive polymer. The cargo loading and release conditions were optimized, and the HIFU-responsive cargo release can be monitored by MRI contrast change. The spotlight technique in this dissertation is promising for biomedical applications of precision therapy. The framework on parameter choice and demonstrated MRI contrast enhancement at human body temperature provides the foundation for further clinical translation.

The dissertation of Tian Deng is approved.

Holden H. Wu

Ellen May Sletten

Xiangfeng Duan

Jeffrey I. Zink, Committee Chair

University of California, Los Angeles

2021

TABLE OF CONTENTS

LIST OF FIGURES

LIST OF SUPPORTING FIGURES

LIST OF SCHEMES

LIST OF TABLES

LIST OF SUPPORTING TABLES

ACKNOWLEDGEMENT

I always feel blessed to have so many people supporting me in graduate school, and I would like to acknowledge all of you here.

First of all, I would like to acknowledge my research advisor, Professor Jeffrey I. Zink. I am so lucky to have had the opportunity to learn from him and work in his great lab in the past 5 years. I admire his life-long enthusiasm about science, and it is cheerful to share his passion in the daily work. Also, I am deeply respectful of his dedication to develop and advance cutting-edge science and technology, and I find him a role model for my future career. Besides, he is always patient and supportive to me throughout these 5 years. He opens so many opportunities so that I can dive into research I am interested in. I have learned so much from him, not only about science, but also about how to work with a team, how to manage a project, and how to be a kind mentor.

I would also like to thank my laboratory colleagues. I would like to thank all my mentors: Dr. Zilu Li, Dr. Bastian Ruehle, Dr. Philippe Saint-Cricq, Dr. Ruining Wang, Dr. Chia-Jung Yu, Dr. Sheba Plamthottam, Professor Qilin Yu, Professor Liping Ruan, Professor Xiaojie Ju, and Professor Changli Zhang. I really appreciate the help they offered to me generously when I first joined the lab. They did not only train me on the experimental skills but also mentored me on how to think and work as a scientist. I truly benefited a lot from our discussion about science, and I appreciated their supports when I started a brand-new journey in a different country. I would also like to thank Dr. Yao Cai, Dr. Navnita Kumar, Dr. Fang-Chu Lin, and Professor Kun Nie for all the great time in the lab discussing science, career, and life. I also appreciate their supports and helps when I face difficulties in my projects.

I would like to thank my committee members, Professor Holden Wu, Professor Ellen Sletten, and Professor Xiangfeng Duan for their advice and supports during my Ph.D. study. I am lucky to have the chance to collaborate with two of them on my research projects.

I would like to thank Professor Wu and his lab members for their help and supports on the MRI-guided HIFU projects. It has been a great experience working with all of you, and I am glad that we all learn from each other. I would like to thank Dr. Le Zhang for being a great mentor and friend. I appreciate his patience in explaining all the MRI concepts and protocols, and it was a great time hearing about the research stories from his Ph.D. life. I would also like to thank Xinzhou Li and Qing Dai for their brilliant work. The discussion with them made the time in the lab much more enjoyable.

I would like to thank Professor Sletten and her lab members for their help and supports on the thermo-responsive polymers and characterizations. I have learned a lot about their great works and appreciated their ideas and thoughts on our collaborated project. I would like to thank Dr. Dan Estabrook and John Chapman for the brilliant work and for being patient to explain polymer chemistry to me.

I am always curious to explore outside of the chemistry world, and I would like to thank all of the people who understand me and support me. I would like to thank Professor Elizabeth Randell Upton and Professor Robert Winter for giving me the opportunity to take their music history classes, where I could continue my music education and experience a different campus life full of art. I would also like to thank Professor Jennifer McCaney for the great lectures about life science entrepreneurship, where I catch up a lot from the business side of scientific research. Many thanks to Dr. Mary Sullivan for being a great mentor. I really appreciate her generous supports and helps in my career development, and I admire her for being dedicated and determined to her career.

In addition, I would like to thank all my friends. I am very lucky to have so many great friends in graduate school. You give me so much support through the difficulties and bring my life so much joy outside the lab. I will always remember the time when we had dinner parties and game nights, went to dancing classes, enjoyed the concerts and museums, and traveled around the continent. I also want to thank my old friends all over the world. I am glad that the time zones and distance do not dilute our friendship, and I am so lucky to get inspired and supported by all of you.

Last but not the least, I would like to thank my family and my partner. I always believe I have the best parents and family, and I am so proud of you as always. In the past 5 years, we cannot meet very often as we live in different countries, but I am grateful that we still understand and closely support each other. I also want to thank my partner for giving me the courage to chase the light and happiness far away. I am so blessed to be accompanied by such a creative, inspiring, and kind person.

Chapter 2 of the dissertation is adapted and reprinted with permission from a Perspective paper (*J. Am. Chem. Soc.*2021, 143, 16, 6025–6036). Copyright 2021 American Chemical Society. Co-author contributions: Lin, F. C., Xie, Y., Deng, T. and Zink, J. I. reviewed the literature and drafted the manuscript, and Deng, T. drafted the paragraphs related to high-intensity focused ultrasound. Jeffrey I. Zink was the P.I.

Chapter 3 of the dissertation is adapted and reprinted with permission from *Chem. Commun.* **2019**, *55*, 10261–10264. Copyright 2019 The Royal Society of Chemistry. Co-auther contributions: Deng, T. and Zhang, L. designed and conducted experiments and drafted the manuscript, Wu, H. H. and Zink, J. I. reviewed the manuscript. Wu, H. H. and Zink, J. I. were the co-P.I.s.

Chapter 4 of the dissertation is adapted from a manuscript in press from *ACS Nano*. Co-auther contributions: Deng, T., Zhang, L., and Li X. designed and conducted experiments and drafted the manuscript, Wu, H. H. and Zink, J. I. reviewed the manuscript. Wu, H. H. and Zink, J. I. were the co-P.I.s.

VITA

2012 - 2016	B.S. Chemistry Shandong University Jinan, China
2015	Cross-Disciplinary Scholars in Science and Technology (CSST) Scholarship University of California, Los Angeles
2016 - 2018	Teaching Assistant Department of Chemistry and Biochemistry University of California, Los Angeles
2018 - 2021	Research Assistant Department of Chemistry and Biochemistry University of California, Los Angeles
2020	UCLA Chemistry and Biochemistry Excellence in Research Fellowship Department of Chemistry and Biochemistry University of California, Los Angeles
2021	Inorganic Chemistry Dissertation Award, sponsored by the SG Fellowship in Chemistry Department of Chemistry and Biochemistry University of California, Los Angeles

SELECTED PUBLICATIONS

1. **Deng, T.**; Zhang, L.; Li, X.; Wu, H. H.; Zink, J. I. Responsive Nanoparticles to Enable a Focused Ultrasound-Stimulated Magnetic Resonance Imaging Spotlight. *ACS Nano* in press.
2. Lin, F.-C.; Xie, Y.; **Deng, T.**; Zink, J. I. Magnetism, Ultrasound, and Light-Stimulated Mesoporous Silica Nanocarriers for Theranostics and Beyond. *J. Am. Chem. Soc.* **2021**, *143*, 6025–6036.
3. Yu, Q.; **Deng, T.**; Lin, F. C.; Zhang, B.; Zink, J. I. Supramolecular Assemblies of Heterogeneous Mesoporous Silica Nanoparticles to Co-Deliver Antimicrobial Peptides and Antibiotics for Synergistic Eradication of Pathogenic Biofilms. *ACS Nano* **2020**, 14, 5926–5937.
4. Cai, Y.; **Deng, T.**; Pan, Y.; Zink, J. I. Use of Ferritin Capped Mesoporous Silica Nanoparticles for Redox and PH Triggered Drug Release *in Vitro* and *in Vivo*. *Adv. Funct. Mater.* **2020**, 30, 2002043.
5. **Deng, T.**; Zhang, L.; Wu, H. H.; Zink, J. I. A Nanoparticle Enabled Focused Ultrasound-Stimulated Magnetic Resonance Imaging Spotlight. *Chem. Commun.* **2019**, 55, 10261–10264.
6. Cheng, C. A.; **Deng, T.**; Lin, F. C.; Cai, Y.; Zink, J. I. Supramolecular Nanomachines as Stimuli-Responsive Gatekeepers on Mesoporous Silica Nanoparticles for Antibiotic and Cancer Drug Delivery. *Theranostics* **2019**, 9, 3341–3364.
7. Kumar, N.; Chen, W.; Cheng, C.; **Deng, T.**; Ruining, W.; Zink, J. I. Stimuli-Responsive Nanomachines and Caps for Drug Delivery. *Enzym.* **2018**, 43, 31–65.

Chapter 1. Introduction

Mesoporous silica nanoparticles (MSNs) are nanocarriers and are known for their tunable morphology and pore size, large surface area and pore volume, and great flexibility of surface chemical modification.[1] The MSNs used in this dissertation are synthesized by a sol-gel method from tetraethyl orthosilicate (TEOS) as the silica sources in the basic solution. For the MCM-41 type of MSNs, cetyltrimethylammonium bromide (CTAB) is used as a template to generate nanoparticles with hexanol pore structure with a pore size of about 2 nm. The 120 nm MSNs usually have a surface area of 1000 m^2/g, and a pore volume of 1 cc/g, which makes them good carriers for molecules either inside the pores or on the surface. The facile surface modification opens up the endless possibilities for various applications, including controlled drug delivery.[2,3] MSNs also have good biocompatibility and low toxicity, which brings great potential in biomedical applications.[4–6]

With the high demand for large molecule delivery, such as protein, RNA, and large drug molecules, there are studies to enlarge the pore of MSNs.[7] The synthesis method of large pore MSNs (LPMSNs) adopted in this dissertation is to use trimethylbenzene (TMB) to enlarge the CTAB micelles, thus enlarging the pores. Both the nanoparticle diameter and the pore size are tunable, and the pore size can vary from 5 – 15 nm. Similar to MSNs, the surface silanol groups make it possible for a large variety of chemical functionalization. Thus, it is a promising delivery vehicle for large biological molecules.

Magnetic resonance image (MRI) is a non-invasive diagnostic technology that does not involve ionizing radiation. Its three-dimensional imaging capacity with high resolution makes it a reliable guide for high-intensity focused ultrasound (HIFU). HIFU is a non-invasive therapeutic technology, and MRI-guided HIFU (MRIgHIFU) has been applied in the clinic for decades.[8,9]

With a deep penetration into tissue, HIFU has both thermal and mechanical effects at the HIFU focal point. Based on these effects, there have been studies on HIFU responsive drug delivery systems and MRI contrast agents.[10,11]

In Chapter 2, a comprehensive review of ultrasound responsive MSNs carriers is provided. On-command release of cargo molecules such as drugs from the pores can be activated by a variety of stimuli. This chapter focuses on one of the non-invasive, biologically usable external stimuli: ultrasound. We survey the variety of MSNs that have been and are being used and assess capping designs and the advantages and drawbacks of the nanoplatforms' responses to the various stimuli. We discuss important recent advances, their basic mechanisms, and their requirements for stimulation. Based on our survey we identify fundamental challenges and suggest future directions for research that will unleash the full potential of these fascinating nanosystems for clinical applications.

In Chapter 3, the proof-of-concept spotlight technique based on MRIgHIFU and MSNs is introduced that enhances MRI contrast. As shown in **Figure 1.1**, periodic HIFU modulation of a nanoparticle generates reversible MRI T_1 relaxivity changes at the 1.5 mm^3 focal point causing periodic T_1-weighted signal changes. Fourier analysis extracts signal changes at the modulation frequency, and a modulation enhancement map spotlights the precise region of interest by increasing contrast almost 100-fold.

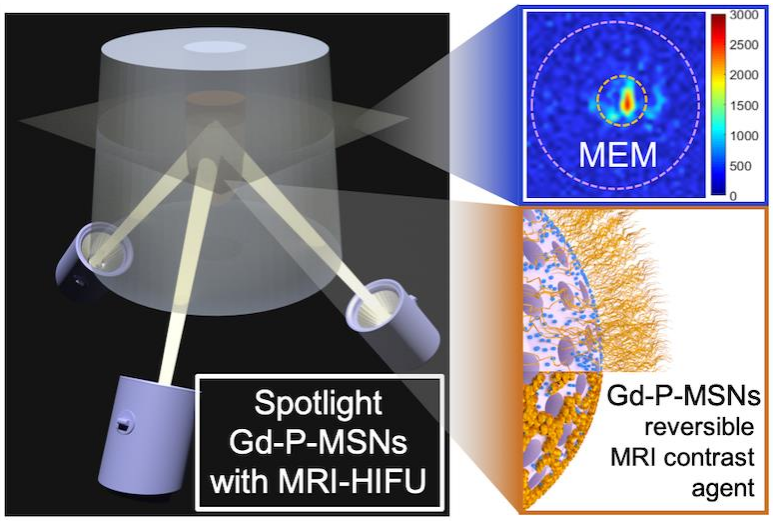

Figure 1.1 Proof-of-concept spotlight technique design based on MRIgHIFU and MSNs.

In Chapter 4, another functionalized MSNs are reported, and demostrate higher contrast enhancement results applied with the spotlight technique. Enhanced MRI contrast for the depiction of target tissues will improve the precision and applicability of HIFU therapy. As shown in **Figure 1.2**, the spotlight technique combines four essential components: periodic HIFU stimulation, strong modulation of T_1 caused by HIFU, rapid MRI signal collection, and spotlight MRI spectral signal processing. The T_1 modulation is enabled by a HIFU-responsive nanomaterial based on mesoporous silica nanoparticles with Pluronic polymers (Poloxamers) and MRI contrast agents attached. With periodic HIFU stimulation in a precisely defined region containing the nanomaterial, strong periodic MRI T_1-weighted signal changes are generated. Rapid MRI signal collection of the periodic signal changes is realized by a rapid dynamic 3D MRI technique, and spotlight MRI spectral signal processing creates modulation enhancement maps (MEM) that suppress background signal and spotlight the spatial location with nanomaterials experiencing HIFU stimulation. In particular, a framework is presented to analyze the trade-offs between different parameter choices for the signal processing method. The optimal parameter choices under a specific experimental setting achieved MRI contrast enhancement of more than two orders of

magnitude at the HIFU focal point, compared to controls. The framework and demonstrated enhancement provide a foundation for translation of spotlight MRI to future biomedical applications of precision therapy.

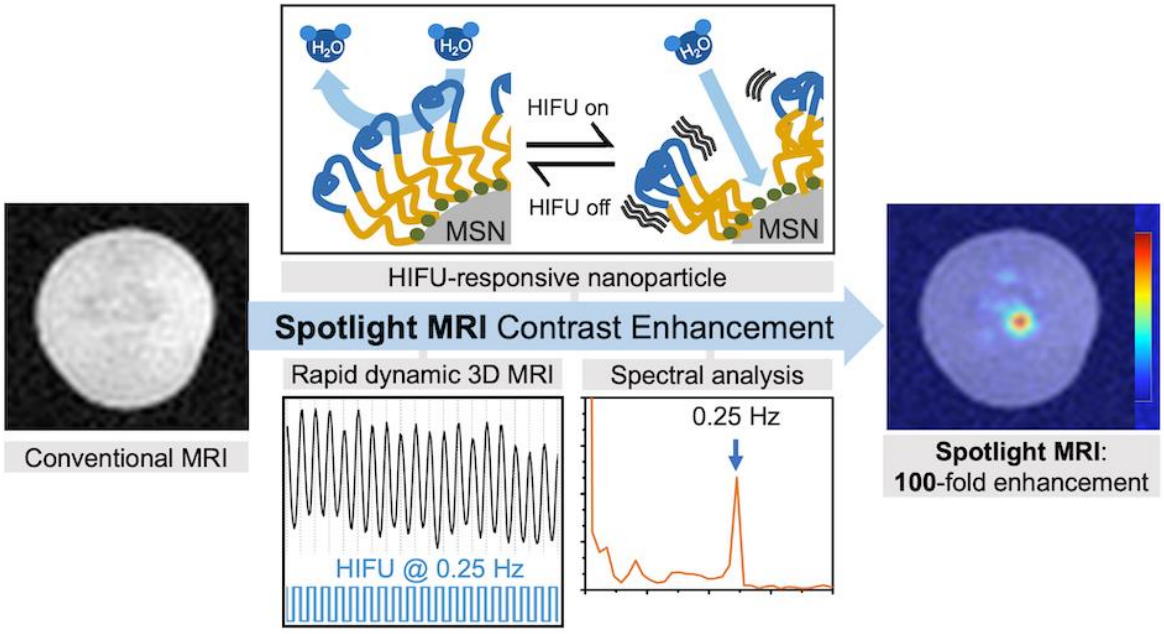

Figure 1.2 MSNs functionalized with Pluronic polymers applied with the spotlight technique.

In Chapter 5, it is demonstrated that the spotlight technique can be applied at human body temperature. With the tailored poly(2-oxazoline)s with lower critical solution temperature (LCST) at 40 °C, MSNs were functionalized to generate reversible MRI contrast change. Applied with the spotlight MRI technique, significant MRI contrast enhancement was realized at human body temperature. The temperature oscillation range is small (3 °C), and the data acquisition is relatively fast (in 100 s), which takes it a step further to the biomedical application in the clinic.

In Chapter 6, I shift my focus to the other side of MRIgHIFU: the HIFU-responsive drug release. In this work, LPMSNs are used as the nanocarrier and develop an effective drug loading procedure to load a large drug molecule, Docetaxel. The HIFU-responsive release was demonstrated in a biologically relevant solvent and the factors affecting the drug loading and

release performance were studied, such as solvent, HIFU amplitude and duration, and nanoparticle functionalization.

In Chapter 7, I continue my focus on HIFU-responsive cargo delivery, but instead of using a drug, the delivery of an MRI contrast agent, Magnevist, is studied. A capping system based on thermo-responsive polymer was designed, the cargo loading and release conditions were optimized, the mechanism of the cargo delivery process was explored, and cargo release monitored by MRI was demonstrated.

1.1 References

(1) Ruehle, B.; Clemens, D. L.; Lee, B.-Y.; Horwitz, M. A.; Zink, J. I. A Pathogen-Specific Cargo Delivery Platform Based on Mesoporous Silica Nanoparticles. *J. Am. Chem. Soc.* **2017**, *139*, 6663–6668.

(2) Chen, W.; Glackin, C. A.; Horwitz, M. A.; Zink, J. I. Nanomachines and Other Caps on Mesoporous Silica Nanoparticles for Drug Delivery. *Acc. Chem. Res.* **2019**, *52*, 1531–1542.

(3) Aznar, E.; Oroval, M.; Pascual, L.; Murguía, J. R.; Martínez-Máñez, R.; Sancenón, F. Gated Materials for On-Command Release of Guest Molecules. *Chem. Rev.* **2016**, *116*, 561–718.

(4) Li, Z.; Barnes, J. C.; Bosoy, A.; Stoddart, J. F.; Zink, J. I. Mesoporous Silica Nanoparticles in Biomedical Applications. *Chem. Soc. Rev.* **2012**, *41*, 2590.

(5) Hoang Thi, T. T.; Cao, V. Du; Nguyen, T. N. Q.; Hoang, D. T.; Ngo, V. C.; Nguyen, D. H. Functionalized Mesoporous Silica Nanoparticles and Biomedical Applications. *Mater. Sci. Eng. C* **2019**, *99*, 631–656.

(6) Jafari, S.; Derakhshankhah, H.; Alaei, L.; Fattahi, A.; Varnamkhasti, B. S.; Saboury, A. A. Mesoporous Silica Nanoparticles for Therapeutic/Diagnostic Applications. *Biomed. Pharmacother.* **2019**, *109*, 1100–1111.

(7) Xu, C.; Lei, C.; Yu, C. Mesoporous Silica Nanoparticles for Protein Protection and Delivery. *Front. Chem.* **2019**, *7*, 1–12.

(8) Lin, F.-C.; Xie, Y.; Deng, T.; Zink, J. I. Magnetism, Ultrasound, and Light-Stimulated Mesoporous Silica Nanocarriers for Theranostics and Beyond. *J. Am. Chem. Soc.* **2021**, *143*, 6025–6036.

(9) Keserci, B.; Duc, N. M.; Nadarajan, C.; Huy, H. Q.; Saizan, A.; Wan Ahmed, W. A.; Osman, K.; Abdullah, M. S. Volumetric MRI-Guided, High-Intensity Focused Ultrasound Ablation of Uterine Leiomyomas: ASEAN Preliminary Experience. *Diagnostic Interv. Radiol.* **2020**, *26*, 207–215.

(10) Cheng, C. A.; Chen, W.; Zhang, L.; Wu, H. H.; Zink, J. I. A Responsive Mesoporous Silica Nanoparticle Platform for Magnetic Resonance Imaging-Guided High-Intensity Focused Ultrasound-Stimulated Cargo Delivery with Controllable Location, Time, and Dose. *J. Am. Chem. Soc.* **2019**, *141*, 17670–17684.

(11) Cheng, C.-A.; Chen, W.; Zhang, L.; Wu, H. H.; Zink, J. I. Magnetic Resonance Imaging of High-Intensity Focused Ultrasound-Stimulated Drug Release from a Self-Reporting Core@ Shell Nanoparticle Platform. *Chem. Commun.* **2020**, *56*, 10297–10300.

Chapter 2. Ultrasound-Stimulated Mesoporous Silica Nanocarriers for Theranostics and Beyond

 Co-author contributions: Lin, F. C., Xie, Y., Deng, T. and Zink, J. I. reviewed the literature and drafted the manuscript. Jeffrey I. Zink was the P.I. This chapter emphasizes on HIFU related paragraphs to fit in the scope of the thesis.

2.1 Introduction

Chemical and materials research involving mesoporous silica has developed rapidly in the past decade, driven initially by interest in this new type of structurally ordered nanomaterial and accelerated by the potential applications in catalysis and especially biomedical drug delivery. Most of the materials can be synthesized on the benchtop at moderate temperatures, and the resulting silica structures can be readily derivatized with a huge variety of organic, inorganic and biomolecules that have functions varying from supramolecular nanomachines to cancer cell targeting ligands. In this chapter we focus primarily on mesoporous silica nanoparticles (MSNs), which are made by the sol-gel synthesis of silica and the self-assembling surfactant templating of the pores. The original materials were multi-sized aggregates, but further research ultimately led to controllable synthesis of spherical particles with primary sizes of less than 100 nm with mesopores between 2 – 10 nm in diameter **(Figure 2.1a)**.[1,2] The attractive features of MSNs, such as porous frameworks and surface functionality, allow various types of fabrication methods and have led to advanced applications of MSNs in multiple fields.[3–7] Various advanced architectures of MSNs such as large-pore MSNs (LPMSNs, **Figure 2.1b**), hollow MSNs (HMSNs, **Figure 2.1c**),

or core-shell MSNs **(Figure 2.1d**) have also gained significant interest for multifunctional biomedical purposes.[1,8]

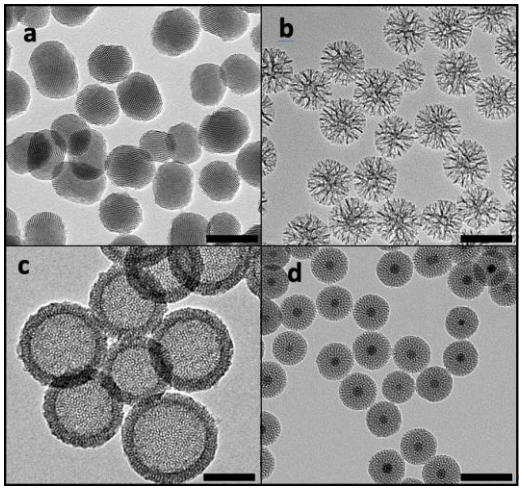

Figure 2.1 TEM images of the most common spherical mesoporous silica nanoparticles (MSNs) used for biomedical drug delivery. (a) Tubular pores ~2.5 nm in diameter in a two-dimensional hexagonal array. The pores are commonly templated with cetyltriammoniumammonium bromide (CTAB) surfactant. (b) "Large pore" MSNs with dendritic center-radial oriented pores ~ 4 nm in diameter. The pore size can be changed using "swelling" agents, larger molecular weight templating surfactants, or a hydrophilic and hydrophobic solvent mixture. (c) Hollow MSNs. The hollow center is frequently formed by condensing mesoporous silica around a spherical nanoparticle that is then dissolved and leaves behind a spherical void. (d) Core-shell MSNs with radial pores. This important example contains a superparamagnetic iron oxide (SPION) core. Scale bar: 100 nm.

Over a decade ago during the initial excitement about all things nano, (popularized by the title of Feynman's lecture "There's Plenty of Room at the Bottom"),[9] there was great fascination and interest in supramolecular structures, especially in the synthesis and properties of molecules in molecules such as rotaxanes that could function as nanomachines.[10,11] Around the same time,

self-assembled and templated porous nanostructures described above also became popular. It was a logical extension to try to put molecules in the pores and cap the pores with nanomachines. Early studies involved materials synthesis, emptying the self-assembled surfactants from the pores, and filling them with molecules from a solution. Examples include proteins,[12] hydrophobic drugs,[13] and fluorescent dyes.[14,15] Alternatively, the desired molecules could be dissolved in the initial sol used in the synthesis and become incorporated during the templating and gelation process.[16] Many early studies used macroscopic aggregates or thin films for luminescent molecules, polymers, or living cells encapsulation.[17–19]

The next challenge required not only filling the pores in the nanoparticles with molecules such as drugs but also trapping them in the pores with controllable nanomachine caps.[20–23] The pores essentially became tiny capped bottles in the particles; the challenge was to controllably cap the particles and uncap them at will. Today there are literally hundreds of types of caps designed to be specifically opened by a chosen stimulus.[22–24] For biomedical drug delivery applications, the stimuli must be biocompatible and feasible to control.[25] How can a particle deep in a tumor in the interior of an organism be controlled? Two classes of control have been developed: autonomous chemical stimulus that exists at the desired biological site (such as pH change in a tumor or cancer cell), and external stimuli that can non-invasively penetrate the body and tumor and open the cap.

The emphasis of this chapter is on external control of nanoparticles potentially useful for medical therapy. We first discuss recent developments in trapping and releasing molecules from the pores using biocompatible external stimuli and some of the advanced capping systems of MSN carriers designed for the three types of stimuli — magnetism, ultrasound, and light (**Figure 2.2**). Light stimulation has the best spatial resolution but the poorest tissue penetration; magnetism has great tissue penetration but the poorest resolution. The major application of interest is drug delivery,

but we will also discuss briefly diagnosis and targeting. The clinical relevance of these stimuli will also be highlighted. We then provide our insights on the future directions the field could take to advance biomedical applications and accelerate clinical translation of MSNs-based drug delivery platforms.

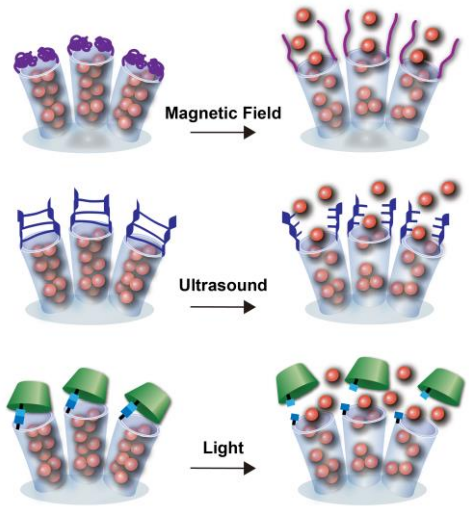

Figure 2.2 Schematic representations of capping systems over pores and their responses to external magnetic field, ultrasound, or light stimuli that cause cargo molecules trapped in the capped pores to be released. Top: the phase change of polymer caps on a SPION@MSN that is stimulated by heat from a superparamagnetic core in an alternating magnetic field (AMF). Middle: bond cleavage of linker-based caps that are triggered by ultrasound. Bottom: the dissembling of supramolecular caps that are activated by light. In all cases the trapped cargo molecules (orange spheres) diffuse out of the pores after the stimulation opens the cap. Note that the pores are not drawn to scale and that each illustration only shows a few of many pores in a nanoparticle.

2.2 Ultrasound Control of Nanocaps

The tunable dual thermal and/or mechanical effects of ultrasound can be used to stimulate a wide variety of nanocap designs and produce highly versatile and advantageous methods for controlling MSN-based drug delivery systems. The heat produced by ultrasound can be applied to

the thermo-sensitive capping systems discussed in the previous section, and the additional mechanical effects can be applied to uncap pores via other ultrasound responsive mechanisms such as bond breaking. Ultrasound can be carefully modulated by tuning frequency, power density, duty cycles, and exposure time.[42] The depth of penetration and potential cavitation can be tuned by changing the frequency. The intensity of the ultrasound plays a major role in not only the cavitation effects but also the thermal effects.[42] By focusing ultrasound waves into a small volume – the focal point – which is usually several cubic millimeters,[43] high intensity focused ultrasound (HIFU) with an intensity of $\geq$3 W/cm^2 and deep tissue penetration capability offers a noninvasive method for nanoparticle-enabled delivery of drugs. HIFU can locally trigger cargo release at a specific location with little or even no side effects because its intensity is strong only at the focal point. Current therapeutic applications utilize both the thermal effects of HIFU, which benefit from the rapid temperature rise at HIFU focal point to induce coagulative necrosis, and mechanical (cavitation) effects that break chemical bonds.[44] Combined with imaging methods such as low frequency ultrasound or magnetic resonance imaging (MRI), HIFU is able to ablate the tumor tissue precisely with minimal invasion and has been used to treat solid tumors such as prostate, rectal, pancreatic, breast, bladder, brain, and bone.[44,45] In addition, HIFU can temporarily disrupt the blood–brain barrier (BBB) and help the therapeutic agents into the brain.[46] In the following sections, we will discuss how ultrasound responsive capping systems control the pore entrance accessibility and advance the cargo delivery systems and the development of nanotheranostics.

Ultrasound-Stimulated Supramolecular-Based Nanocaps

Cavitation is one of the major mechanical effects produced by ultrasound. It depends on a broad variety of parameters such as ultrasound frequency and the presence of bubbles or cavitation nuclei.[42] It was demonstrated that MSNs can be drug carriers and inertial cavitation nuclei at the

same time; the mechanical strain induced by the acoustic cavitation can help enhance and control the drug release.[47,48] For example, β-CD-capped MSNs with hydrophobic internal channels were designed for the delivery of the hydrophobic cancer drug paclitaxel (PTX), where the loaded hydrophobic PTX and the gas stored in the hydrophobic mesopores acted as an ultrasonic cavitation nuclei.[48] In addition to the excellent synergistic effect *in vitro* and the high biocompatibility *in vivo*, it was demonstrated that this delivery platform could significantly inhibit the 4T1 mammary tumor growth by more than 3-fold when compared with the MSNs without hydrophobic modification.

Thermal effects generated in biological tissues by ultrasound were also utilized by dibenzo-crown ether periphery nanovalves on SPION@MSNs for ultrasound-responsive drug delivery and tumor cell imaging. The mesopores were blocked by the interaction between cations (Na^+ or Cs^+) and the oxygen-rich, electronic donating crown ether's ethylene glycol chains.[49] The blocking agents dissociated from dibenzo-crown ethers by the energy gained from ultrasound, leading to 3-fold enhanced DOX release. The *in vitro* biological evaluation revealed that the nanoparticles are biocompatible and are taken up by L929 normal fibroblast cells. The embedded SPIONs caused the spin-spin T_2 relaxation time changes; the attained dark contrast on the MRI images further demonstrates their potential use as theranostic agents.

HIFU can be guided by an imaging technique such as MRI or low-frequency ultrasound imaging.[45,51] Due to this attractive feature, many multifunctional nanoparticles have been developed to realize both diagnostic and therapeutic outcomes. For example, a theranostic approach that can control and monitor drug release using magnetic resonance-guided high intensity focused ultrasound (MRgHIFU) was developed (**Figure 2.3**).[50] In this method, a SPION@MSN structure was used: the mesoporous silica shell provides large pore volume for cargo storage and

delivery and the water access to the paramagnetic SPION core changes after drug release, leading to T_2 MRI contrast change. The HIFU-responsive cap containing an aliphatic azo-containing compound was attached to the nanoparticle surface and control drug release. Using this design, the image contrast changes can be used to measure cargo release and the therapeutic efficacy. The process was visualized in human pancreatic cancer cells. It brings possible applications of assessing the precision of HIFU-triggered drug release, and drug dose painting.

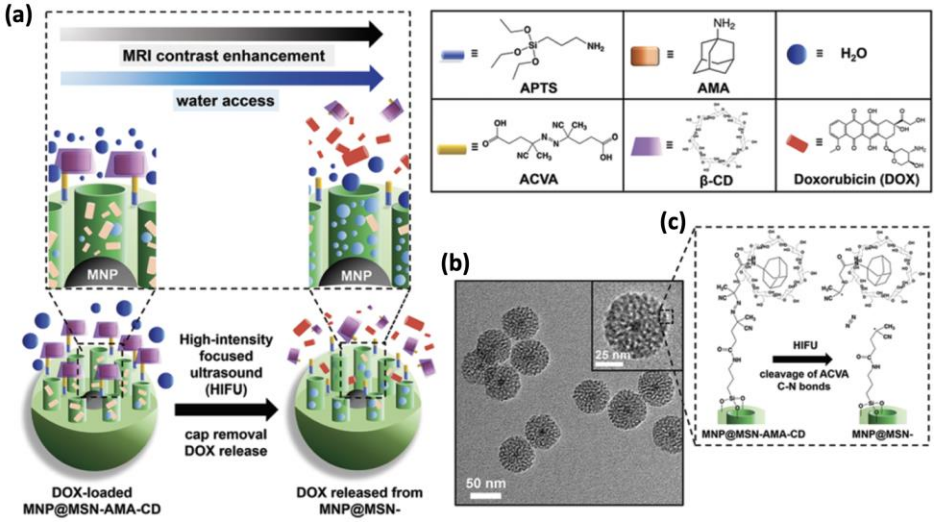

Figure 2.3 Capping system stimulated by high-intensity focused ultrasound (HIFU) to control drug release from MSNs. The release is imaged by magnetic resonance imaging (MRgHIFU). (a) On the left, doxorubicin (DOX) is trapped in the mesopores by β-CD caps that are held in place by thermo-sensitive azo bonds. On the right, after the HIFU stimulation is turned on, the thermo-sensitive bonds are cleaved by HIFU, the cap is opened and DOX is released. The increased water access to the superparamagnetic iron oxide core causes the T_2 MRI contrast to change. (b) TEM images of core-shell MSNs, and (c) the bond cleavage reaction stimulated by HIFU. Image adopted from ref [50] with permission from The Royal Society of Chemistry.

Ultrasound-Stimulated Polymer-Based Nanocaps

The cavitation caused by ultrasound can also be applied on MSNs coated with polymer-based capping systems. The synergy between MSNs and polymer was shown to enhance the ultrasonic susceptibility and reliability of ibuprofen drug release,[52] where the convection increase due to the effects of cavitation increased the diffusion rate of the drug and facilitated faster drug release. Additionally, high intensity ultrasound can cause irreversible biological changes such as cancer cell eradication and is capable of inducing chemical change for cargo release.[53] For example, the ultrasound stimulation can result in a change of polymer conformation and the subsequent release of DOX in LNCaP tumor cells (**Figure 2.4**). By further coating the polymer-grafted MSNs with a PEI layer, it can enhance nanoparticle internalization into Decidua Mesenchymal Stem Cells (DMSNs), where DMSNs acted as transporters to the tumor tissue.[54] Such engineered nanoparticles were shown to release Calcein-AM *in vivo* after 10 min of ultrasound application and the DOX-loaded PEI-coated nanoparticles could be retained in DMSNs for 6 days and exhibited high migratory capacity toward the tumor homogenate, leading to the effective uptake of DMSNs. The release of DOX, which only occurred when the platform is exposed to ultrasound, resulted in the reduction of N-Nitroso-N-methylurea cell viability. Future approaches of polymeric delivery systems should focus on the enhancing the efficiency of particle internalization into cells for better treatment efficacy and clinical applications.

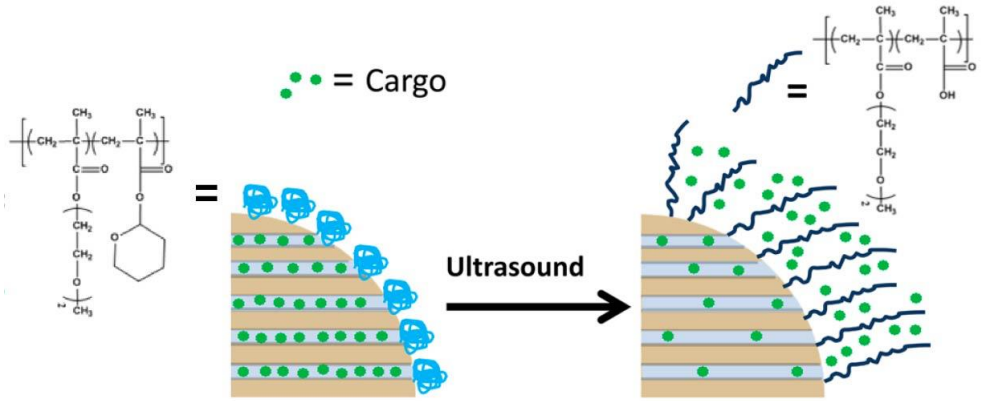

Figure 2.4 An ultrasound-responsive copolymer grafted on the surface of MSNs changes conformation in response to ultrasound irradiation. The cargo is retained in the pores when the polymer is coiled. Ultrasound irradiation induces the change in polymer conformation to extended coil-like, unblocking the pore openings and allowing the trapped cargo to be released. The image adopted from ref. [53] Copyright 2015 American Chemical Society.

HIFU is being used in the clinic. There are several designs of capping systems that are responsive to HIFU that demonstrate promising potential for applications. A reversible ultrasound-responsive hybrid nanocarrier based on alginate-coated MSN was designed to utilize mechano-responsive chemical bond breaking and reforming of the capping systems for realizing HIFU-controlled cargo release.[55] It was demonstrated that 100% of the cargo can be released after HIFU irradiation with low *in vitro* cytotoxicity. In another study, polydopamine (PDA) coated MSNs were shown to release DOX due to ultrasonic cavitation, where the pulsatile drug release could be controlled by switching the HIFU on and off.[56] PEG was also designed to cap the pore in a biofriendly MSN drug delivery platform for MRgHIFU.[57] The PEG-coated nanocarriers enabled the HIFU-triggered release of FDA approved gadolinium-based contrast agent, $Gd(DTPA)^{2-}$ without hyperthermia because cavitation induced by HIFU could lead to PEG cleavage and degradation. With MRgHIFU, real time spatial- and temporal-control of cargo release in three-dimensional space can be realized. The study further demonstrated that the dose of cargo release

was correlated to HIFU stimulation times and power levels. The significance of this platform for future biomedical applications was supported by ex vivo results demonstrating that MRgHIFU achieved selective stimulation spatially in the presence of nanoparticles. This platform is promising for precise therapy that delivers drugs to a specific tissue in real time.

2.3 Outlook and Perspectives

Though considerable progress and advances have been made over the past decade towards externally controlled MSN-based drug delivery (and other innovative applications) by exploring different capping systems, challenges for their use in biomedical applications need to be addressed to achieve clinical translation. To summarize and look toward the future, we point out various research opportunities and practical consideration involved in preclinical development and clinical translation of external responsive MSN-based nanocarriers.

Research Opportunities Taking Advantage of Modern Clinically Available Medical Devices.

External triggers discussed in this chapter are attractive because the triggering events can be controlled remotely outside of human bodies. The high promise for external stimuli for various therapies has been evidenced by their progress in clinical trials and usages. HIFU was FDA approved and was first applied in the clinic in 2004 to treat uterine fibroids under the guidance of MRI.[72] SPION-AMF-based therapy in phase-I and phase-II clinical trials of glioblastoma and prostate cancer treatments showed promising results.[28] The patients are treated by the NanoActivator® (MagForce, Germany) device that generates the AMF. Our perspective is that AMF and HIFU are the two stimuli of the future that provide wide-open opportunities for taking advantage of newly available clinical instrumentation. Along with them, new stimuli-responsive drug delivery nanoparticles will be needed to exploit instruments that will become available in the future. For example, external electromagnetic stimuli such as radiofrequency (RF) waves (100 kHz

to 300 GHz)[73–75] or microwaves (100 MHz to 3 GHz)[76] have been suggested as stimuli of drug release. The low-power RF field can transmit throughout the brain, resulting in improved drug penetration across the BBB for an efficient drug delivery to glioma cells. The magnetic cores of Fe_3O_4@MSNs doped with ZnO have microwave-absorbing and thermal conversion properties and can generate local heat under microwave radiation, suggesting a new path toward thermo-stimulated drug delivery platforms.[76] Despite the promising results, further research is needed to confirm their exploitability in clinics.

Throughout this chapter, examples of exceptional performances *in vitro* and *in vivo* of each type of stimulus have been demonstrated. It is important to note that all stimuli discussed in this chapter produce heat. Although the heat can be controlled and can help trigger cargo release on-demand, it can be dangerous to human tissues if too much is produced. Stimuli with low power is generally safer but requires caps that respond sensitively. While stimuli with periodic or short pulses may provide a better control of the release profile, the attained treatment efficiency should be carefully compared with other conditions. Appropriate parameters for each stimulus must be carefully analyzed for its usage *in vivo*. Analysis on these external stimulations should be conducted to make sure that stimuli only aim at the desired groups (e.g., nanocaps) but not the other components (e.g., protective coating or targeting ligands) of nanocarriers because these components play a crucial role in enhancing their performance in living organisms, as will be discussed next.

Research Directions Based on Surface Engineering for Enhancing Targeting Efficacy

A key feature of a nanoplatform to combat a disease is its capability of specifically targeting the diseased cells without affecting the normal healthy tissues. To achieve the optimal treatment efficacy, the nanoparticles carrying the cargo need to be capable of reaching the location of interest

and interact exclusively with the targeted cells. Active targeting via the specific interaction between ligands decorating the surface of the nanocarriers and the receptors overexpressed on the target cells has been used to enhance nanoparticle uptake.[77,78] MSN-based nanoplatforms offer an array of potential solutions for the development of receptor-based active targeting. For example, short-stranded DNA or RNA oligonucleotides with a specific sequence, the aptamer, could be developed to serve as not only the stimuli-responsive capping system but also the targeting ligands on the nanoparticle surface. As another example, a supramolecular cap discussed above can be functionalized with targeting agents such as folic acid to add targeting functionality and thus achieve the enhanced selective targeting of cancer cells.[48] Polymer coated MSNs can be further covered with an oppositely charged polymer with targeting functionality via electrostatic forces; for example, the interactions between the anionic PEI and cationic hyaluronic acid (HA).[79] Methods of introducing different functional groups to the surface of nanocarriers, such as polymers with various surface functionalities, are worth investigation in further prospective studies to append both targeting and capping agents to the particle surface for enhancing cell and tumor uptake as well as stimuli-responsive release of a drug.

Studies also showed that the interactions between cells and nanoparticles are highly sensitive to the nanoparticle surface chemistry. For example, by fusing zwitterionic lipid-based vesicles on MSNs – the so-called "protocells", individual cell targeting and delivery can be achieved.[80] Moreover, nanoparticles with zwitterionic surfaces have been shown to offer low nonspecific binding with the bioenvironment and high cell uptake,[81] suggesting that the nanoparticle surface charges (i.e. those of the charged functional groups of the capping systems) should be appropriately designed and optimized for *in vivo* targeting applications. The development of new approaches such as coating the MSN surfaces with biomolecule-based layers to mimic exosomes

or cell membranes will also be an interesting field to focus on for a more direct targeting and enhanced treatment efficacy.[82] By building a protein corona shield on the MSNs functionalized with targeting agents, it was demonstrated that the interactions between MSNs and biological systems can be regulated, avoiding the clearance of MSNs by macrophages and retaining their targeting ability *in vitro* and *in vivo*.[83] Apart from surface modification of the MSN surface, the aspect ratios of the particles were shown to have impact on cellular uptake mechanism and different aspects of cellular function.[84] Such evidence suggests that the unique characteristic features of MSNs (e.g., both surface and structure) will play an important role in enhancing therapeutic efficacy.

Research Opportunities Using Core-Shell, Large-Pore and Hollow MSNs

Monitoring the dose in real time is another very challenging and important topic to pursue for the advancement of precision medicine. Discussed earlier in this chapter, measuring and controlling the drug release from SPION@MSNs can be realized using MRgHIFU.[57] When using light as the stimulus, fluorescence quenching is a possible future direction to achieve real-time monitoring of drug release by capturing the change of emission intensity or wavelength before and after drug release. To further advance light-stimulated platforms and allow the observation of the light-based processes in deep tissue, shortwave infrared (SWIR) light appears promising. HMSNs that have mesopores that open into a large cavity has been used for optical imaging with SWIR via the assembly of SWIR-emissive J-aggregates in HMSNs.[85] This development resulted in a significant improvement in depth penetration, contrast, and sensitivity and is therefore worthwhile to be further explored for advancing therapeutic drug monitoring.

MSN-based platforms can also be designed for enhancing MRI contrast. While it is known that microbubbles can enhance ultrasound imaging and air-filled MSNs can serve as a HIFU-

responsive ultrasound contrast agent,[86,87] air, which provides paramagnetic susceptibility when compared with the surrounding diamagnetic water, is also a source of contrast in MRI.[88] We anticipate that the future design of gas-encapsulated MSNs can be used as MRI contrast agents that can be triggered by the external stimuli that we discussed in this chapter. In addition to improving MRI contrast via utilization of gas, a spotlight technique was developed to enhance MRI contrast specifically at the targeted tissue with ~1.5 mm^3 resolution.[89] This technique is based on periodic HIFU responsive MSNs modified with $Gd(DTPA)^2$ and PNIPAM. These MSNs can generate reversible MRI contrast changes. Spectral analysis extracts periodic signal changes, and a modulation enhancement map is reconstructed with a contrast enhancement of almost 100-fold at HIFU focal point compared to conventional MRI protocol. This spotlight technique can potentially be utilized to identify detailed tissue structure as well as enhance MRI contrast change with a wide variety of applications. Combined with the drug delivery features of MSNs, we envisioned that it would open more possibilities in the field of theranostics.

In addition to utilizing regular MSNs in the advancements of diagnosis, LPMSNs **(Figure 2.1b)** have great potential for the encapsulation of large biomolecules such as peptides and proteins that are increasingly important new therapeutic agents. The delivery of RNA or DNA to date mainly involved the outside surfaces of particles. Recently, LPMSNs are being investigated for gene therapy and to deliver relatively large biomolecules such as siRNA, IL-4 cytokines, and antigenic protein.[90] The pore tunability of MSNs was used to regulate antigen delivery efficacy and demonstrated the enhanced immune response intensity by using MSNs with large pores.[91] These strategies could lead to more advanced designs of MSN-based vaccines for cancer immunotherapy, which is a rapidly developing area. LPMSNs have been employed to encapsulate smaller functional nanoparticles to realize MR cancer diagnosis/imaging[92], bimodal MR/NIR

imaging,[93] and biosensing.[94] They have also been used to immobilize enzymes without capping by utilizing physical adsorption.[95] Similar to the chemical amplifier where a nanogate controls the access to an encapsulated enzyme,[96] a more advanced design of mechanized particles that involves a catalyst-based production of amplified response when triggered can potentially increase detection sensitivity and be used as a controllable sensor to identify targeted signals from circulating cancer cells.[97]

The growing usage of the LPMSNs requires design and testing of large stimuli-responsive caps. Burst release of the encapsulated cargo sometimes occurs after the drug administration, resulting in a significant decrease in the number of cargo drugs that can reach the pharmacological target in the body. While it can be envisioned that suitable pore gatekeepers can minimize leakage and premature release of cargo, not many supramolecular-based nanocaps that can block the large pore openings have been reported.[96] We think the design and synthesis of stimuli-responsive capping systems for LPMSNs will open up new opportunities in both theranostic and biosensor applications.

It is interesting to note that HMSNs are underutilized in spite of their potentially large storge capacity. HMSNs have been used to trap a large quantity of nitric oxide (NO) donors that released NO in response to ultrasound, resulting in an excellent *in vivo* effect in inhibiting the Panc-1 tumor.[98] Because the internal cavity of a HMSN is connected to the particle surface through the mesoporous channels, these kinds of particles merit further applications.[99]

2.4 General Considerations

An obvious and extremely important component of the design of capping systems is that the material must function in relevant biofluids (e.g., blood, cytosol) at or near the physiological pH of 7.2. Nanomachines that function beautifully in distilled water may not operate at all in the

presence of proteins (e.g., albumins) or other common biomolecules. Equally importantly, the particles must be dispersible (minimal aggregation) in the biofluids. Well known strategies for increasing dispersibility, for example by attaching PEG polymers to the particle's surfaces, may decrease the number of capping molecules that can be attached and also interfere with their operation. Despite the successful utilization of MSNs *in vitro* and *in vivo*, full understanding of their biocompatibility in biological systems is needed before their translation to the clinic.

A second and extremely important constraining consideration is the toxicity of the final nanoparticle. Spherical MSNs have been shown to be safe, but each new cap or attached molecule creates a new particle that must be tested for safety. This constraint means that when designing a new capping system, not only the cap and all other molecules attached must be nontoxic, but also all of the degradation products resulting from the response to stimulation must also be nontoxic. Other essential factors for the MSN-based carriers' uses in clinics include ensuring high purity and uniformity of nanoparticles, which sometimes may be challenging. It will be necessary to establish cost-effective and scalable methods to fabricate various kinds of well-dispersed high-quality MSNs with good reproducibility in order to receive approval from the FDA.

Ultimately, MSNs possessing capping systems that respond to one or more external stimuli hold great promise for biological applications such as diagnostics and therapeutics. Despite their promise, to advance and succeed in clinical trials, well-defined parameters for the stimuli should be established and more effort should be focused on addressing, identifying, and solving the potential toxicity of the designed nanosystems. The system should be kept as simple as possible through first utilizing its intrinsic properties to the fullest extent before incorporating any other component for improvement of treatment efficacy. The challenges that nanosystems face for use in various applications are multi-faceted. Successful clinical translation of nanoparticles depends

on cooperation between physicochemical and biomedical sciences and interdisciplinary research in academic, industrial, and clinical settings to address the real clinical challenges.[82] Finally, to accurately compare preclinical results, to improve existing nanoparticles, and to design promising new nanosystems, more effort on the standardization of the laboratory practices and preclinical characterization, including physicochemical, *in vitro*, and *in vivo* characterization, is necessary. Such a standard can help future researchers recognize the critical healthcare needs when designing the nanoparticles and speed up the advancement of MSN-based nanosystems using past experiences. If all the challenges can be appropriately solved and requirements can be met, triggered MSN-based drug delivery nanocarriers that avoided deleterious off-target effects can strengthen the treatment efficacy and offer a very promising research field with high impact for therapeutic applications.

2.5 References

(1) Kankala, R. K.; Han, Y. H.; Na, J.; Lee, C. H.; Sun, Z.; Wang, S. Bin; Kimura, T.; Ok, Y. S.; Yamauchi, Y.; Chen, A. Z.; Wu, K. C. W. Nanoarchitectured Structure and Surface Biofunctionality of Mesoporous Silica Nanoparticles. Adv. Mater. 2020, 32, 1–27.

(2) Yanagisawa, T.; Shimizu, T.; Kuroda, K.; Kato, C. The Preparation of Alkyltrimethylammonium-Kanemite Complexes and Their Conversion to Microporous Materials. Bulletin of the Chemical Society of Japan. 1990, pp 988–992.

(3) Vivero-Escoto, J. L.; Huxford-Phillips, R. C.; Lin, W. Silica-Based Nanoprobes for Biomedical Imaging and Theranostic Applications. Chem. Soc. Rev. 2012, 41, 2673.

(4) Lee, J. E.; Lee, N.; Kim, T.; Kim, J.; Hyeon, T. Multifunctional Mesoporous Silica Nanocomposite Nanoparticles for Theranostic Applications. Acc. Chem. Res. 2011, 44, 893–902.

(5) Ambrogio, M. W.; Thomas, C. R.; Zhao, Y. L.; Zink, J. I.; Stoddart, J. F. Mechanized Silica Nanoparticles: A New Frontier in Theranostic Nanomedicine. Acc. Chem. Res. 2011, 44, 903–913.

(6) Argyo, C.; Weiss, V.; Bräuchle, C.; Bein, T. Multifunctional Mesoporous Silica Nanoparticles as a Universal Platform for Drug Delivery. Chem. Mater. 2014, 26, 435–451.

(7) Biju, V. Chemical Modifications and Bioconjugate Reactions of Nanomaterials for Sensing, Imaging, Drug Delivery and Therapy. Chem. Soc. Rev. 2014, 43, 744–764.

(8) Liong, M.; Lu, J.; Kovochich, M.; Xia, T.; Ruehm, S. G.; Nel, A. E.; Zink, J. I.; Tamanoi, F.; Zink, J. I.; Nel, Ќ. A. E.; Tamanoi, F.; Zink, J. I. Multifunctional Inorganic Nanoparticles for Imaging, Targeting, and Drug Delivery. ACS Nano 2008, 2, 889–896.

(9) Feynman, R. P. There's Plenty of Room at the Bottom: An Invitation to Enter a New Field of Physics. American Physical Society Lecture, 1959, California Institute to Technology.

(10) Xue, M.; Yang, Y.; Chi, X.; Yan, X.; Huang, F. Development of Pseudorotaxanes and Rotaxanes: From Synthesis to Stimuli-Responsive Motions to Applications. Chem. Rev. 2015, 115, 7398–7501.

(11) Schalley, C. A.; Beizai, K.; Vögtle, F. On the Way to Rotaxane-Based Molecular Motors: Studies in Molecular Mobility and Topological Chirality. Acc. Chem. Res. 2001, 34, 465–476.

(12) Slowing, I. I.; Trewyn, B. G.; Lin, V. S. Y. Mesoporous Silica Nanoparticles for Intracellular Delivery of Membrane-Impermeable Proteins. J. Am. Chem. Soc. 2007, 129, 8845–8849.

(13) Lu, J.; Liong, M.; Zink, J. I.; Tamanoi, F. Mesoporous Silica Nanoparticles as a Delivery System for Hydrophobic Anticancer Drugs. Small 2007, 3, 1341–1346.

(14) Manzano, M.; Vallet-Regí, M. Mesoporous Silica Nanoparticles for Drug Delivery. Adv. Funct. Mater. 2020, 30, 3–5.

(15) Li, Z.; Barnes, J. C.; Bosoy, A.; Stoddart, J. F.; Zink, J. I. Mesoporous Silica Nanoparticles in Biomedical Applications. Chem. Soc. Rev. 2012, 41, 2590.

(16) Klichko, Y.; Khashab, N. M.; Yang, Y. W.; Angelos, S.; Stoddart, J. F.; Zink, J. I. Improving Pore Exposure in Mesoporous Silica Films for Mechanized Control of the Pores. Microporous Mesoporous Mater. 2010, 132, 435–441.

(17) Hernandez, R.; Franville, A. C.; Minoofar, P.; Dunn, B.; Zink, J. I. Controlled Placement of Luminescent Molecules and Polymers in Mesostructured Sol-Gel Thin Films [10]. J. Am. Chem. Soc. 2001, 123, 1248–1249.

(18) Lu, Y.; Ganguli, R.; Drewien, C. A.; Anderson, M. T.; Jeffrey Brinker, C.; Gong, W.; Guo, Y.; Soyez, H.; Dunn, B.; Huang, M. H.; Zink, J. I. Continuous Formation of Supported Cubic and Hexagonal Mesoporous Films by Sol-Gel Dip-Coating. Nature 1997, 389, 364–368.

(19) Chia, S.; Urano, J.; Tamanoi, F.; Dunn, B.; Zink, J. I. Patterned Hexagonal Arrays of Living Cells in Sol-Gel Silica Films [1]. J. Am. Chem. Soc. 2000, 122, 6488–6489.

(20) Rühle, B.; Saint-cricq, P.; Zink, J. I. Externally Controlled Nanomachines on Mesoporous Silica Nanoparticles for Biomedical Applications. 2016, 1769–1779.

(21) Kumar, N.; Chen, W.; Cheng, C.; Deng, T.; Ruining, W.; Zink, J. I. Stimuli-Responsive Nanomachines and Caps for Drug Delivery. Enzym. 2018, 43, 31–65.

(22) Cheng, C. A.; Deng, T.; Lin, F. C.; Cai, Y.; Zink, J. I. Supramolecular Nanomachines as Stimuli-Responsive Gatekeepers on Mesoporous Silica Nanoparticles for Antibiotic and Cancer Drug Delivery; 2019; Vol. 9.

(23) Chen, W.; Glackin, C. A.; Horwitz, M. A.; Zink, J. I. Nanomachines and Other Caps on Mesoporous Silica Nanoparticles for Drug Delivery. Acc. Chem. Res. 2019, 52, 1531–1542.

(24) Aznar, E.; Oroval, M.; Pascual, L.; Murguía, J. R.; Martínez-Máñez, R.; Sancenón, F. Gated Materials for On-Command Release of Guest Molecules. Chem. Rev. 2016, 116, 561–718.

(25) Croissant, J. G.; Butler, K. S.; Zink, J. I.; Brinker, C. J. Synthetic Amorphous Silica Nanoparticles : Toxicity and Biomedical and Environmental Implications. Nat. Rev. Mater. 2020, 5, 886–90.

Chapter 3. A Thermo-Responsive Nanoparticle Enabled Focused Ultrasound-Stimulated Magnetic Resonance Imaging Spotlight

3.1 Introduction

Magnetic resonance imaging (MRI) is a widely used non-invasive diagnostic technique, and Gd-DTPA (gadolinium-diethylenetriamine pentaacetic acid, the effective component in Magnevist [Bayer]) is widely used to enhance the MRI visibility of tissues of interest.[1,2] MRI-guided high-intensity focused ultrasound (HIFU) is used in clinical practice as a therapeutic tool. Under real-time MRI monitoring, HIFU can achieve precise spatial and temperature control; the HIFU focal point is about 1.5 mm^3. [3–7] To improve efficacy of MRI-guided HIFU, it is essential to accurately identify, or spotlight target tissues for treatment. In this paper, we show that a novel HIFU-modulated MRI nano contrast agent based on mesoporous silica nanoparticles (MSNs), [8,9] combined with Fourier spectral analysis, can distinguish periodic signals from noisy background, enhance the modulated MRI signals and thus spotlight the region of interest.

We designed Gd-DTPA and poly(N-isopropylacrylamide) (PNIPAm) modified MSNs (Gd-P-MSNs) to generate reversible MRI T_1 relaxivity changes based on the mechanism shown in **Figure 3.1**. The T_1 relaxation time can be modulated using HIFU by changing the water access to Gd-DTPA.[10–12] PNIPAm , a thermo-responsive polymer with a lower critical solution temperature (LCST) of 32 ℃ changes its hydrophilicity reversibly. [13,14] It is hydrophilic below the LCST and hydrophobic above it. [15–20] HIFU-induced periodic temperature changes across the LCST of PNIPAm can modulate the hydrophobicity of PNIPAm and the water access to Gd-DTPA and thus modulate T_1-weighted MRI contrast.

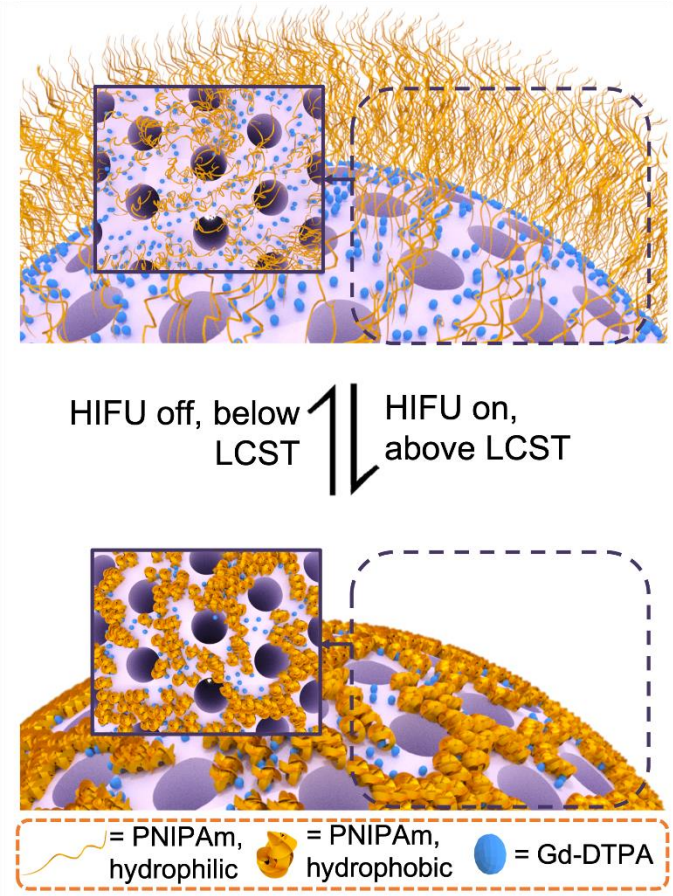

Figure 3.1 Top and side view of Gd-P-MSNs below LCST (top) and above LCST (bottom). When HIFU is on and sample temperature goes above LCST, PNIPAm becomes hydrophobic and shrinks, obstructing water access to Gd-DTPA and leading to longer T_1 relaxation time.

3.2 Results and Discussion

The Gd-P-MSNs was synthesized following previously published protocols shown in **Figure S3.1**.[21] MSNs were about 120 nm in diameter as shown in TEM images (**Figure S 3.2**). They were modified by attaching amine groups mostly on the exterior surface by refluxing them in toluene with 3-aminopropyl triethoxysilane (APTES). The zeta potential changed from negative to positive (**Figure S 3.3**). The EDC/NHS reaction was used to couple carboxylic groups on Gd-DTPA to amine groups on MSNs[22], and the zeta-potential changed from positive to negative due to the

negative charge of Gd-DTPA. The amount of Gd-DTPA attached on MSNs was quantified by ICP-OES. PNIPAm with a carboxylic acid terminal was also attached to amine groups by the EDC/NHS reaction and quantified by TGA (**Figure S 3.4**). The zeta-potential went further negative due to the negative charge of the carboxylic acid terminals of PNIPAm. TEM images showed that the Gd-P-MSNs stayed intact after modification (**Figure S 3.2**). DLS results showed increasing hydrodynamic diameters after each modification step, and the diameter increased at temperature above the LCST due to MSN aggregation caused by hydrophobic PNIPAm on the surface (**Figure S 3.5**). By tuning the amount of Gd-DTPA and PNIPAm, Gd-P-MSNs with various Gd/PNIPAm ratios were synthesized. (**Table S 3.1**.)

The T_1 relaxivity change caused by Gd-P-MSNs was then tested under MRI-guided HIFU. Gd-P-MSNs was dispersed in Mili-Q water and mixed with a tissue-mimicking gel (methyl cellulose, 2 wt%) and milk (50% wt%)[23]. An agarose phantom (3.5 wt%) with cylindrical wells was constructed to hold samples. The experiment setup is shown in **Figure 3.2 (a)**; the agarose phantom was placed on the HIFU transducer and the HIFU focal point was positioned within the sample. An optical temperature probe was also placed in the well. Using a standard 2D Cartesian single-slice gradient echo temperature mapping protocol (echo time [TE]=15 ms, repetition time [TR]=25 ms, flip angle=25°), the temperature increases of the samples were monitored. The control was Magnevist (Mgv) with the same amount of Gd-DTPA as the Gd-P-MSN samples, and the HIFU power and duration were kept constant for all samples and controls. Both T_1-weighted (T_1W) images and T_1 values were obtained before, during, and after HIFU stimulation, and the results from the Gd-P-MSNs are shown in **Figure 3.2 (b)**. As temperature increased during HIFU, the T_1 value increased and the signal intensity of the sample area on the T_1W image decreased. After HIFU, the T_1 value and T_1W intensity returned to the starting points.

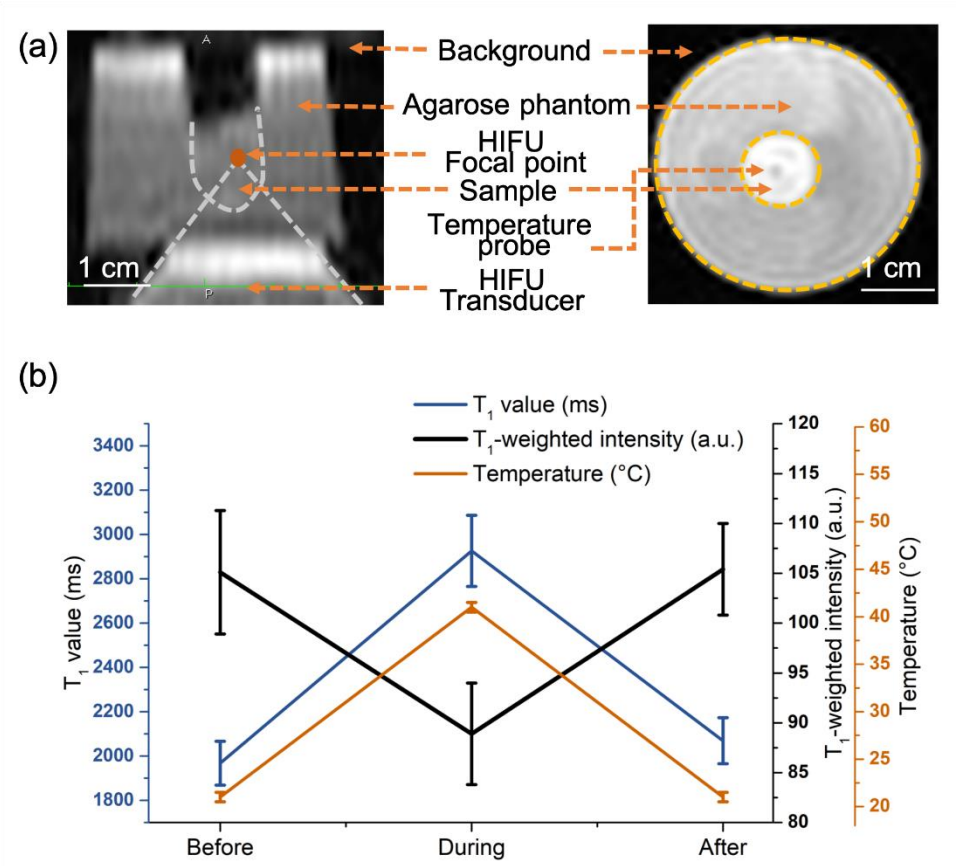

Figure 3.2 (a) Sagittal (left) and coronal (right) views of the MRI-guided HIFU experiment setup. (b) Temperature, intensity of T_1-weighted images and T_1 value changes of the Gd-P-MSN sample before, during, and after HIFU.

In order to quantify and compare the T_1 value change of each sample and control, the T_1 value change percentage ($\Delta T_1\%$) was calculated following the **Equation 3-1**:

$$\Delta T_1\% = \frac{T_{1,during} - T_{1,after}}{T_{1,after}} \times 100\% \quad \text{Equation 3-1}$$

$\Delta T_1\%$ of each sample and control are plotted in **Figure S 3.6**. All samples and controls showed positive $\Delta T_1\%$ during HIFU. The $\Delta T_1\%$ of both Mgv and PNIPAm-modified MSNs (P-MSNs) resulted from the temperature increase during HIFU. The $\Delta T_1\%$ of Gd-P-MSN samples resulted from not only the temperature effect but also the hydrophobicity change of PNIPAm.

During HIFU the temperature increase made PNIPAm hydrophobic and the water access of Gd-DTPA was reduced, resulting in a longer T_1 value. This is supported by the fact that the ΔT_1% of Gd-P-MSNs was much higher than that of Gd-DTPA modified MSNs (Gd-MSNs) without PNIPAm modification (**Figure S 3.7**). We chose the Gd-P-MSNs with the highest ΔT_1% for the following experiments with the same MSN concentration. This sample showed a higher ΔT_1% than the Mgv, which indicates that it can cause more significant MRI contrast changes than the Mgv.

Next, both Gd-P-MSNs and Mgv were tested under periodic MRI-guided HIFU modulation. The HIFU power and repetition pattern were chosen to generate temperature modulation across the LCST within a short time. Gd-P-MSNs were pre-heated to 31 ℃ by HIFU using a power of 24.5 W for 3 min, followed by periodic HIFU stimulation with a power of 18 W to modulate the temperature across the LCST within a 2 ℃ window. Mgv was treated with the same HIFU sequence. The frequency of the periodic HIFU modulation was 0.1 Hz with a 5 s on/off pattern, and the total duration was 100 s (10 cycles). Conventional Cartesian MRI protocols struggle to rapidly measure dynamic signal changes, therefore a 3D stack-of-radial golden-angle-ordered spoiled-gradient-echo multi-echo sequence (10 slices, TR=11.1 ms, six echoes, TE_1=1.43 ms, echo spacing=1.29 ms, flip angle=6°)[24] was used and coupled with a k-space weighted image contrast (KWIC) reconstruction technique (3 radial angles in the centermost annulus and 89 in total)[25] to produce one set of T_1W 3D images every 0.33 s. The temperature was simultaneously measured with this stack-of-radial sequence using the proton resonance frequency method, which was based on frequency and phase changes.[24,26] The Gd-P-MSNs were also scanned with the same stack-of-radial sequence and duration without HIFU modulation as a control (Gd-P-MSNs no HIFU). The synchronized HIFU sequence and T_1W intensity changes of the sample, phantom and background

area of the Gd-P-MSN sample with HIFU modulation (Gd-P-MSNs with HIFU), MSN no HIFU, and Mgv with HIFU modulation (Mgv with HIFU) are shown in **Figure 3.3**. There were no substantial changes in T_1W signal in the phantom or background area in all 3 experiments. T_1W signal changes due to HIFU modulation can be observed in both Gd-P-MSNs with HIFU and Mgv with HIFU, and the frequency of signal change follows that of the HIFU sequence. **Figure 4 (a-c)** show the temperature and T_1W signal changes of the three samples during 100 seconds of periodic HIFU modulation. In both Gd-P-MSNs with HIFU and Mgv with HIFU, temperature and T_1W intensity changes were periodic and correlated: when the temperature increased, the T_1W intensity decreased, which is consistent with the results mentioned above. However, in Gd-P-MSNs no HIFU, the temperature and intensity changes were minor and random. In addition, the periodic T_1W signal changes in Gd-P-MSNs with HIFU were substantially larger than that in Mgv with HIFU.

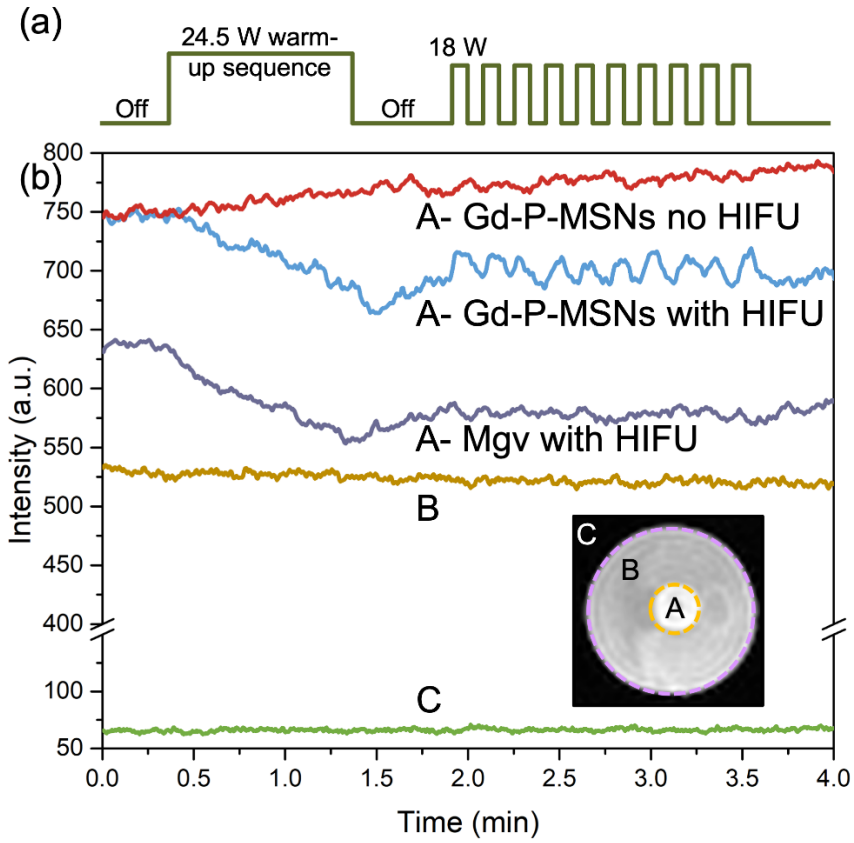

Figure 3.3 (a) Synchronized HIFU sequence applied to the sample region: a warm-up sequence of 24.5 W followed by a periodic HIFU sequence with frequency of 0.1 Hz (18 W, 5 s on and 5 s off, repeated 10 times). (b) T_1W intensity change over time of the sample (region A), phantom (region B) and background (region C) of Gd-P-MSNs with HIFU (blue line), Gd-P-MSNs no HIFU (red line) and Magnevist (Mgv) with HIFU (purple line).

Spectral analysis was then done to construct a modulation enhancement map (MEM) using an offline MATLAB script. For each pixel, the change of its intensity in all dynamic T_1W images were plotted against time, after which a fast Fourier transform was performed to produce a frequency spectrum. **Figure 3.4 (d-f)** show spectra from pixels in the HIFU focal points where the peak having the same frequency (0.1 Hz) as the HIFU modulation is indicated by the arrow. The intensity of this peak was then mapped across the entire imaging field of view to produce a MEM.

The T_1W images before HIFU of Mgv (Mgv T_1W before HIFU) and Gd-P-MSNs (Gd-P-MSNs T_1W before HIFU) are shown in **Figure 3.5 (a)** and **(b)**. **Figure 3.5 (c-e)** show the MEM of Mgv with HIFU, Gd-P-MSNs no HIFU and Gd-P-MSNs with HIFU. Compared to **Figure 3.5 (a)** and **(b)**, the intensity of the agarose phantom was suppressed significantly in all of the MEMs due to absence of periodic intensity modulation, whereas the intensity of the sample region, especially at the HIFU focal point, was enhanced in the MEMs. To quantify the enhancement, contrast difference % (CD%) was calculated using **Equation 3-2**, where μ_A stands for average intensity of region of interest (ROI), which is the sample region (within yellow circle in **Figure 3.5**), μ_B stands for average intensity of the agarose phantom region (annulus between yellow and purple circles in **Figure 3.5**).

$$CD\% = \frac{\mu_A - \mu_B}{\mu_B} \times 100\% \quad \text{Equation 3-2}$$

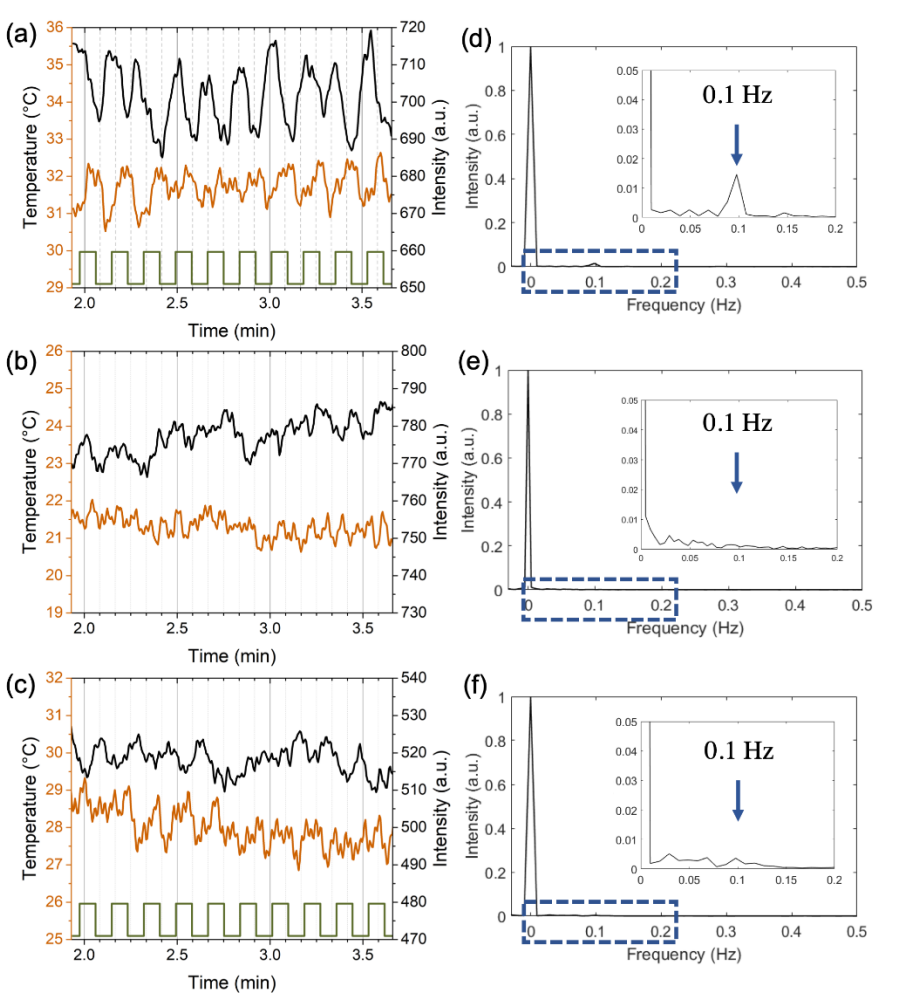

Figure 3.4 Temperature (orange) and T_1W intensity (black) changes of (a) Gd-P-MSNs with HIFU (b) Gd-P-MSNs no HIFU and (c) Mgv with HIFU. All values were average of 9 pixels around the HIFU focal point. (d)-(f) are Fourier transform spectra of T_1W intensity changes vs. time of one pixel on the HIFU focal point in (a)-(c). DC (0 Hz) peak intensity in each spectrum was normalized to 1. The area under the 0.1 Hz peak in (d) is much larger than that in (e) and (f).

The CD% of Gd-P-MSNs with HIFU is 281, which is 30-fold higher than CD% of 9 in Gd-P-MSNs no HIFU, close to 3-fold higher than CD% of 103 in Mgv with HIFU and 25-fold higher than CD% of 11 in Mgv T_1W before HIFU. From MEM of Gd-P-MSNs with HIFU in **Figure 3.5 (e)**, we observe that the CD% at the 1.5 mm^3 HIFU focal point is 912 (ROI showed in **Figure S**

3.8), which is 83-fold higher than CD% of Mgv T_1W before HIFU. This indicates that spectral analysis can efficiently capture the enhancement created by periodic HIFU modulation of Gd-P-MSNs. Also, Gd-P-MSNs clearly exhibits greater enhancement in the MEM than the Mgv undergoing the same periodic HIFU modulation, because it caused more T_1 change during HIFU as explained previously. The T_1W image before HIFU and MEM for Gd-P-MSNs both show several-fold higher CD% than Mgv, and these two could be considered together in a multi-spectral method to further enhance the contrast. MEMs were also constructed from the modulation in first 30 s, and Gd-P-MSNs with HIFU showed 46-fold enhancement compared to Mgv T_1W before HIFU (**Figure S 3.9**). It indicates that significant enhancement can also be achieved using a shorter data acquisition time.

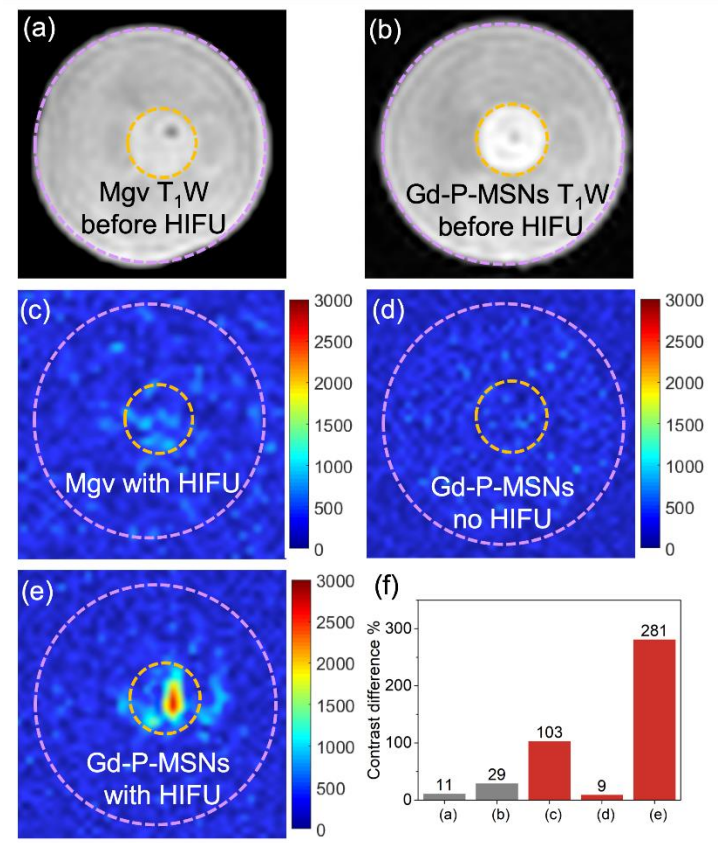

Figure 3.5 T_1W images, modulation enhancement maps (MEMs) and contrast difference% (CD%) of samples and controls. In (a) through (e), the edge of the agarose phantom is delineated with the purple circle (outer circle), and the sample/control region is delineated by a yellow circle (inner circle). (a) and (b) are T_1W images before periodic HIFU of Mgv (Mgv T_1W before HIFU) and Gd-P-MSNs (Gd-P-MSNs T_1W before HIFU). The black spots in (a) and (b) are from temperature probe. (c)-(e) are MEMs of Mgv with HIFU, Gd-P-MSNs no HIFU and Gd-P-MSNs with HIFU. (f) CD% of (a)-(e).

3.3 Conclusions

In summary, we have developed HIFU-responsive Gd-P-MSNs that can generate reversible T_1 relaxivity changes by modulating the hydrophobicity of PNIPAm. Combined with periodic HIFU modulation at 0.1 Hz over 100 s and spectral analysis, the MRI contrast was enhanced by

over an order of magnitude compared to that of Gd-P-MSNs without HIFU modulation, 3 times that of Mgv with HIFU modulation and 83 times that of Mgv with conventional Cartesian T_1W protocols. Our new method integrates these effects with the precise three-dimensional spatial control of the HIFU focal point to "spotlight" the region of interest with highly specific MRI contrast enhancement. The data acquisition time for the experiments in our study was only 100 s, and the small (2 ℃) temperature change would cause minimal tissue damage. This method can be applied in improving the identification of target tissues, such as delineation of the tumor margins, for MRI-guided HIFU therapies.

3.4 Experimental Section

Chemicals

Tetraethylorthosilicate (TEOS; 99%, Aldrich), cetyltrimethylammonium bromide (CTAB; 98%, Aldrich), sodium hydroxide (99%, Fisher Scientific), absolute ethanol (EtOH; Aldrich). 3-aminopropyl triethoxysilane (APTES; 99%, Aldrich), poly(N-isopropylacrylamide) (PNIPAm, carboxylic acid terminated, Mn=7000, Aldrich), EDC•HCl (99%, Covachem), sulfo-NHS (99%, Covachem), diethylenetriaminepentaacetic acid gadolinium(III) dihydrogen salt hydrate (Gd-DTPA; 97%, Aldrich), nitric acid (TraceMetal grade, Fisher), methyl cellulose (4000 cP, Sigma), agarose BP160-100 (Molecular Biology Grade, Fisher) were used as received. Anhydrous toluene was obtained by distillation from CaH_2 under dry nitrogen.

Synthesis of Gd-DTPA and PNIPAm modified MSNs (Gd-P-MSNs)

Synthesis of mesoporous silica nanoparticles (MSNs)

0.25 g CTAB and 875 μL of sodium hydroxide solution (2 M) were dissolved in 120 mL of water under stirring. The solution was heated at 80 °C for 30 minutes, followed by the addition of 1.2 mL of TEOS and 0.79 mL ethyl acetate under vigorous stirring. Stirring was continued for 2 h

at 80 °C, and then the solution was allowed to cool to room temperature. The nanoparticles were collected by centrifugation (15 min at 7830 rpm), washed 3x with ethanol (3x 30 mL) and dispersed in 20 mL ethanol for further use. Approximately 200 mg of MSNs was obtained in each batch.

Amine modification on MSN surface

Around 200 mg unfunctionalized MSNs was washed 3x with toluene (3x 30 mL), and redispersed in 30 mL of dry toluene stirring in a flame-dried 50 mL round bottom flask under nitrogen. Then 120 μL (3-aminopropyl)triethoxysilane was added drop by drop and resulting mixture was refluxed in 110 °C oil bath under nitrogen overnight. The amine-modified MSNs was collected by centrifugation (10 min at 7830 rpm) and washed 3x with ethanol (3x 30 mL). Product was redispersed in 20 mL ethanol for further use.

Extraction of APTES-functionalized MSNs (NH_2-MSNs)

APTES-functionalized MSNs dispersed in toluene were washed 2x with ethanol (2x 30 mL). To extract the organic template from the pores, the nanoparticles were dispersed in 80 mL of an acidic ethanolic solution (EtOH:HCl(conc.) = 90/10 (v/v)), refluxed for 1 h, collected by centrifugation (10 min at 7830 rpm), and repeated above procedure one more time. The product was washed 2x with ethanol (2x30 mL) and stored in ethanol.

Gd-DTPA modification of NH_2-MSNs

NH_2-MSN dispersed in ethanol was washed 3x with DI water (3x 30 mL), then dispersed in HEPES buffer (pH=7.4) for future use. 1.2 mL of Gd-DTPA water solution (0.10 g/mL, pH=6.7) was mixed with 4.8 mL of MES buffer (100 mM, pH = 6.0), 17.2 mg of EDC•HCl and 19 mg of sulfo-NHS, and the mixture was stirred for 20 min. 0.3, 0.6, 2.1, 3 mL of mixture were added to 5 mL of HEPES buffer with 60 mg NH_2-MSN dispersed, and stirred in room temperature for 24 h.

Gd-DTPA modified MSNs (Gd-MSNs) products were washed 3x with DI water (3x 30 mL) and labeled as sample 1 to sample 4 (S1, S2, S3, S4).

PNIPAm modification of Gd-MSNs

Wash S1-S4 with HEPES buffer (20 mL) and redisperse it in 20 mL HEPES buffer for further use. 30 mg of PNIPAm was dissolved in cold MES buffer and stirred for 15 min, then 8.25 mg of EDC•HCl and 9.3 mg of sulfo-NHS were added. The mixture was stirred for one hour in room temperature, then add to 5 mL HEPES buffer with 50 mg of dispersed S1-S4. The mixture was stirred for 24 h, and products were collected by centrifugation (15 min at 7830 rpm) at 20 °C followed by washing 8x with cold DI water (8x 20 mL). S1-S4 were redispersed in 20 mL DI water for further use.

Tissue mimicking gel and MRI-guided HIFU sample preparation

1 g methyl cellulose was slowly added to 15 mL boiled water and stirred for 3 min. Then 25 mL condensed milk was added followed by 10 mL cold water. The mixture was stored in refrigerator overnight to eliminate air bubble. 3 mg Gd-P-MSNs were dispersed in 0.5 mL water and then mixed with 1 mL gel/milk mixture, resulting a 2 mg/mL Gd-P-MSNs gel/milk mixture. The Magnevist (Mgv) control was made by similar method. Mgv was first diluted to 0.5 mL water, then was mixed with 1 mL gel/milk mixture.

Agarose phantom

17.5 g agarose was slowly added to hot water with stirring. Then the solution was heated up to boiling, and then poured to sample holder model. After agarose was solidified under room temperature, it was stored in refrigerator for further use.

Characterization

Transmission electron microscopy (TEM)

TEM images were recorded on a Tecnai T12 Quick CryoEM at an accelerating voltage of 120 kV. A suspension (8 μL) of nanoparticles in ethanol was dropped on a 200 mesh carbon coated copper grid and the solvent was allowed to evaporate at room temperature.

Zeta-potential analysis and dynamic light scattering (DLS)

Zeta-potential analysis and DLS were carried out on a ZetaSizer Nano (Malvern Instruments Ltd., Worcestershire, U.K.) in DI water.

Thermogravimetric analysis (TGA)

TGA was performed using a Perkin-Elmer Pyris Diamond TG/DTA under air (200 mL/min). Approximately 5-10 mg of sample was loaded into aluminum pans. The sample was held at 100 °C for 30 minutes, and then the data were recorded during a temperature scan from 100 to 600 °C at a scan rate of 10 °C/min and an isothermal process of 600 °C for 80 min. The plotted values are normalized to the weight at 100 °C. An empty aluminum pan was used as a reference.

Quantification of Gd-DTPA by inductively coupled plasma atomic emission spectroscopy (ICP-OES)

ICP-OES measurements were made using ICPE-9000 Shimadzu. 0.1 mL of sodium hydroxide solution (2 M) was added to approximately 0.5-1 mg sample (Gd-MSNs or Gd-P-MSNs) dispersed in 0.05 mL of Milli-Q water, and the mixture was sonicated for 1 h. Then 0.05 mL of nitric acid was added, and the mixture was sonicated for 1h. The solution was then diluted to 10 mL with 2% nitric acid for measurement.

MRI-guided HIFU Experiments

All MRI-guided HIFU experiments were conducted using a research-dedicated HIFU system (Image Guided Therapy, Bordeaux, France) integrated with a whole-body 3 T scanner (Prisma,

Siemens Healthineers, Erlangen, Germany). The HIFU system had an 8-element annular transducer array with a diameter of 25 mm, frequency of 2.5 MHz, a focal point of $0.7\times0.7\times3 mm^3$ in size, and a peak electrical power output of 200 W. The electrical power output during experiments ranged from 18 W to 24.5 W.

T_1-weighted images were acquired before and after HIFU stimulation with a 3D Cartesian gradient-echo sequence using the following parameters: field of view (FOV)=$280\times140\times54$ mm^3, matrix size=256×128×18, echo time (TE)=1.89 ms, repetition time (TR)=5 ms, flip angle=10°. T_1 relaxation times were measured before, during, and after HIFU stimulation using a Cartesian variable flip angle sequence with the following parameters: FOV=$180\times90\times48$ mm^3, matrix size=192×96×16, TE=2.29 ms, TR=6 ms, flip angles=1, 2, 5, 7 and 9°. To correct B_1+ field variations, a separate B_1 mapping protocol was ran before, during, and after HIFU with matching FOV and matrix size with the T_1 mapping protocol and TE=1.87 ms, TR=2 s and flip angle=10°. These images were reconstructed in-line with the scanner software. A standard DESPOT1 T_1 fitting algorithm[27] was then carried out in an offline MATLAB 2018a (MathWorks, Natwick, MA) script to produce 3D T_1 maps. They were saved as DICOM images and imported into Horos where regions of interest (ROIs) of 9 voxels in size were carefully drawn to exclude the thermal probe and/or air bubbles inside the heated region of the sample to compute the average T_1 value.

For simultaneous acquisition of the change in temperature and T_1-weighted image signal, a 3D multi-echo gradient-echo stack-of-radial sequence was used with FOV=$109\times109\times30$ mm^3, matrix size=96×96×10, six echoes, $TE_1/\Delta TE$=1.43/1.29 ms, TR=11.1 ms, flip angle=6° and number of radial spokes=3000. Reconstruction was performed offline in MATLAB. To increase the temporal resolution, a k-space weighted image contrast (KWIC) filter was employed with eight annuli in total and the number of spokes in each annulus following the Fibonacci numbers[25], e.g.,

3 (innermost annulus), 5, 8, 13, 21, 34, 55 and 87 (outermost annulus). The filter then moved 5 radial spokes at a time for a temporal resolution of 0.33 s and a temporal footprint of 9.88 s. Gridding, density compensation, and coil combination then followed to produce magnitude and phase images[28]. Magnitude images of all echoes were combined with sum-of-squares and a fast Fourier transform was performed on a voxel-by-voxel basis along the time dimension for spectral analysis and producing the modulation enhancement map (MEM). Phase images of all echoes were also combined to an effective TE=10 ms and relative temperature change was extracted from the phase difference between a dynamic image acquired at a time point *t* and the first dynamic image at baseline temperature before HIFU ablation using $\Delta T(t) = \frac{\Phi_t - \Phi_0}{\alpha \cdot TE \cdot \gamma \cdot B_0}$, where ΔT is the change in temperature at *t*, Φ_t is the phase at *t*, Φ_0 is the phase of the first dynamic image, α is the proton resonant frequency shift (PRF) temperature coefficient of -0.01 ppm/°C, TE is the effective echo time (10 ms in this study), γ is the gyromagnetic ratio of protons (267.522×10^6 rad·s^{-1}·T^{-1}), and B_0 is the magnetic field strength. Similar to the measurement of T_1 relaxation times, ROIs of 9 voxels in size were drawn to compute the average relative temperature change and magnitude change. The same ROIs were also transferred to MEMs to measure the intensity of the 0.1 Hz peak. For comparison, ROIs of 9 voxels and 100 voxels were drawn in unheated regions of the agar gel phantom and background noise, respectively, in the same images.

3.5 Supporting Information

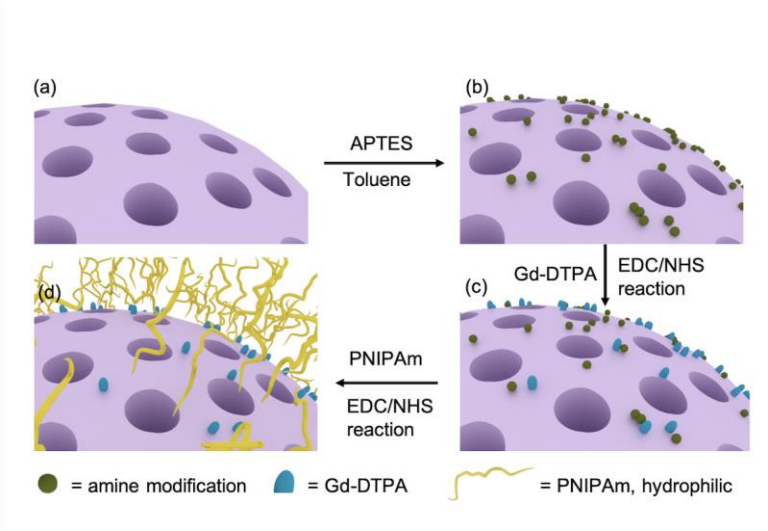

Figure S 3.1 Synthesis route of Gd-P-MSNs. (a) bare MSNs (b) amine modified MSNs (NH2-MSNs) (c) Gd-DTPA modified MSNs (Gd-MSNs) (d) Gd-P-MSNs

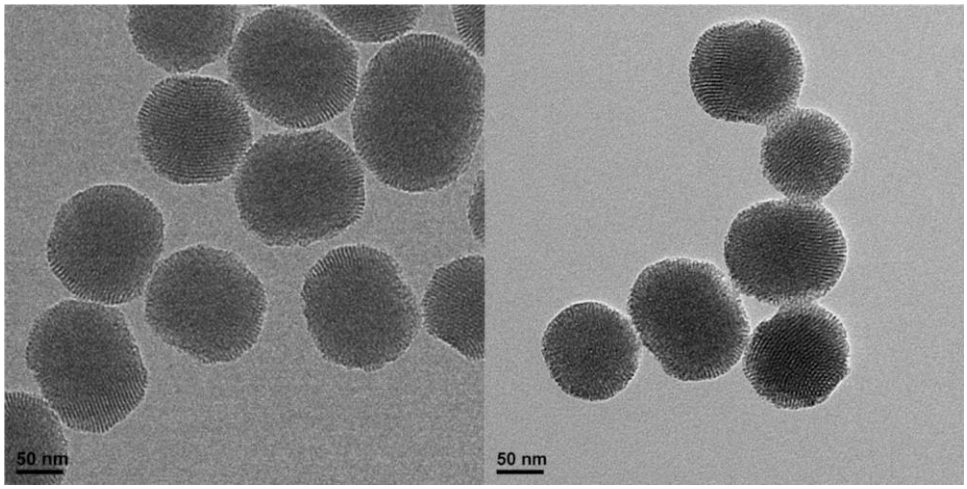

Figure S 3.2 TEM images of bare MSNs (left) and Gd-P-MSNs (right). MSNs stay intact after all modification steps.

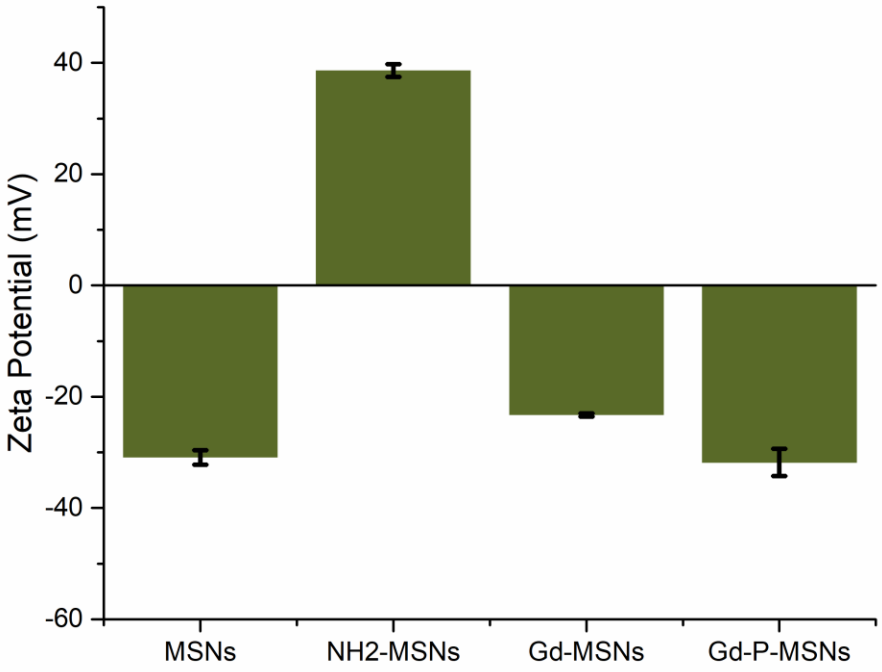

Figure S 3.3 Zeta-potential results after each modification step.

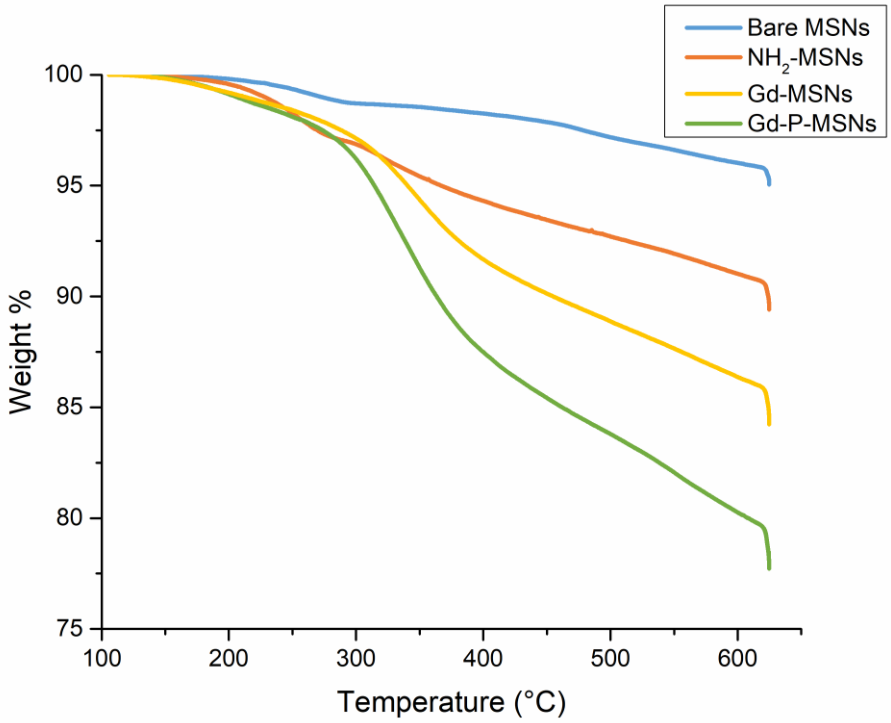

Figure S 3.4 TGA results after each modification step.

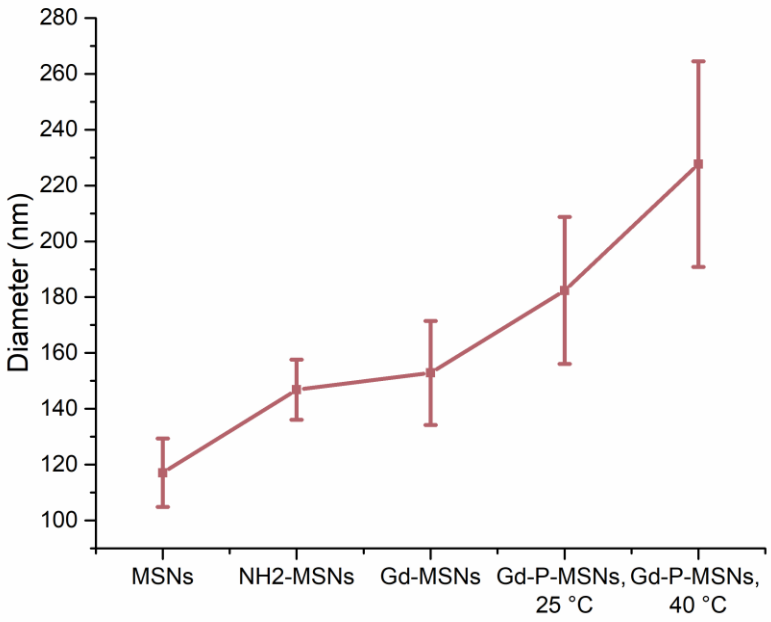

Figure S 3.5 DLS results after each modification step. Gd-P-MSNs showed larger diameter at 40 °C than 25 °C due to aggregation.

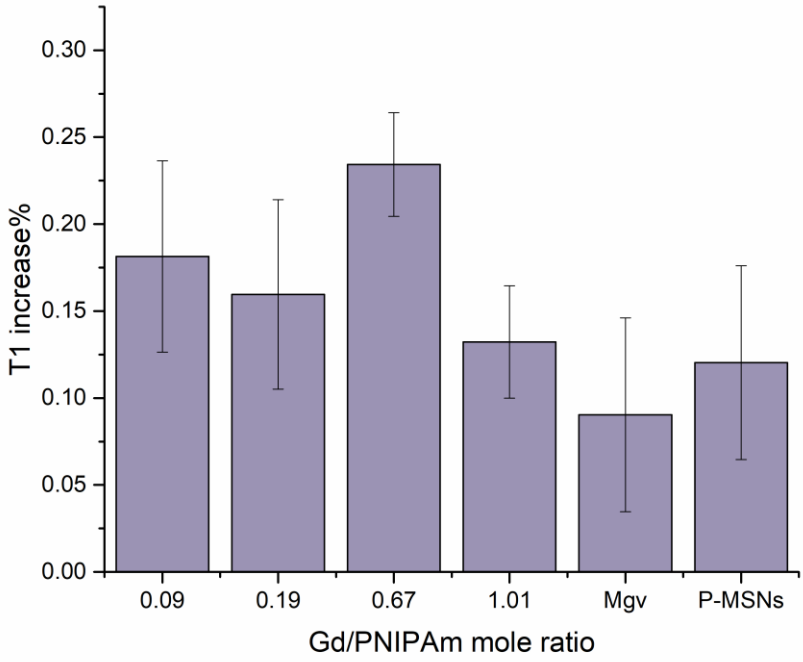

Figure S 3.6 ΔT_1% of Gd-P-MSNs with different Gd/PNIPAm mole ratio and Magnevist control (Mgv) and PNIPAm modified MSNs (P-MSNs) control.

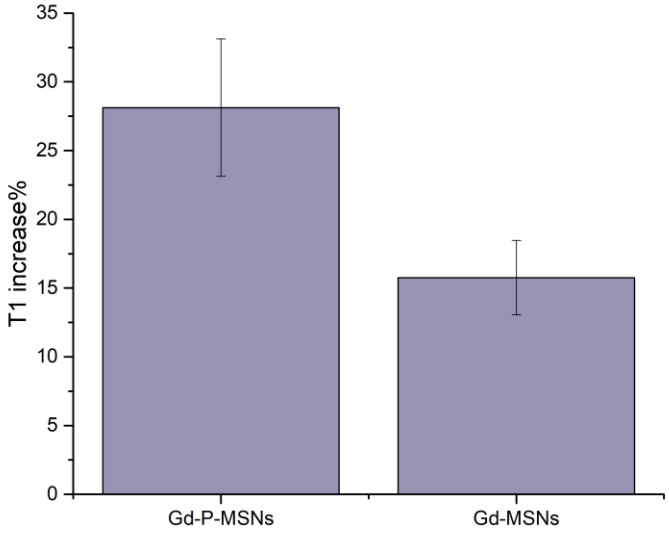

Figure S 3.7 ΔT_1% of Gd-P-MSNs and Gd-MSNs control

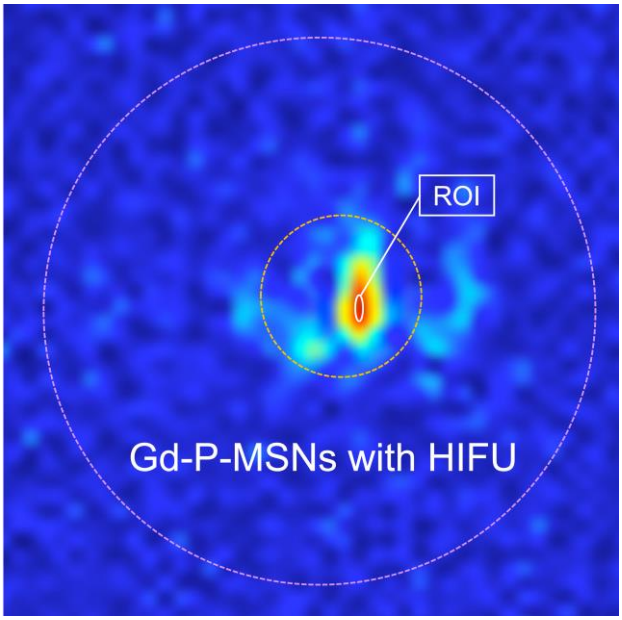

Figure S 3.8 ROI of the HIFU focal point.

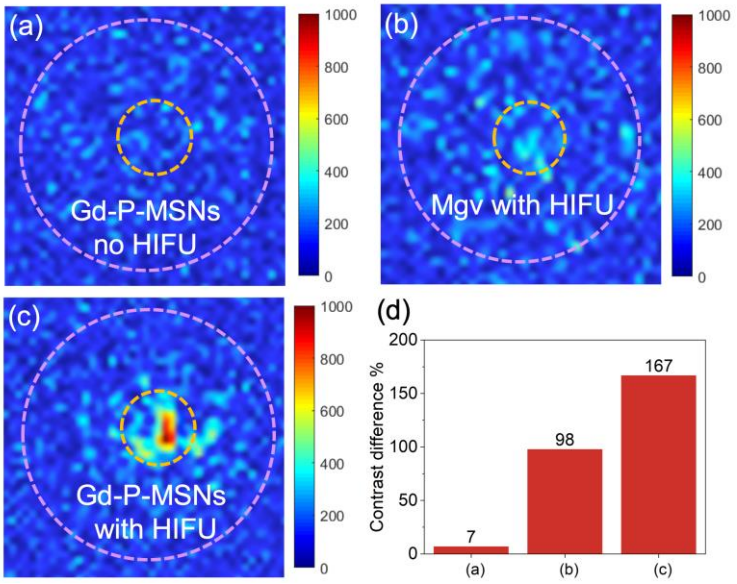

Figure S 3.9 Modulation enhancement maps (MEMs) constructed from the modulation in first 30 s and contrast difference% (CD%) of samples and controls. In (a) through (c), the edge of the agarose phantom is delineated with the purple circle (outer circle), and the sample/control region is delineated by a yellow circle (inner circle). (a)-(c) are MEMs of Gd-P-MSNs no HIFU, Mgv with HIFU and Gd-P-MSNs with HIFU. (d) CD% of (a)-(c). The CD% of Gd-P-MSNs with HIFU

is 167, which is 23-fold higher than CD% of 7 in Gd-P-MSNs no HIFU, close to 2-fold higher than CD% of 98 in Mgv with HIFU and 15-fold higher than CD% of 11 in Mgv T1W before HIFU in Fig. 5 (a). From MEM of Gd-P-MSNs with HIFU in Fig. S9 (c), we observe that the CD% at the 1.5 mm^3 HIFU focal point is 512 (ROI showed in Fig. S8), which is 46-fold higher than CD% of Mgv T_1W before HIFU.

Table S 3.1 Gd-P-MSNs sample 1 (S1) to sample 4 (S4) with different Gd-DTPA/PNIPAm mole ratio.

	Gd-DTPA/MSNs wt %	**PNIPAm/MSNs wt %**	**Gd/PNIPAm mole ratio**
S1	0.09%	17.55%	0.09
S2	0.18%	16.58%	0.20
S3	0.58%	15.54%	0.67
S4	0.83%	14.54%	1.01

Wt%: weight percentage normalized to bare MSNs

3.6 References

(1) Caravan, P.; Ellison, J. J.; Mcmurry, T. J.; Lauffer, R. B. Gadolinium (III) Chelates as MRI Contrast Agents : Structure , Dynamics , and Applications. **1999**, *99*, 2293−2352.

(2) Verwilst, P.; Park, S.; Yoon, B.; Kim, J. S. Recent Advances in Gd-Chelate Based Bimodal Optical / MRI Contrast Agents. *Chem Soc Rev* **2015**, 1791–1806.

(3) Tang, H.; Guo, Y.; Peng, L.; Fang, H.; Wang, Z.; Zheng, Y.; Ran, H.; Chen, Y. *In Vivo* Targeted, Responsive, and Synergistic Cancer Nanotheranostics by Magnetic Resonance Imaging-Guided Synergistic High-Intensity Focused Ultrasound Ablation and Chemotherapy. *ACS Appl. Mater. Interfaces* **2018**, *10*, 15428–15441.

(4) Huang, H. Y.; Hu, S. H.; Hung, S. Y.; Chiang, C. S.; Liu, H. L.; Chiu, T. L.; Lai, H. Y.; Chen, Y. Y.; Chen, S. Y. SPIO Nanoparticle-Stabilized PAA-F127 Thermosensitive

Nanobubbles with MR/US Dual-Modality Imaging and HIFU-Triggered Drug Release for Magnetically Guided *in Vivo* Tumor Therapy. *J. Control. Release* **2013**, *172*, 118–127.

(5) Kim, D. H.; Vitol, E. A.; Liu, J.; Balasubramanian, S.; Gosztola, D. J.; Cohen, E. E.; Novosad, V.; Rozhkova, E. A. Stimuli-Responsive Magnetic Nanomicelles as Multifunctional Heat and Cargo Delivery Vehicles. *Langmuir* **2013**, *29*, 7425–7432.

(6) Lorenzato, C.; Cernicanu, A.; Meyre, M. E.; Germain, M.; Pottier, A.; Levy, L.; de Senneville, B. D.; Bos, C.; Moonen, C.; Smirnov, P. MRI Contrast Variation of Thermosensitive Magnetoliposomes Triggered by Focused Ultrasound: A Tool for Image-Guided Local Drug Delivery. *Contrast Media Mol. Imaging* **2013**, *8*, 185–192.

(7) Chen, Y.; Chen, H.; Sun, Y.; Zheng, Y.; Zeng, D.; Li, F.; Zhang, S.; Wang, X.; Zhang, K.; Ma, M.; He, Q.; Zhang, L.; Shi, J. Multifunctional Mesoporous Composite Nanocapsules for Highly Efficient MRI-Guided High-Intensity Focused Ultrasound Cancer Surgery. *Angew. Chemie - Int. Ed.* **2011**, *50*, 12505–12509.

(8) Lu, J.; Liong, M.; Li, Z.; Zink, J. I.; Tamanoi, F. Biocompatibility, Biodistribution, and Drug-Delivery Efficiency of Mesoporous Silica Nanoparticles for Cancer Therapy in Animals. *Small* **2010**, *6*, 1794–1805.

(9) Tarn, D.; Ashley, C. E.; Xue, M. I. N.; Carnes, E. C.; Zink, J. I.; Brinker, C. J. Mesoporous Silica Nanoparticle Nanocarriers: Biofunctionality and Biocompatibility. *Acc. Chem. Res.* **2013**, *46*.

(10) De Leõn-Rodríguez, L. M.; Martins, A. F.; Pinho, M. C.; Rofsky, N. M.; Sherry, A. D. Basic MR Relaxation Mechanisms and Contrast Agent Design. *J. Magn. Reson. Imaging* **2015**, *42*, 545–565.

(11) Ni, D.; Bu, W.; Ehlerding, E. B.; Cai, W. Engineering of Inorganic Nanoparticles Asmagnetic Resonance Imaging Contrast Agents. *Chem. Soc. Rev.* **2017**, *46*, 7438–7468.

(12) Bruckman, M. A.; Yu, X.; Steinmetz, N. F. Engineering Gd-Loaded Nanoparticles to Enhance MRI Sensitivity via T1 Shortening. **2013**.

(13) Schild, H. G. Poly (N-Isopropylacrylamide): Experiment , Theory and Application. *Prog. Polym. Sci.* **1992**, *17*, 163–249.

(14) Vanparijs, N.; Nuhn, L.; De Geest, B. G. Transiently Thermoresponsive Polymers and Their Applications in Biomedicine. *Chem. Soc. Rev.* **2017**, *46*, 1193–1239.

(15) Chang, J. H.; Kim, J.; Lee, H. PNIPAm Grafted Amino-Functionalized Mesoporous Silica for Thermo-Responsive Chromium Elimination. *Appl. Surf. Sci.* **2017**, *424*, 115–121.

(16) Brunella, V.; Jadhav, S. A.; Miletto, I.; Berlier, G.; Ugazio, E.; Sapino, S.; Scalarone, D. Hybrid Drug Carriers with Temperature-Controlled on – off Release : A Simple and Reliable Synthesis of PNIPAM-Functionalized Mesoporous Silica Nanoparticles. *REACT* **2016**, *98*, 31–37.

(17) Stroeve, P.; Yu, E.; Galiana, I.; Martínez-má, R.; Marcos, M. D.; Aznar, E.; Sancenón, F.; Murguía, J. R.; Amorós, P. Poly (N -Isopropylacrylamide) -Gated Fe3O4/SiO2 Core Shell Nanoparticles with Expanded Mesoporous Structures for the Temperature Triggered Release of Lysozyme. *Colloids Surfaces B Biointerfaces* **2015**, *135*, 652–660.

(18) Yang, Y.; Li, J. Lipid, Protein and Poly(NIPAM) Coated Mesoporous Silica Nanoparticles for Biomedical Applications. *Adv. Colloid Interface Sci.* **2014**, *207*, 155–163.

(19) You, Y. Z.; Kalebaila, K. K.; Brock, S. L.; Oupický, D. Temperature-Controlled Uptake and Release in PNIPAM-Modified Porous Silica Nanoparticles. *Chem. Mater.* **2008**, *20*, 3354–3359.

(20) Yang, Y.; Yan, X.; Cui, Y.; He, Q.; Li, D.; Wang, A.; Fei, J.; Li, J. Preparation of Polymer-Coated Mesoporous Silica Nanoparticles Used for Cellular Imaging by a “Graft-from” Method. **2008**, 5731–5737.

(21) Ruehle, B.; Clemens, D. L.; Lee, B.-Y.; Horwitz, M. A.; Zink, J. I. A Pathogen-Specific Cargo Delivery Platform Based on Mesoporous Silica Nanoparticles. *J. Am. Chem. Soc.* **2017**, *139*, 6663–6668.

(22) Fischer, M. J. E. Amine Coupling Through EDC/NHS: A Practical Approach. In *Surface Plasmon Resonance Methods and Protocols*; 2010; pp 55–73.

(23) Demitri, C.; Sannino, A.; Conversano, F.; Casciaro, S.; Distante, A.; Maffezzoli, A. Hydrogel Based Tissue Mimicking Phantom for In-Vitro Ultrasound Contrast Agents Studies. **2008**, 338–345.

(24) Zhang, L.; Armstrong, T.; Li, X.; Wu, H. H. A Variable Flip Angle Golden-angle-ordered 3D Stack-of-radial MRI Technique for Simultaneous Proton Resonant Frequency Shift and T1-based Thermometry. *Magn. Reson. Med.* **2019**.

(25) Song, H. K.; Dougherty, L. K-Space Weighted Image Contrast (KWIC) for Contrast Manipulation in Projection Reconstruction MRI. *Magn. Reson. Med.* **2000**, *832*, 825–832.

(26) Rieke, V.; Pauly, K. B. MR Thermometry. *J. Magn. Reson. Imaging* **2008**, *27*, 376–390.

(27) Deoni, S. C. L.; Rutt, B. K.; Peters, T. M. Rapid Combined T 1 and T 2 Mapping Using Gradient Recalled Acquisition in the Steady State. **2003**, *526*, 515–526.

(28) Svedin, B. T.; Payne, A.; Jr, B. D. B.; Parker, D. L. Multiecho Pseudo-Golden Angle Stack of Stars Thermometry With High Spatial and Temporal Resolution Using k-Space Weighted Image Contrast. **2018**, *1419*, 1407–1419.

Chapter 4. Pluronic Polymer Functionalized Nanoparticles to Enable a Focused Ultrasound-Stimulated Magnetic Resonance Imaging Spotlight

4.1 Introduction

High-intensity focused ultrasound (HIFU) in conjunction with magnetic resonance imaging (MRI) is being studied and used worldwide as a non-invasive therapeutic tool to treat cancers.[1–3] MRI is a non-invasive volumetric imaging technology that does not involve ionizing radiation and provides a powerful suite of contrast mechanisms to depict anatomy, characterize function and physiology, and measure tissue properties, including temperature changes. MRI-guided HIFU (MRIgHIFU) has been approved by the U.S. Food and Drug Administration (FDA) for several clinical indications since 2004.[4–6] Ultrasound can propagate noninvasively to tissues within the body and be focused on a region of interest as small as 1.5 mm^3. Two important effects of HIFU are local heating and cavitation. The local heating at the HIFU focal point enables hyperthermia and ablation therapies with temperature increase controlled by HIFU amplitude and duration.[7] In addition, the mechanical effects of HIFU are utilized to cause cavitation, chemical bond breaking, and/or mechanical disruption to eliminate target tissues.[8]

The contrast in an MR image is essential for visualizing anatomical structures and identifying target tissue regions. MRI contrast is frequently enhanced for clinical applications by administering paramagnetic molecules (e.g. Gadolinium complexes)[9] to decrease the spin-spin relaxation time (T_1) or superparamagnetic nanoparticles (e.g. superparamagnetic iron oxide nanoparticles, SPIONs)[10] to decrease the spin-lattice relaxation time (T_2). Improving image contrast in the region of interest and developing better contrast agents and techniques is an active

area of research, since improved depiction of the tissue structure for diagnosis further informs the therapeutic strategy.

Many experimental methods have been developed to enhance and/or amplify a weak signal in the presence of a noisy background. A robust and well-known method is to modulate the desired signal and use a boxcar integrator or lock-in amplifier to periodically capture the desired signal in the time interval when its amplitude is at a maximum.[11,12] To use this technique, the desired signal is modulated (pulsed) and collected periodically at its maxima and accumulated over a desired time. In a more general view of this process, the periodic signal is Fourier transformed and the coefficient of the time domain Fourier component at the modulation frequency is the equivalent of the accumulated signals from the boxcar integrator.[11]

We aimed to apply the afore mentioned ideas in an integrated approach to significantly enhance MRI signals and resulting contrast during a HIFU procedure. One of our main ongoing research objectives is to use HIFU to deliver drugs from nanoparticles by using caps to trap drugs and HIFU to open the caps and release drugs.[13,14] There are also many works utilizing the thermal and/or mechanical effects of HIFU to trigger drug release from nanoparticles.[15–18] We hypothesized that an alternative perspective could have unique advantages – using caps to exclude solvent molecules and open the caps to allow water to enter. If a contrast agent were immobilized on a nanoparticle and water access were controlled, the contrast would change as water access changed. We attached caps to nanoparticles that could reversibly open and close in response to HIFU and thereby rapidly and reversibly change MRI contrast. These studies provided the impetus to specifically design and evaluate responsive nanoparticles for HIFU modulation-based amplification of MRI contrast.

Combining the concepts described in the previous paragraphs, we developed a "Spotlight MRI" method to enhance the MRI contrast at the HIFU focal point by creating and capturing periodic MRI contrast changes mediated by responsive nanoparticles.[19] In addition to requiring access to an integrated MRIgHIFU instrument, three technical requirements must be met. First, the HIFU must be pulsed with reasonably short "on" and "off" times for multiple repetitions. Second, the MRI detector must be able to rapidly acquire a series of dynamic images to capture the periodic signal and contrast changes. Finally, for maximum effect, an appropriate nanomaterial that responds to HIFU and changes the MRI signal periodically must be designed.

Nanoparticles that can cause significant T_1 signal and contrast changes are required to maximize the signal and contrast enhancement using our spotlight MRI technique. In our previous communication, we achieved significant contrast enhancement by our spotlight technique using mesoporous silica nanoparticles (MSNs) functionalized with a thermo-responsive polymer.[19] The water access of the gadolinium-diethylenetriamine pentaacetic acid (Gd-DTPA) attached to the surface of MSNs was altered reversibly by the polymer. To further alter the water access to Gd-DTPA, we used Pluronic polymers for our new MSN design in this study. Pluronic polymers, or Poloxamers, are a family of triblock polymers consisting of hydrophobic poly(propylene oxide) (PPO) and hydrophilic poly(ethylene oxide) (PEO). The A-B-A block structure makes the polymer amphiphilic in aqueous solution. Because of their biocompatibility and self-assembly properties, they have been widely used in micelle drug delivery systems[20–23] and gene transfection.[24,25] Pluronic micelles are reported to be ultrasound-responsive, and the micelle disruption is reversible under an appropriate ultrasound dose. [26–28] MSNs are used as carriers in ultrasound-responsive drug delivery systems for its tunable particle and pore size, large surface area, flexibility for surface functionalization, good biocompatibility, and stability upon ultrasound stimuli.[29]

In this paper we discuss in detail how to amplify the image contrast enhancement, characterized by contrast-to-noise ratio (CNR), in an MR image by two orders of magnitude using HIFU stimulation with pulsed modulation. We report our design of a nanoparticle based on Pluronic polymers and Gd-DTPA modified MSNs (Pluronic-Gd-MSNs), which responds to HIFU modulation by repetitively changing the local T_1. In addition, we discuss the design and parameter choices of our spectral signal processing method based on the temporal Fourier transform from a dynamic series of images from an MRI "detector" to "spotlight" a specific region of interest in three-dimensional space with dimensions as small as 1.5 mm^3.

4.2 Results and Discussion

Overview of the spotlight MRI technique

The essence of the spotlight MRI method is shown in **Scheme 4.1**. The T_1-weighted (T_1W) MR images undergoing HIFU stimuli are shown in **Scheme 4.1 (a)**. The T_1W intensity at the HIFU focal point changes in response to repetitive HIFU stimulation, and is extracted and shown as a sinusoidal wave in the time domain in (b) (blue line). The HIFU modulation scheme is shown as a square wave (green line). The repetition rate in this illustration is 0.16 Hz. Using carefully selected parameters, we used a dynamic 3D stack-of-radial MRI technique we have developed to increase the temporal sampling rate and capture multiple data points within each HIFU modulation cycle [19,30,31] as shown in (c), which enabled subsequent processing to extract the modulated contrast enhancement. The addition of HIFU-responsive nanomaterial further enhances the T_1W intensity changes during HIFU modulation, shown in (d). **Scheme 4.1 (e)** shows the temporal Fourier transform of the time-dependent signal from the dynamic MR image series. The intensity of the spectral peak at 0.16 Hz carries the information about the amplified MR image signal and contrast. To reconstruct a modulation enhancement map (MEM), the intensity of the 0.16 Hz peak

of each pixel is used as the signal intensity at the corresponding pixel on MEM. After mapping the entire image, regions of interest where T_1W signal intensity fluctuates at the same frequency as the HIFU modulation can then be identified and enhanced as shown in (f). In this way, periodic MRI contrast change can be differentiated from background regions and enhanced. An MEM with enhancement of one hundred-fold can be reconstructed from less than 2 minutes of data acquisition. An overlay of the MEM and the original T_1W image shown in (g) highlights the location with enhanced MR image contrast, which can be useful for biomedical applications.

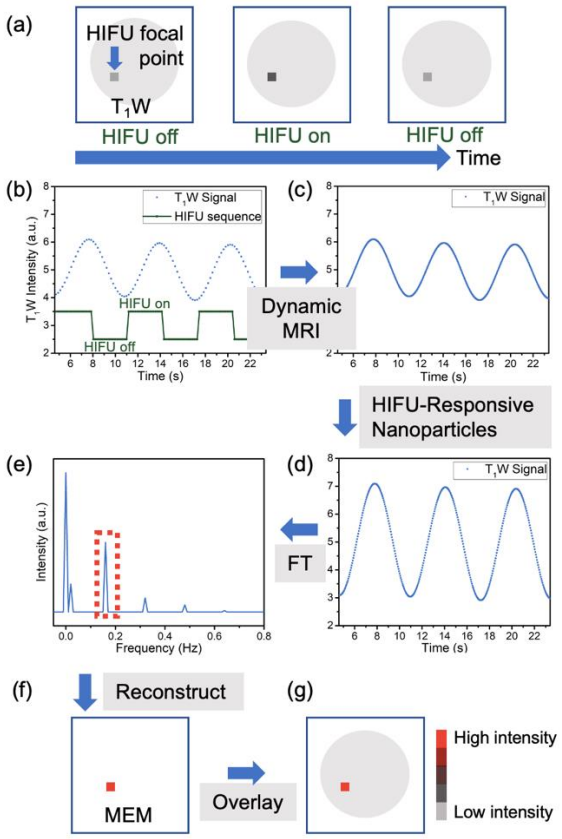

Scheme 4.1 Spotlight MRI contrast enhancement using our dynamic 3D stack-of-radial MRI technique, HIFU-responsive nanoparticles, and spectral signal processing: (a) Conceptual illustration of T_1W image series shows periodic intensity change at the HIFU focal point; (b) extracted T_1W intensity change (blue) at the HIFU focal point over time with HIFU modulation (green); (c) using 3D stack-of-radial MRI, the temporal sampling rate can be increased and more

data points can be collected within each time period; (d) addition of HIFU-responsive nanoparticles can amplify the T_1W signal change; (e) temporal Fourier Transform (FT) of T_1W signal over time in (d), in which the signal at the HIFU modulation frequency is extracted at each spatial location and used to reconstruct MEM in (f); (g) overlay of (f) on the original T_1W image shows the region of interest being spotlighted against the background.

Rapid dynamic 3D MRI

Spotlight MRI relies on rapid dynamic 3D imaging to capture the changes in MRI contrast caused by responsive nanoparticles during periodic HIFU modulation. To overcome the limitations of conventional Cartesian MRI for rapid dynamic imaging, we used our recently developed non-Cartesian 3D stack-of-radial MRI technique and refined the parameter choices to balance spatial resolution (the physical size that a pixel in an image represents) and temporal resolution (the time interval or rate at which data or images are acquired, reconstructed, or displayed). See the Supplementary Notes and **Figures S 4.1-S 4.2** in Supporting Information for an overview of non-Cartesian radial MRI for rapid dynamic imaging.

We have developed a 3D stack-of-radial MRI technique that achieves large volumetric coverage (e.g., 320x320x48 mm^3) while maintaining high spatial (e.g., 1.67x1.67x3 mm^3) and temporal resolutions (e.g., 910 ms per 3D volume) for dynamic imaging during MRI-guided HIFU.[19,30,31] To improve the flexible trade-offs between spatial and temporal resolution in radial MRI, we implemented golden-angle-ordering of the radial spokes (i.e. continuously incrementing the angle of the radial spokes by 111.25° throughout the acquisition)[32] as shown in **Figure 4.1 (a)** and a sliding-window image reconstruction with a k-space weighted image contrast (KWIC) spatiotemporal filter as shown in **Figure 4.1 (b)**.[33] Golden-angle-ordered radial sampling ensures that the flexible selection of almost any subset of radial angles acquired during the dynamic scan

has favorable k-space (i.e., the spatial Fourier transform space in which raw MRI data is acquired) coverage for reconstructing an image frame. The sliding-window reconstruction has two key parameters: the number of radial spokes included to reconstruct an image frame (i.e., temporal footprint, Tf, in ms) and the update rate (i.e., temporal resolution, Tres, in ms) for "sliding" the reconstruction window along the stream of acquired data. The temporal resolution determines how frequently new image frames are reconstructed for monitoring the dynamic process. The Tf determines how faithfully the reconstructed image frames represent the dynamic process: a wider Tf has less k-space undersampling and higher spatial resolution and image quality, but may have a mixture of information as the dynamic process evolves throughout the duration of the Tf (**Figure S 4.2**). To improve the reconstruction of each dynamic image frame, we use a KWIC filter to emphasize the central k-space data (and image contrast) from the most up-to-date radial spokes in the sliding window while including the peripheral k-space data from older spokes to improve the spatial resolution and reduce undersampling artifacts.

As temperature changes are common during HIFU procedures, it is a critical property to monitor to ensure safety and characterize performance. This is especially important during rapid HIFU modulation, since temperature changes occur on the scale of a few seconds and vary across the object. MRI has the unique capability to non-invasively measure spatially resolved maps of temperature changes. The most widely used method is based on the proton resonance frequency shift (PRF).[34,35] See the Supplementary Notes in Supporting Information for an overview of PRF temperature mapping.

Our 3D stack-of-radial dynamic MRI technique simultaneously measures PRF-based temperature maps and captures the T_1W contrast changes over time caused by the MSN state changes during HIFU modulation.[19,30,31] The contrast changes at each image pixel are then

analyzed using temporal Fourier analysis to extract the spectral response and calculate MEM. Our previous study demonstrated the initial performance of our dynamic imaging technique for spotlight MRI[19] and further investigation is conducted in this work to optimize the choice of Tf and Tres for specific experimental settings.

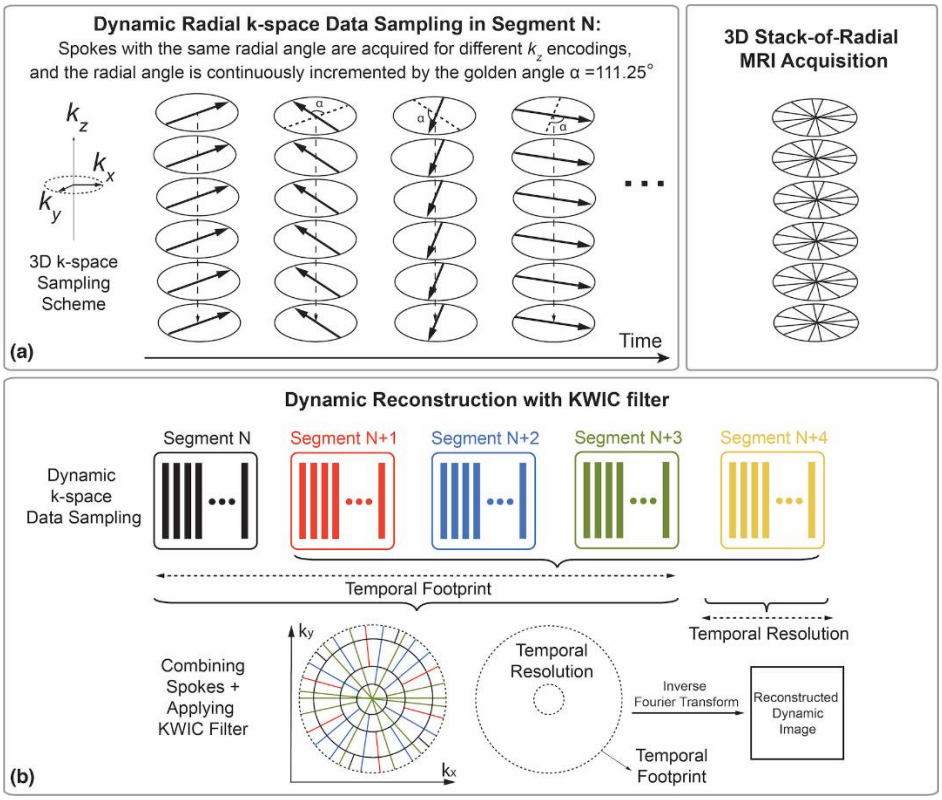

Figure 4.1 Dynamic 3D stack-of-radial MRI k-space data sampling by rotating radial readout spokes based on the golden angle increment over time. (b) A k-space weighted image contrast (KWIC) filter is applied to each selected subset of radial spokes from different segments with certain temporal resolution and footprint to reconstruct dynamic image frames.

Nanoparticle design, synthesis and characterization

The rapid and repetitive changes in T_1 mediated by the nanoparticle in response to HIFU is the fundamental source of intensity changes in the MR images for spotlight MRI. Thus, we carefully designed, synthesized and characterized the nanomaterials that can enable maximum

MRI signal change. MSNs are synthesized and amine-functionalized by the method reported by our group previously.[36] From the TEM images shown in **Figure S 4.3 (a)**, the diameter of MSNs is around 120 nm. The MSN surface modification route is shown in **Figure S 4.4**. Gd-DTPA is coupled to amine-functionalized MSNs (NH_2-MSNs) by the EDC/NHS reaction. Pluronic polymer is coupled to 3-(triethoxysilyl)propyl isocyanate first, and then bonded to Gd-DTPA modified MSNs (Gd-MSNs) by Si-O-Si condensation.

Both Gd-DTPA and the hydrophobic tail of the Pluronic polymer are chemically bonded on the outer surface of MSNs as shown in **Figure 4.2 (b)**. **Figure 4.2 (c)** illustrates the mechanism of the reversible HIFU-responsive MRI contrast change: when HIFU is off, the Gd-DTPA is surrounded by the hydrophobic tail of Pluronic polymer, and therefore water has less access to the Gd-DTPA resulting in longer T_1 relaxation time. During HIFU stimulation, HIFU will vibrate the polymer chain and generate cavities. At this time, the water permeability of Pluronic polymer layer is increased, thus the water access to Gd-DTPA is increased, which leads to a shorter T_1 relaxation time. Because the Pluronic polymer is chemically bonded to MSNs, the polymer layer structure will recover immediately after HIFU is turned off, and the T_1 relaxation time will return to the initial value. Therefore, by applying periodic HIFU stimuli, the Pluronic-Gd-MSNs can generate reversible T_1 contrast changes. Using our spectral signal processing method,[19] the MRI contrast at the HIFU focal point will be significantly enhanced.

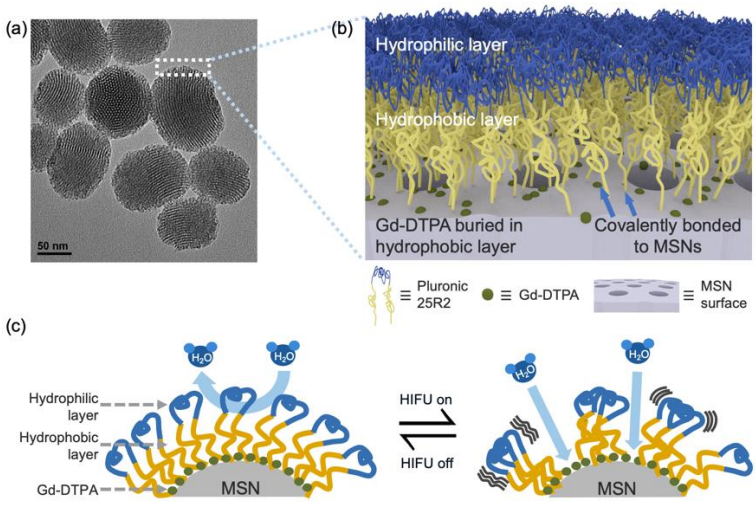

Figure 4.2 (a) TEM image of Pluronic (25R2) and Gd-DTPA modified MSNs; (b) 3D sketch of MSN surface modifications; (c) illustration of Pluronic and Gd-DTPA modified MSNs generating reversible MRI T_1 contrast change upon HIFU stimuli. (Not to scale)

We synthesized a panel of Pluronic-Gd-MSNs using Pluronic polymers with different molecular weights and PO/EO ratio as listed in Table S1. Since it is preferred to have hydrophobic terminals of Pluronic polymers conjugated to MSN surface, three reverse Pluronic polymers, 25R2, 17R4, and 31R1, with two hydrophobic blocks on both terminals were chosen. Pluronic P123 was also chosen as a comparison to the reverse Pluronic polymers. Then we used dynamic light scattering (DLS), zeta-potential measurement and inductively coupled plasma-optical emission spectrometry (ICP-OES) to characterize the hydrodynamic diameters, surface charge and the amount of coupled Gd-DTPA on the MSNs respectively. As shown in **Figure 4.2 (a)** and **Figure S 4.3**, the nanoparticles in the panel remain intact after surface modification. As shown in Table S1, after Pluronic polymer modification, the hydrodynamic diameters increased from 131 nm to 200-300 nm. The zeta-potential became less positive after coupling negatively charged Gd-DTPA, whose weight percentage was 0.2-0.6%. After the Pluronic coupling, the zeta-potential became negative. The negative zeta-potential is common for Pluronic micelle,[37] and the excess Pluronic

silane that was hydrolyzed to silanol group may also contribute to the negative charge. The functionalized 25R2 polymer was also quantified by weight loss from thermogravimetric analysis (TGA) as shown in **Figure S 4.5**: the weight loss of Gd-DTPA modified MSNs was 14.9%, whereas after 25R2 coupling, the weight loss increased to 56.1%, which indicated that the weight percentage of coupled 25R2 polymer was 41.2%.

To evaluate the HIFU-stimulated changes in T_1 caused by Pluronic-Gd-MSNs (25R2-Gd-MSNs, P123-Gd-MSNs, 17R4-Gd-MSNs and 31R1-Gd-MSNs), a series of MRIgHIFU experiments were designed and conducted. We performed MRIgHIFU fast modulation experiments using a dynamic 3D stack-of-radial T_1W MRI protocol to monitor the rapid T_1W contrast change of the panel of Pluronic-Gd-MSNs under various HIFU sequences. The Pluronic-Gd-MSNs were dispersed in Mili-Q water and mixed with a tissue-mimicking gel (methyl cellulose, 2 wt%). An agarose phantom (3.5 wt%) with cylindrical wells was constructed to hold the samples. The control was Magnevist (Mgv; FDA-approved commercially available formulation of gadopentetate dimeglumine [Bayer]) with the same amount of Gd-DTPA as the Pluronic-Gd-MSN samples. Various HIFU modulation sequences, power and duration were tested as shown in Table S2. Spectral signal processing was then performed to reconstruct MEM using a MATLAB (MathWorks, Natick, MA) script.[19] To quantify the image contrast enhancement, contrast difference % (CD%) were calculated using the following **Equation (4-1)**.

$$\mathbf{CD\%} = \frac{|\text{Intensity in region of interest-Intensity in reference area}|}{\text{Intensity in reference area}} \times 100\% \quad \text{Equation 4-1}$$

The HIFU focal point location in the sample area was chosen to be the region of interest (ROI) and the reference area corresponded to the agarose phantom area. Examples of these regions are depicted in **Figure 4.3 (c)**.

The CD% of MEM and T_1W images were calculated for each trial, and the results are listed in Table S2. We did not observe enhancement from 31R1-Gd-MSNs or 17R4-Gd-MSNs, thus the results are not listed here. A high degree of enhancement at the HIFU focal point on the MEM, as characterized by a high CD%, is preferred, as well as high enhancement fold compared to T_1W images and Mgv controls. The enhancement fold compared to T_1W images is the ratio of CD% of MEM over that of T_1W images of the same trial, which represents the enhancement achieved from the spotlight MRI technique. The enhancement fold compare to Mgv control is the ratio of CD% of MSN sample's MEM over that of Mgv under the same HIFU modulation sequence. We tested several HIFU amplitudes (70% and 50% of the maximum), cycle number (20 and 40 cycles), and modulation frequencies (0.25 and 0.5 Hz) settings, and the enhancement results are listed in Table S2. From the results in Table S2, we can observe that both 25R2-Gd-MSNs and P123-Gd-MSNs show strong contrast enhancement. We chose the HIFU sequence with 0.25 Hz modulation frequency and 20 cycles and 80 s duration for further comparison as shown in Table 1. At both lower amplitude (50%) and higher amplitude (70%), 25R2-Gd-MSNs showed higher CD% and higher enhancement to Mgv control compared to P123-Gd-MSNs. For 25R2-Gd-MSNs, the enhancement at 50% amplitude is higher than that at 70% amplitude, and 50% amplitude is considered safer for future biomedical applications. Therefore, we chose to conduct further analysis on 25R2-Gd-MSNs results modulated by HIFU sequence at 50% amplitude (bold in **Table 4.1**).

Table 4.1 Contrast Difference % (CD%) and enhancement fold of 25R2-Gd-MSNs and P123-Gd-MSNs tested under different HIFU power levels at 0.25 Hz modulation frequency with 20 cycles and 80 s duration.

Nanoparticles	HIFU amplitude and power	CD%	Enhancement fold vs. T_1W image	Enhancement fold vs. Mgv control
25R2-Gd-MSNs	70% (40 W)	641%	302.2	3.6
25R2-Gd-MSNs	**50% (20 W)**	**1332%**	**254.7**	**92.5**
P123-Gd-MSNs	70% (40 W)	291%	40.8	1.6
P123-Gd-MSNs	50% (20 W)	661%	387.5	45.9

The spotlight MRI spectral signal processing steps and results using data from 25R2-Gd-MSNs stimulated by 20 cycles of 0.25 Hz HIFU at 50% amplitude (20 W) are shown in **Figure 4.3**. **Figure 4.3 (a)** shows the changes of T_1W intensity (black), temperature (red) and HIFU modulation frequency (blue) in the time domain. From the zoomed-in view, we observe that when HIFU is turned on, both temperature and T_1W intensity increase; when HIFU is turned off, both temperature and T_1W intensity decrease. These changes are repetitive and reversible throughout the HIFU modulation sequence, which is 2 s on and 2 s off, with 20 cycles in total. For spectral analysis, we perform temporal Fourier transform on T_1W intensity change over time at a specific spatial location (pixel or region), as shown in (b). The signal peak of 0.25 Hz in the frequency domain spectrum matches the HIFU modulation frequency. To reconstruct MEM, the intensity of the 0.25 Hz peak at each pixel location is used to create a map throughout the entire field of view as shown in (c), and there is significantly increased intensity at the HIFU focal point because at this point the 0.25 Hz spectral component is at its maximum amplitude. For the ease of visualization, the MEM is displayed using a color scale. To conduct further analysis and evaluation of both image contrast and image quality with different levels of background noise, the contrast-to-noise ratio (CNR) is calculated using the **Equation (4-2)** and adopted in the following analysis.

$$\mathbf{CNR} = \frac{|\text{Intensity in region of interest} - \text{Intensity in reference area}|}{\text{Background noise standard deviation}} \quad \text{Equation 4-2}$$

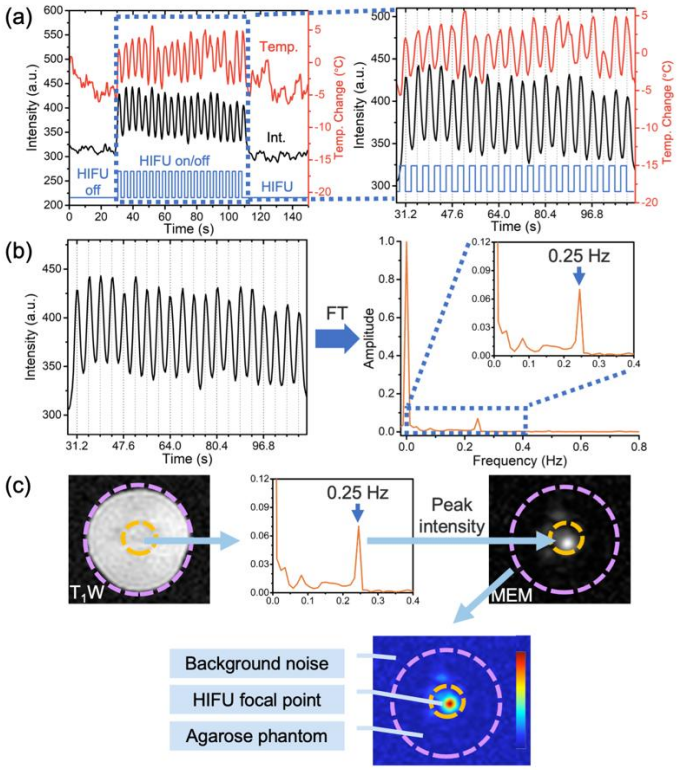

Figure 4.3 Spotlight MRI spectral signal processing steps and results using dynamic MR images reconstructed with optimized Tres and Tf from 20 cycles. (a) Plots of T_1W signal intensity and temperature change over time and zoomed-in view of the HIFU modulation time period; (b) Perform temporal Fourier transform (FT) on T_1W signal intensity vs time to generate Fourier transform spectrum; (c) Reconstruct MEM using the peak intensity of the spectral component at the HIFU modulation frequency for each pixel location (MEM displayed in color scale).

MRI reconstruction and processing to maximize contrast enhancement

Temporal resolution and footprint for dynamic MRI reconstruction

Appropriate choices of Tres and Tf for dynamic 3D stack-of-radial MRI reconstruction (**Figure 4.1**) are essential to obtain MEMs with high levels of enhancement and fidelity. We

performed retrospective data analysis and reconstructed MEMs using an experimental dataset from 25R2-Gd-MSNs stimulated with periodic HIFU of 0.25 Hz (2 sec on and 2 sec off) and 20 cycles. In order to choose the best performing combination of Tres and Tf, we investigated a parameter matrix shown in **Figure 4.4 (a)**. In each trial, we reconstructed the MEMs and the baseline T_1W images and used the same set of ROI for the intensity measurements. In **Figure 4.4 (a)**, each data point represents the result from one set of Tres and Tf. In **Figure 4.4 (b) – (d)**, The diameter of each data point is proportional to the numerical value, and each data point is color coded according to the numerical value (green color refers to favorable outcomes).

To verify the spectral data fidelity for calculating the MEMs, we examined the main peak frequencies (MPFs) on the temporal Fourier transform spectrum from dynamic 3D stack-of-radial MRI as shown in **Figure 4.4 (b)**. Since the HIFU modulation frequency was 0.25 Hz, the theoretical value of the MPF is 0.25 Hz. The MPFs that are close to 0.25 Hz represent high accuracy in capturing the modulated signal, and in this case, we choose the threshold to be 0.24 Hz. The fidelity check shows the data set with Tres lower than 0.61 s and Tf lower than 6.73 s meet the spectral data fidelity requirement.

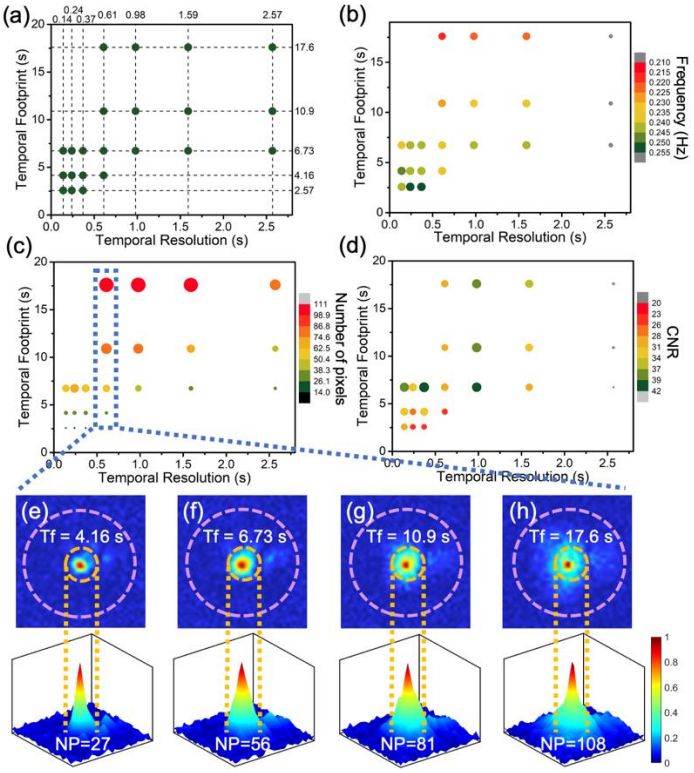

Figure 4.4 MEMs reconstructed using 20 stimulation cycles based on different parameter sets (green color represents better enhancement). (a) Temporal resolution (Tres) and temporal footprint (Tf) matrix; (b) Main peak frequencies (MPFs) on Fourier transform spectrum; (c) Spatial sharpness measure of MEMs; (d) CNR of MEMs reconstructed using various Tres and Tf; (e) – (h) MEMs reconstructed using Tres = 0.61 s and different Tf; as Tf increases, the number of pixels (NP) in the enhanced spatial region increases, indicating that the spatial sharpness decreases. The spatial sharpness is visualized by volcano plots under each MEM, where the narrower spatial enhancement patterns represent better spatial sharpness.

Next, we examined the quality of MEMs in terms of the spatial sharpness of the enhancement near the HIFU focal point as shown in **Figure 4.4 (c)**. In our controlled phantom experiments, the HIFU focal point was positioned in the sample well to stimulate the nanoparticles and achieve MRI contrast enhancement. Potential blurring in the MEM due to unsatisfactory choices of Tres

and Tf can degrade the precise delineation of enhancement at the HIFU focal point **Figure 4.4** (e) to (h) show increase in the blurring (decrease in spatial sharpness) when the Tf is increased. The red and orange areas on MEMs correspond to enhancement near the HIFU focal point, and the green and blue areas around it reflect blurring of the area of interest. The blurring effect is further visualized by volcano plots in **Figure 4.4** (e) to (h). We can observe that with shorter Tf, the enhanced area is sharp and well-defined in space, whereas the spatial sharpness with longer Tf is diminished. **Figure 4.4** (e) to (h) plot the number of pixels (NP) above 25% of maximum intensity, or full area at quarter of maximum (FAQM), with lower numerical values representing higher spatial sharpness. The observation based on spatial sharpness suggests that the data reconstructed with a Tf equal or lower than 4.16 s can achieve high spatial fidelity of MEMs. Another example of images reconstructed from long or short Tf is shown in **Figure S 4.2**. Long Tf leads to image blurring during motion or dynamic changes, while short Tf leads to sharper image features but more undersampling artifacts (radial streaking).

To evaluate the enhancement comprehensively, we calculated the CNR of MEM reconstructed from each set of Tres and Tf. As shown in **Figure 4.4 (d)**, the CNR of MEM reconstructed with Tres equal or shorter than 1.59 s and Tf equal or longer than 4.16 s achieved high CNR.

For comparison, we show the results with short and long Tres and Tf in **Figure 4.5** to interpret the outcome of choosing inappropriate sets of parameters. **Figure 4.5** (a) and (b) show the results with Tres = 0.14 s, Tf = 2.57 s, which are the shortest Tres and footprint we can achieve with the current dynamic MRI acquisition settings. In **Figure 4.5 (a)** we observe that both temperature and T_1W intensity signals are well defined and correlated, which lead to the sharp spectral peak on **Figure 4.5 (b)**. However, the fidelity of data is lower compared to that in the

optimized parameter set (Tres = 0.37 s, Tf = 4.16 s): the temperature plot shows more noise (less data is included to reconstruct each image due to the short Tf), and range of signal fluctuation is two times higher, which does not match the results from other temperature measurements. **Figure 4.5** (c) and (d) show results with the longest Tres and Tf we have tried: Tres = 2.57 s, Tf = 17.6 s. From **Figure 4.5 (c)** we can observe that the signal modulation of neither temperature nor intensity is reliable, and the peak frequency of **Figure 4.5 (d)** does not match the actual HIFU modulation frequency. Both examples highlight the importance of choosing proper Tres and Tf to balance the performance objectives and preserve temporal (spectral) and spatial signal fidelity.

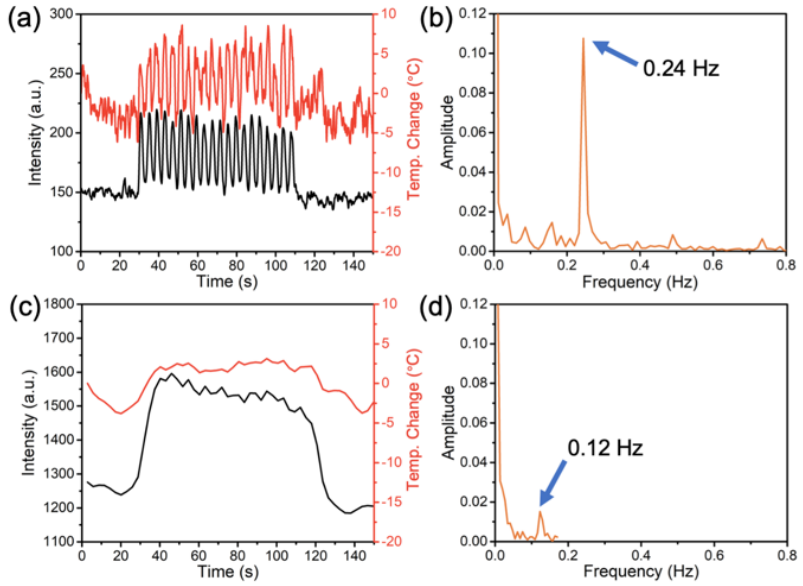

Figure 4.5 Examples of reconstruction results using short or long Tres and Tf: (a) T_1-weighted signal intensity and temperature plots over time and (b) Temporal Fourier transform spectrum reconstructed using Tres = 0.14 s, Tf = 2.57 s; (c) Intensity and temperature plots and (d) Temporal Fourier transform spectrum reconstructed using Tres = 2.57 s, Tf = 17.6 s.

Cycle number for calculating MEM

We also investigated the performance trade-offs for the number of HIFU on-off stimulation cycles and the corresponding cycles of T_1-weighted intensity changes over time included for

dynamic MRI reconstruction and calculation of MEMs. Fewer cycles would lead to shorter overall data acquisition time at a constant modulation frequency, which is desired in practice. However, fewer cycles would also result in lower spectral data quality (reduced spectral resolution after temporal Fourier transform). Therefore, we studied the tradeoff between the number of cycles (data acquisition time) and performance metrics by comparing MEMs reconstructed using 10 or 20 stimulation cycles. In **Figure 4.6 (a)**, we can observe that the spectral data fidelity using 10 cycles is lower than the results using 20 cycles: only 3 sets of results achieved accurate MPF (above 0.24 Hz). The spatial sharpness of MEMs shown in **Figure 4.6 (b)** has the same trend with the 20-cycle results but the NP (or FAQM) is higher, indicating lower spatial sharpness. Similarly, the CNR shown in **Figure 4.6 (c)** has the same trend with 20-cycle results. In order to summarize the impact of cycle number on CNR, we plot the ratio between CNR of 20 cycles and CNR of 10 cycles in **Figure 4.6 (d)**. The higher numerical value from Tres = 0.37 s suggests this Tres value can maximize the advantage of adjusting the cycle number.

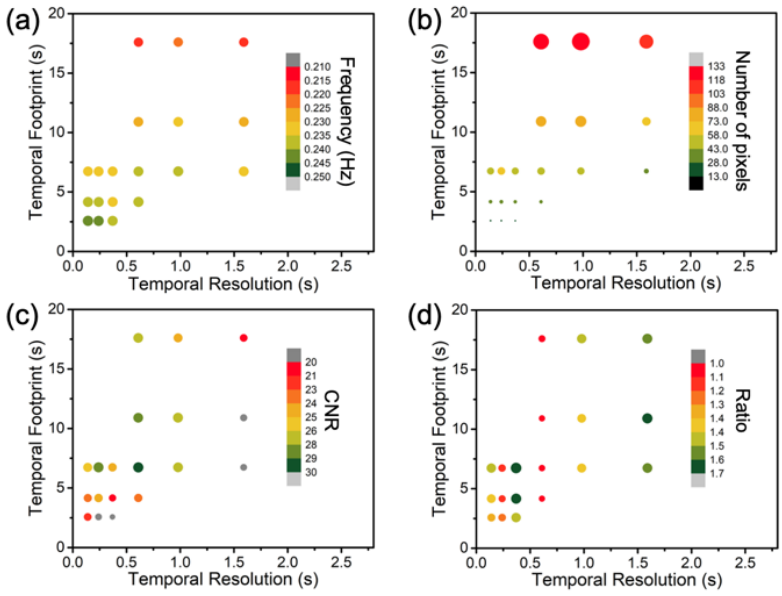

Figure 4.6 Characterization of MEMs reconstructed using 10 stimulation cycles. (a) Main peak frequencies (MPFs); (b) Spatial peak sharpness of MEMs; (c) CNR reconstructed using various

Tres and Tf; (d) Ratio between CNR of 20 cycles and CNR of 10 cycles. Tres = 0.37 s and Tf = 4.16 s are chosen to be the best parameter set for further analysis.

Noise analysis

In order to study the image and MEM reconstruction quality with various background noise levels, we added artificial noise to the raw 3D stack-of-radial MRI k-space data to simulate the noise generation in the actual MRI experiment, and analyzed the performance in terms of CNR in MEMs. For these experiments, we used an MRI noise model to simulate different amounts of noise in the data as shown in **Figure 4.7 (a)**. Zero-mean white Gaussian noise[38,39] was separately generated and superimposed to the real and imaginary components of each MRI k-space signal (i.e., radial readout) in each channel of the array coil in every single echo. The added Gaussian noise had a standard deviation that was specified to be a certain percentage (η) of the original signal strength at the center of k-space of the first echo in each readout. The noisy k-space signals were sent to the same reconstruction pipeline to obtain the dynamic MR images and calculate the MEMs. Ten instances were generated for each noise level in a Monte Carlo simulation.

The results and an example of the noise analysis are shown in **Figure 4.7** and **Figure S 4.6**. As shown in **Figure 4.7 (b)**, the CNR of MEM decreases as the added noise level increases. As the CNR of T_1W images without the spotlight MRI spectral signal processing steps is already low, the addition of noise does not cause a significant change. In **Figure S 4.6 (a)**, the intensity modulation is poorly defined, and the temperature change is highly dominated by noise. Due to the poor correlation, the spectrum in **Figure S 4.6 (b)** does not shown any notable peak at 0.25 Hz, but we can still use our knowledge of the HIFU modulation frequency to extract the appropriate spectral signal component to calculate the MEM. As shown on the T_1W images and MEM in **Figure S 4.6** (c) and (d), the added noise decreased the visibility of contrast enhancement at the

HIFU focal point and agarose phantom, but the HIFU focal point still shows contrast enhancement on MEM.

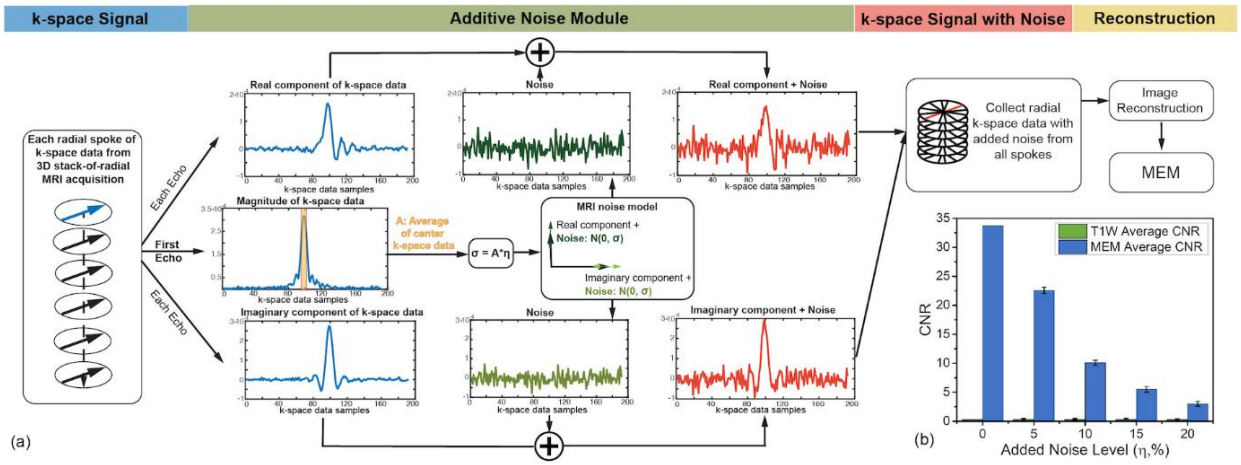

Figure 4.7 Noise analysis for spotlight MRI: (a) Example of the k-space additive noise generation using an MRI noise model. Zero-mean additive white Gaussian noise, characterized by a normal distribution (N) with zero mean and standard deviation of A*η, was generated and added to the real and imaginary components of the k-space data of every MRI radial readout spoke. σ: standard deviation; η: noise level; A: average center k-space data in the first echo of the MRI acquisition. (b) Plots of the mean and standard deviation (black bars) of CNR for T_1W and MEM across 10 instances at different added noise levels (η = 5%, 10%, 15%, 20%).

Spotlight MRI enhancement results with chosen parameters

After careful consideration of the image processing method and parameters, we found that Tres of 0.37 s and Tf of 4.16 s, as well as 20 cycles, can achieve the highest degree of enhancement for the current acquired dynamic MRI data. Thus, we used this parameter set to process the samples and controls to characterize the enhancements from our spotlight MRI technique. For the MEM with MSNs and HIFU shown in **Figure 4.8 (b)**, the CNR reaches 33.73, which is enhanced 116-fold compared to CNR of the conventional T_1W image shown in **Figure 4.8 (a)**. The MEM and T_1W can be overlaid as shown in **Figure 4.8 (c)** to show both the sample background from T_1W

and the spotlighted HIFU focal point from MEM. If we use the same MSN sample but do not apply HIFU modulation, the MEM does not show any enhancement and the CNR is 0.01. These results demonstrate that with MSNs and data processing, HIFU modulation can bring an enhancement of 3373-fold.

We also performed control experiments with Mgv. The Mgv control sample contains the same amount of Gd-DTPA as the MSN samples, and is dispersed in the same methyl cellulose phantom. Using the same HIFU sequence and image reconstruction and processing, the CNR of the Mgv MEM shown in **Figure 4.8 (e)** is 0.34, although the CNR of Mgv T_1W is higher than the CNR of MSN T_1W. Compared to Mgv, the MSNs achieved 99-fold higher enhancement on MEM, which indicates the amplified T_1W intensity changes enabled by responsive nanoparticles contribute significantly to the contrast enhancement.

We are aware that the parameter set we identified in this study may not be universal for all experimental conditions. The parameter choice depends on the HIFU modulation frequency and inherent dynamic MR image quality. However, this study provides a method and framework that would guide future designs for *in vitro* and *in vivo* studies.

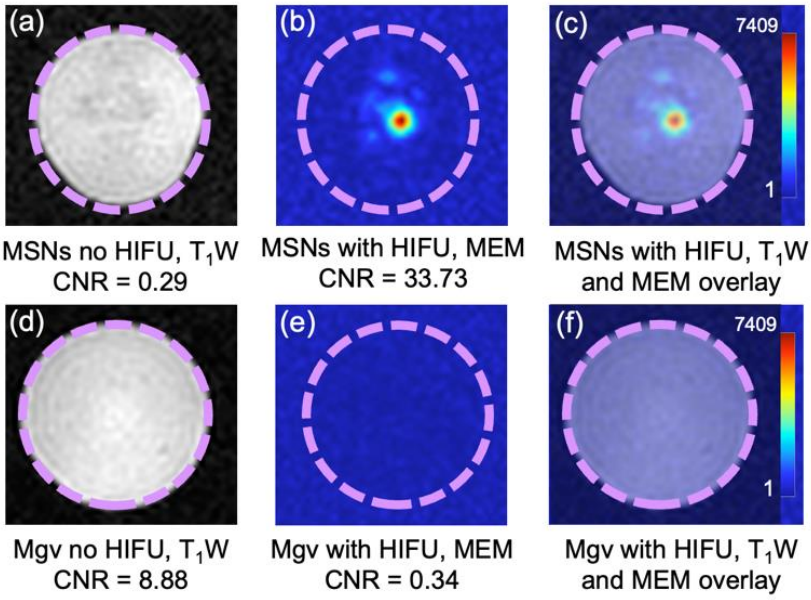

Figure 4.8 MEMs and T_1W of samples and controls. (a) T_1W of MSNs without HIFU; (b) MEM of MSNs with HIFU; (c) overlay of T_1W and MEM with MSNs and HIFU; (d) T_1W of Mgv without HIFU (e) MEM of Mgv with HIFU; (f) overlay of T_1W and MEM with Mgv and HIFU.

4.3 Conclusions

The HIFU-stimulated "spotlight" imaged by using MRI requires four integrated components: periodic HIFU stimulation, significant modulation of T_1 caused by HIFU, rapid MRI signal collection, and a spectral signal processing method. The T_1 modulation is caused by functionalized nanoparticles that reversibly expose and shield paramagnetic molecules in response to the mechanical and thermal effects of HIFU on a polymeric shell. We explored several types of polymer coatings based on their expected temperature and/or mechanical sensitivity to HIFU and chose the one causing the largest change in T_1 for detailed study. We then described in detail how to collect dynamic MR images and capture contrast changes rapidly enough to sample the oscillating signal. We simultaneously measured the changes in signal intensity and temperature of the sample as a function of time. We described in detail our method that involved a dynamic 3D

stack-of-radial T_1W MRI technique to monitor responses of the panel of polymer-coated nanoparticles to HIFU stimulation. Multiple HIFU sequences, powers and durations were tested and analyzed. We then evaluated MRI reconstruction and processing to maximize contrast enhancement. In order to study the image and MEM reconstruction quality, we added artificial noise to the data and analyzed the performance in terms of the contrast-to-noise ratio. Using the resulting parameter set, we showed that the MRI contrast enhancement in less than two minutes of acquisition time was two orders of magnitude greater than that of the Mgv control (contrast to noise ratio of 33.7 vs. 0.34) in the 1.5 mm^3 volume defining the HIFU focal point. This paper provides a multifaceted exposition and analysis of the materials, instrumentation, data acquisition and analysis techniques that are required to achieve spotlight MRI, and will advance the adaptation of the technique to potential biomedical applications.

4.4 Experimental Section

Chemicals

Tetraethylorthosilicate (TEOS; 99%, Aldrich), cetyltrimethylammonium bromide (CTAB; 98%, Aldrich), sodium hydroxide (99%, Fisher Scientific), absolute ethanol (EtOH; Aldrich). 3-aminopropyl triethoxysilane (APTES; 99%, Aldrich), Pluronic® 25R2 (BASF), Poly(propylene glycol)-block-poly(ethylene glycol)-block-poly(propylene glycol) (Pluronic® 17R4, M_n 2,700, Aldrich), Poly(propylene glycol)-block-poly(ethylene glycol)-block-poly(propylene glycol) (Pluronic® 31R1, M_n 3,300, Aldrich), Poly(ethylene glycol)-block-poly(propylene glycol)-block-poly(ethylene glycol) (Pluronic® P123, M_n 5,800, Aldrich) 3-(Triethoxysilyl)propyl isocyanate (95%, Aldrich), EDC•HCl (99%, Covachem), sulfo-NHS (99%, Covachem), diethylenetriaminepentaacetic acid gadolinium(III) dihydrogen salt hydrate (Gd-DTPA; 97%, Aldrich), nitric acid (TraceMetal grade, Fisher), methyl cellulose (4000 cP, Sigma), agarose

BP160-100 (Molecular Biology Grade, Fisher) were used as received. Anhydrous toluene was obtained by distillation from CaH_2 under dry nitrogen.

Synthesis of Gd-DTPA and Pluronic modified MSNs (Pluronic-Gd-MSNs)

a. Synthesis of mesoporous silica nanoparticles (MSNs)

0.25 g CTAB and 875 μL of sodium hydroxide solution (2 M) were dissolved in 120 mL of water under stirring. The solution was heated at 80 °C for 30 minutes, followed by the addition of 1.2 mL of TEOS and 0.79 mL ethyl acetate under vigorous stirring. Stirring was continued for 2 h at 80 °C, and then the solution was allowed to cool to room temperature. The nanoparticles were collected by centrifugation (15 min at 7830 rpm), washed 3x with ethanol (3x30 mL) and dispersed in 20 mL ethanol for further use. Approximately 200 mg of MSNs was obtained in each batch.

b. Amine modification on MSN surface

Around 200 mg unfunctionalized MSNs was washed 3x with toluene (3x30 mL), and redispersed in 30 mL of dry toluene stirring in a flame-dried 50 mL round bottom flask under nitrogen. Then 60 μL (3-aminopropyl)triethoxysilane was added drop by drop and resulting mixture was refluxed in 110 °C oil bath under nitrogen overnight. The amine-modified MSNs was collected by centrifugation (10 min at 7830 rpm) and washed 3x with ethanol (3x 30 mL). Product was redispersed in 20 mL ethanol for further use.

c. Extraction of APTES-functionalized MSNs (NH_2-MSNs)

APTES-functionalized MSNs dispersed in toluene were washed 2x with ethanol (2x30 mL). To extract the organic template from the pores, the nanoparticles were dispersed in 80 mL of an acidic ethanolic solution (EtOH:HCl(conc.) = 90/10 (v/v)), refluxed for 1 h, collected by centrifugation (10 min at 7830 rpm), and repeated above procedure one more time. The product was washed 2x with ethanol (2x 30 mL) and stored in ethanol.

d. Gd-DTPA modification of NH_2-MSNs

NH_2-MSN dispersed in ethanol was washed 3x with DI water (3x 30 mL), then dispersed in HEPES buffer (pH=7.4) for future use. 1.2 mL of Gd-DTPA water solution (0.10 g/mL, pH=6.7) was mixed with 4.8 mL of MES buffer (100 mM, pH = 6.0), 17.2 mg of EDC•HCl and 19 mg of sulfo-NHS, and the mixture was stirred for 20 min. 0.3, 0.6, 2.1, 3 mL of mixture were added to 5 mL of HEPES buffer with 60 mg NH_2-MSN dispersed, and stirred in room temperature for 24 h. Gd-DTPA modified MSNs (Gd-MSNs) products were washed 3x with DI water (3x30 mL).

e. Pluronic conjugation to Gd-MSNs

Dissolve 3 g Pluronic polymer in 30 mL of dry toluene stirring in a flame-dried 50 mL round bottom flask under nitrogen. Then 200 μL 3-(Triethoxysilyl)propyl isocyanate was added drop by drop and resulting mixture was refluxed in 110 °C oil bath under nitrogen overnight. Cool down to room temperature for further use. 50 mg Gd-MSNs was washed 3x with ethanol (3x30 mL) followed by 3x with dry toluene (3x 30 mL), then added into the fresh Pluronic and toluene mixture that was reacted overnight. The resulting mixture was refluxed in 110 °C oil bath under nitrogen overnight. The nanoparticles were collected by centrifugation (15 min at 7830 rpm), washed 3x with ethanol (3x 30 mL with 30 min sonication to remove the toluene) followed by 3x with DI water (3x30 mL). Dispersed in 10 mL DI water for further use.

Tissue mimicking gel and MRI-guided HIFU sample preparation

1 g methyl cellulose was slowly added to 15 mL boiled water and stirred for 3 min. Then 25 mL condensed milk was added followed by 10 mL cold water. The mixture was stored in a refrigerator overnight to eliminate air bubbles. 3 mg Pluronic-Gd-MSNs were dispersed in 0.5 mL water and then mixed with 1 mL gel/milk mixture, resulting in a 2 mg/mL Pluronic-Gd-MSNs

gel/milk mixture. The Magnevist (Mgv) control was made in a similar manner. Mgv was first diluted to 0.5 mL water and then mixed with 1 mL gel/milk mixture.

Agarose phantom

17.5 g agarose was slowly added to hot water with stirring. Then the solution was heated up to boiling, and then poured into a sample holder model. After agarose was solidified under room temperature, it was stored in a refrigerator for further use.

Characterization

Transmission electron microscopy (TEM)

TEM images were recorded on a Tecnai T12 Quick CryoEM at an accelerating voltage of 120 kV. A suspension (8 μL) of nanoparticles in ethanol was dropped on a 200 mesh carbon coated copper grid and the solvent was allowed to evaporate at room temperature.

Zeta-potential analysis and dynamic light scattering (DLS)

Zeta-potential analysis and DLS were carried out on a ZetaSizer Nano (Malvern Instruments Ltd., Worcestershire, U.K.) in DI water.

Thermogravimetric analysis (TGA)

TGA was performed using a Perkin-Elmer Pyris Diamond TG/DTA under air (200 mL/min). Approximately 5-10 mg of sample was loaded into aluminum pans. The sample was held at 100 °C for 30 minutes, and then the data were recorded during a temperature scan from 100 to 600 °C at a scan rate of 10 °C/min and an isothermal process of 600 °C for 80 min. The plotted values are normalized to the weight at 100 °C. An empty aluminum pan was used as a reference.

Quantification of Gd-DTPA by inductively coupled plasma atomic emission spectroscopy (ICP-OES)

ICP-OES measurements were made using ICPE-9000 Shimadzu. 0.1 mL of sodium hydroxide solution (2 M) was added to approximately 0.5-1 mg sample (Gd-MSNs or Pluronic-Gd-MSNs) dispersed in 0.05 mL of Milli-Q water, and the mixture was sonicated for 1 h. Then 0.05 mL of nitric acid was added, and the mixture was sonicated for 1h. The solution was then diluted to 10 mL with 2% nitric acid for measurement.

MRI-guided HIFU Experiments

All MRI-guided HIFU experiments were conducted using a research-dedicated HIFU system (Image Guided Therapy, Bordeaux, France) integrated with a whole-body 3 T MRI scanner (MAGNETOM Prisma, Siemens Healthineers, Erlangen, Germany). The HIFU system had an 8-element annular transducer array with a diameter of 25 mm, frequency of 2.5 MHz, a focal point of $0.7\times0.7\times3mm^3$ in size, and a peak electrical power output of 80 W. In this paper, the HIFU power was 20 W, with a 2-second on, 2-second off pattern, repeated for 20 times.

T_1-weighted gradient-echo images were acquired with both transversal (Field of view [FOV]=$213\times107\times48mm^3$, matrix size=192×96×24, flip angle=15°, TE=2.15ms, TR=4.6ms) and coronal (FOV=$180\times90\times72mm^3$, matrix size=192×96×36, flip angle=15°, TE=2.15ms, TR=4.6ms) orientations to locate the natural focal point of the HIFU beam, which was used throughout the experiment without any electronic or mechanical steering.

A T_1-weighted 3D golden-angle-ordered multiple-echo gradient-echo stack-of-radial sequence was used to simultaneously measure temperature change and T_1-weighted signal change with the following parameters: FOV=$109\times109\times18mm^3$, matrix size=96×96×6, flip angle=6°, 4 echoes with bipolar readout (TE=1.29ms, 2.5ms, 3.71ms and 4.92ms), and TR=7.79ms.[19,30,31] The

fourth slice from anterior was manually positioned such that it was centered with the natural HIFU focal point along the anterior-posterior dimension. A total of 3200 radial views were sampled continuously for 2.5 minutes, with the acquisition starting 30s prior to turning on HIFU to establish temperature baseline and continuing for an additional 1 minute after the conclusion of HIFU to observe the return to baseline. During image reconstruction, a k-space weighted image contrast (KWIC) filter[33,40] was applied to the raw data to produce 389 dynamic complex images with a Tres of 0.37 s and Tf of 4.16 s per 3D volume. Complex images from all channels were combined using a method proposed in a previous paper[41] with a modified Roemer's equation[42], after which the magnitude images of all echoes were combined using sum-of-squares while the phase images of all echoes were combined to an effective TE of 10ms to improve temperature mapping SNR. The channel- and echo-combined phase images of any dynamic time point *t* were then used to calculate temperature change ΔT according to **Equation 4-3**:

$$\Delta T = \frac{(\Phi_t - \Phi_1)}{\alpha \cdot TE \cdot \gamma}, \text{ Equation 4-3}$$

with Φ_t being the phase images at time points *t*, α=-0.01ppm/°C the temperature coefficient of PRF, and γ=42.576mHz/T the gyromagnetic ratio of protons.

After the relative temperature changes of all time points were calculated, the voxel that demonstrated the highest peak temperature change was picked as the actual HIFU focal point. Its location was in the general vicinity of the coordinates of the theoretical HIFU focal point recorded from the software during the planning stage, suggesting normal functioning of the HIFU system during the experiments. Average temperature changes as well as average signal intensities of all dynamic time points were then calculated in a square region of interest (ROI) of 9 pixels in size centering on the actual HIFU focal point, on which Fourier analysis was then performed to produce modulation enhancement maps (MEMs).

4.5 Supporting Information

Supplementary Notes

Non-Cartesian Radial MRI for Rapid Dynamic Imaging

Conventional MRI acquires data line-by-line on a rectilinear grid in 2D or 3D Fourier space (i.e., k-space)[43,44], which is known as Cartesian sampling (**Figure S 4.1**). Data near the center of k-space[44] represent low spatial frequency content in image space and have a major role in determining the image contrast. Data in the periphery of k-space correspond to high spatial frequency information in image space and contribute to the fine spatial details. Once a sufficient set of k-space data samples are collected according to the Nyquist sampling criteria,[44] a spatial Fourier transform is performed to reconstruct the image. Cartesian sampling is widely used in MRI due to its robustness to system imperfections and ease of implementation, but acquiring a fully sampled dataset covering all regions of k-space using Cartesian sampling is slow and limits the ability for MRI to capture rapid dynamic processes. MRI reconstruction algorithms have been developed to use prior information (e.g., multiple receiver channels[45], sparsity constraints[46]) and produce images from undersampled Cartesian k-space datasets. However, the geometry of Cartesian k-space sampling leads to coherent aliasing artifacts during motion or dynamic processes and restricts the trade-off between spatial resolution (the physical size that a pixel in an image represents) and temporal resolution (the time interval or rate at which data or images are acquired, reconstructed, or displayed) - higher spatial resolution requires more time to sample k-space data for one image frame, which negatively affects the temporal resolution.

In contrast to Cartesian sampling, non-Cartesian methods such as radial sampling[32] provide more robustness to motion, unobtrusive undersampling artifacts, and greater flexibility in balancing spatial and temporal resolution during dynamic MR imaging. This is possible because

of the radial sampling geometry, where each radial spoke contains data points from the central and peripheral regions of k-space (**Figure S 4.1**). Even when an undersampled set of radial spokes is used to reconstruct an image frame, the radial sampling pattern usually has enough density in the center of k-space to capture the image contrast, while undersampling in the peripheral regions of k-space only leads to noise-like streaking artifacts in the image that do not obscure the object of interest.

MR Temperature Mapping

MRI has the unique capability to non-invasively map temperature changes. The most widely used method is based on the proton resonance frequency shift (PRF), which decreases linearly as temperature increases with a coefficient of α=-0.01ppm/°C in aqueous tissues and remains consistent over a wide temperature range relevant to thermal therapy.[34,35] Typically, PRF is measured by a gradient-echo-based sequence with fixed echo time (TE) and then subtracting baseline phase images φ_0 acquired before heating (i.e., baseline temperature) from phase images φ acquired at an elevated temperature during heating. The phase difference is converted into temperature change according to $\Delta T=(\varphi-\varphi_0)/(\alpha\gamma B_0 TE)$, with γ being the gyromagnetic ratio of protons and B_0 the main magnetic field strength.[35] The choice of TE is thus crucial to achieving accurate measurement and it has been shown its optimal value is equal to the T_2* relaxation time of the tissue in question.[47,48]

Supporting Tables

Table S 4.1 DLS, zeta-potential and ICP-OES characterization of panel of Pluronic-Gd-MSNs.

	Polymer M_n (g/mol)	EO block weight %	Hydrodynamic diameters (nm)	Zeta-potential (mV)	Gd-DTPA weight%
Amine-functionalized MSNs	-	-	124	22.82	-
Gd-DTPA modified MSNs	-	-	131	13.65	0.31%
25R2-Gd-MSNs	3600	20	245	-43.07	0.27%
17R4-Gd-MSNs	2700	40	335	-32.35	0.56%
31R1-Gd-MSNs	3300	10	267	-27.79	0.46%
P123-Gd-MSNs	5800	30	237	-32.15	0.22%

Table S 4.2 CD% and enhancement fold of 25R2-Gd-MSNs and P123-Gd-MSNs tested under different HIFU sequence, power and duration.

Nanoparticles	HIFU amplitude and power	HIFU cycles and duration	HIFU modulation frequency (Hz)	CD%	Enhancement fold compared to T_1W image	Enhancement fold compared to Mgv control
25R2-Gd-MSNs	70% (40W)	20, 80s	0.25	641%	302.2	3.6
	70% (40W)	40, 160s	0.25	976%	426.5	3.2
	70% (40W)	40, 80s	0.5	306%	133.8	0.5
	50% (20W)	20, 80s	0.25	1332%	254.7	92.5
	50% (20W)	40, 80s	0.5	793%	161.7	118.2
P123-Gd-MSNs	70% (40W)	20, 80s	0.25	291%	40.8	1.6
	70% (40W)	40, 160s	0.25	626%	2959.1	2.1
	70% (40W)	40, 80s	0.5	741%	3504.8	1.2

50% (20W)	20, 80s	0.25	661%	387.5	45.9
50% (20W)	40, 80s	0.5	481%	129.9	71.8

Supporting Figures

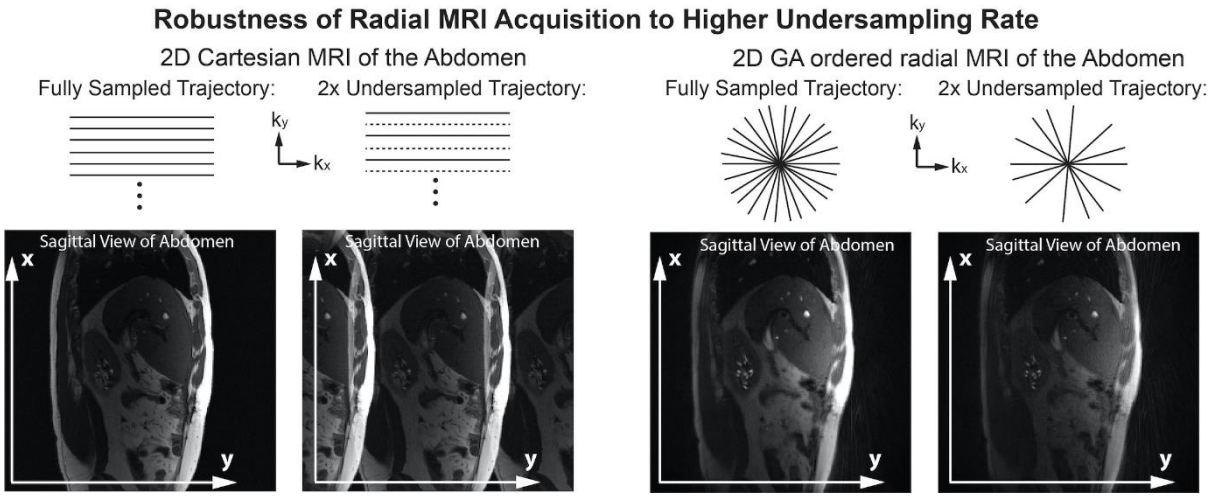

Figure S 4.1 Golden angle (GA) ordered radial MRI acquisition is more robust to undersampling artifacts than Cartesian sampling.

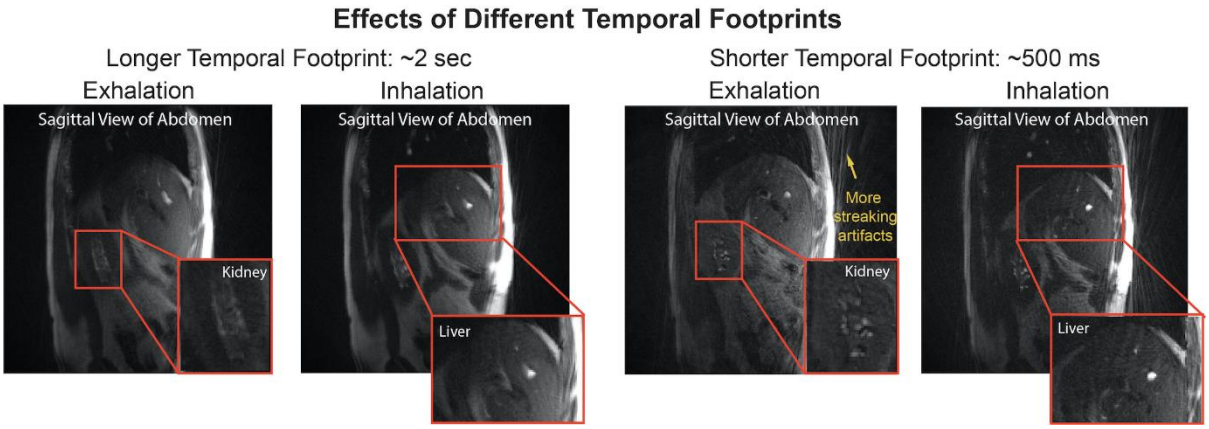

Figure S 4.2 Long temporal footprint (Tf) leads to image blurring during motion, while short Tf leads to sharper image features but more undersampling artifacts (radial streaking).

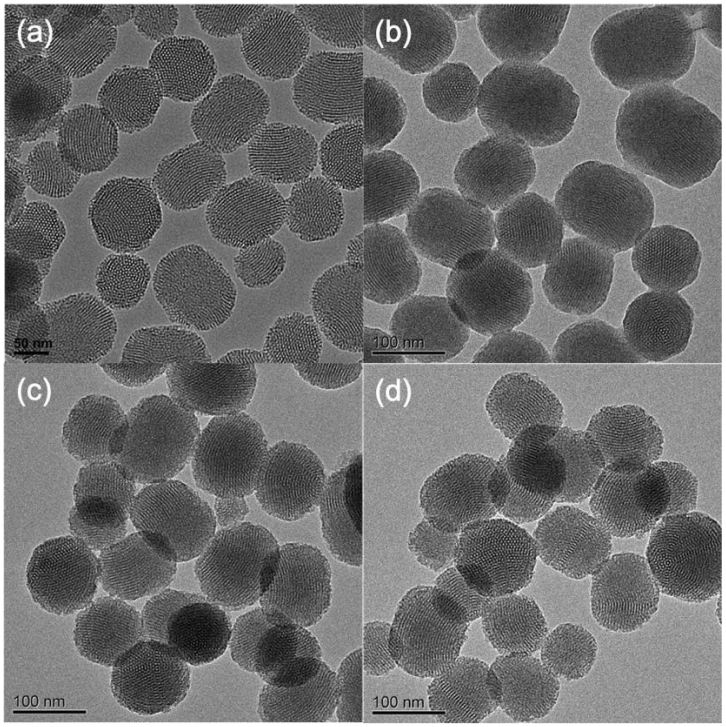

Figure S 4.3 TEM images of bare MSNs and various Pluronic-Gd-MSNs. (a) bare MSNs (b) P123-Gd-MSNs (c) 17R4-Gd-MSNs (d) 31R1-Gd-MSNs. The diameter of MSNs are all around 120 nm.

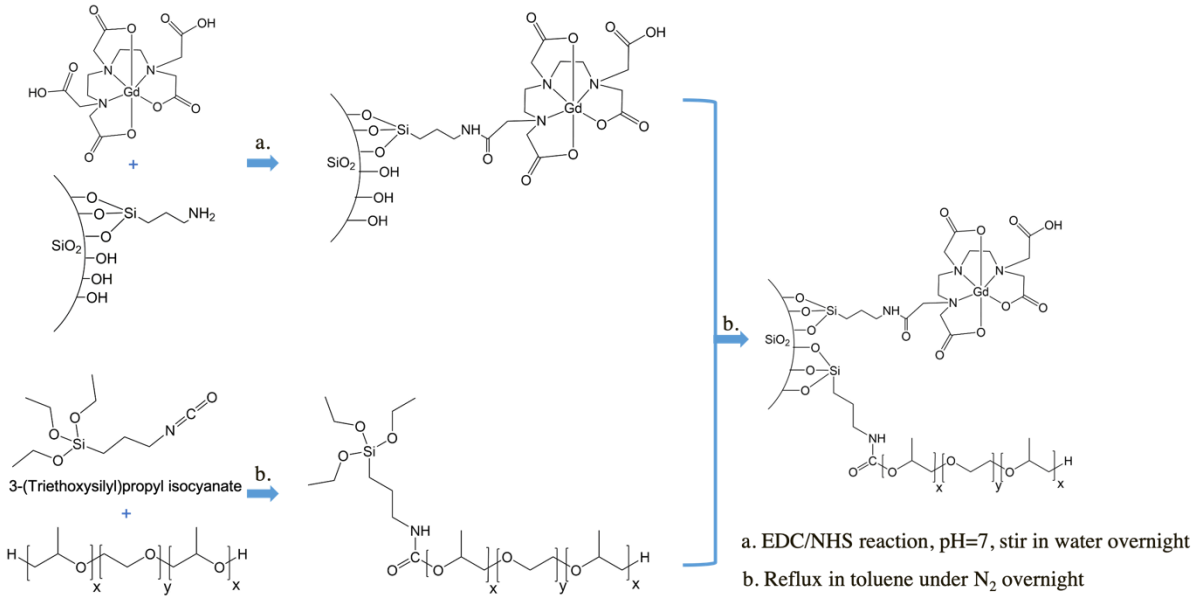

Figure S 4.4 MSN surface modification route.

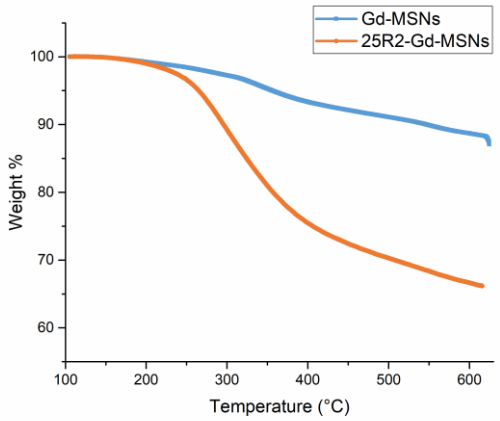

Figure S 4.5 TGA results of 25R2-Gd-MSNs.

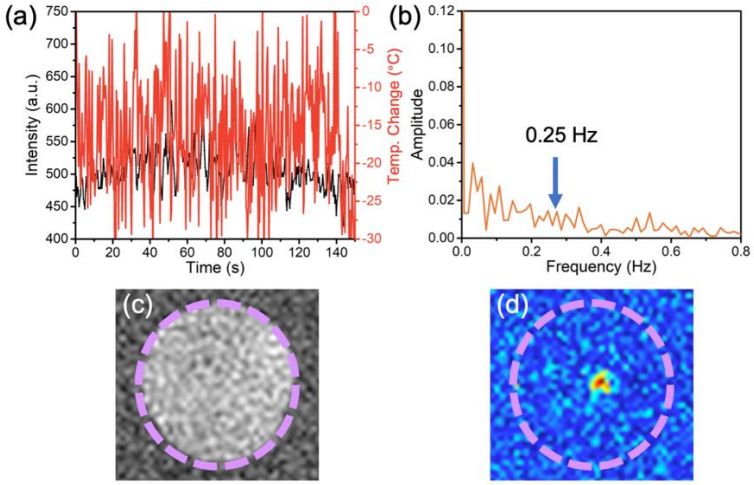

Figure S 4.6 Example of noise analysis: (a) plots of T_1-weighted intensity and temperature over time; (b) temporal Fourier transform spectrum; (c) T_1W image; (d) MEM calculated from the dynamic data with added noise level of standard deviation = 15% of original central k-space signal in each readout of each time frame. The proposed spotlight MRI technique achieves contrast enhancement at the HIFU focal point, even with increased levels of noise.

4.6 References

(1) Sung, H. H.; Jeong, B. C.; Seo, S. Il; Jeon, S. S.; Choi, H. Y.; Lee, H. M. Seven Years of Experience with High-Intensity Focused Ultrasound for Prostate Cancer: Advantages and Limitations. *Prostate* **2012**, *72*, 1399–1406.

(2) Merckel, L. G.; Knuttel, F. M.; Deckers, R.; van Dalen, T.; Schubert, G.; Peters, N. H. G. M.; Weits, T.; van Diest, P. J.; Mali, W. P. T. M.; Vaessen, P. H. H. B.; van Gorp, J. M. H. H.; Moonen, C. T. W.; Bartels, L. W.; van den Bosch, M. A. A. J. First Clinical Experience with a Dedicated MRI-Guided High-Intensity Focused Ultrasound System for Breast Cancer Ablation. *Eur. Radiol.* **2016**, *26*, 4037–4046.

(3) ter Haar, G.; Coussios, C. High Intensity Focused Ultrasound: Physical Principles and Devices. *Int. J. Hyperth.* **2007**, *23*, 89–104.

(4) Fruehauf, J. H.; Back, W.; Eiermann, A.; Lang, M. C.; Pessel, M.; Marlinghaus, E.; Melchert, F.; Volz-Köster, S.; Volz, J. High-Intensity Focused Ultrasound for the Targeted Destruction of Uterine Tissues: Experiences from a Pilot Study Using a Mobile HIFU Unit. *Arch. Gynecol. Obstet.* **2008**, *277*, 143–150.

(5) Chiara Zini, Elisabeth Hipp, Stephen Thomas, Alessandro Napoli, Carlo Catalano, A. O. Ultrasound- and MR-Guided Focused Ultrasound Surgery for Prostate Cancer. *World J. Radiol.* **2012**, *4*, 247.

(6) Malietzis, G.; Monzon, L.; Hand, J.; Wasan, H.; Leen, E.; Abel, M.; Muhammad, A.; Price, P.; Abel, P. High-Intensity Focused Ultrasound: Advances in Technology and Experimental Trials Support Enhanced Utility of Focused Ultrasound Surgery in Oncology. *Br. J. Radiol.* **2013**, *86*.

(7) Rieke, V.; Pauly, K. B. MR Thermometry. *J. Magn. Reson. Imaging* **2008**, *27*, 376–390.

(8) Khokhlova, V. A.; Fowlkes, J. B.; Roberts, W. W.; Schade, G. R.; Xu, Z.; Khokhlova, T. D.; Hall, T. L.; Maxwell, A. D.; Wang, Y.-N.; Cain, C. A. Histotripsy Methods in Mechanical Disintegration of Tissue: Towards Clinical Applications. *Int. J. Hyperth. Off. J. Eur. Soc. Hyperthermic Oncol. North Am. Hyperth. Gr.* **2015**, *31*, 145–162.

(9) Caravan, P.; Ellison, J. J.; Mcmurry, T. J.; Lauffer, R. B. Gadolinium (III) Chelates as MRI Contrast Agents : Structure , Dynamics , and Applications. **1999**, *99*, 2293−2352.

(10) Lee, H.; Lee, E.; Kim, D. K.; Jang, N. K.; Jeong, Y. Y.; Jon, S. Antibiofouling Polymer-Coated Superparamagnetic Iron Oxide Nanoparticles as Potential Magnetic Resonance Contrast Agents for *in Vivo* Cancer Imaging. *J. Am. Chem. Soc.* **2006**, *128*, 7383–7389.

(11) Scofield, J. H. Frequency-domain Description of a Lock-in Amplifier. *Am. J. Phys.* **1994**, *62*, 129–133.

(12) Kotler, S.; Akerman, N.; Glickman, Y.; Keselman, A.; Ozeri, R. Single-Ion Quantum Lock-in Amplifier. *Nature* **2011**, *473*, 61–65.

(13) Cheng, C. A.; Chen, W.; Zhang, L.; Wu, H. H.; Zink, J. I. A Responsive Mesoporous Silica Nanoparticle Platform for Magnetic Resonance Imaging-Guided High-Intensity Focused Ultrasound-Stimulated Cargo Delivery with Controllable Location, Time, and Dose. *J. Am. Chem. Soc.* **2019**, *141*, 17670–17684.

(14) Cheng, C.-A.; Chen, W.; Zhang, L.; Wu, H. H.; Zink, J. I. Magnetic Resonance Imaging of High-Intensity Focused Ultrasound-Stimulated Drug Release from a Self-Reporting Core@ Shell Nanoparticle Platform. *Chem. Commun.* **2020**, *56*, 10297–10300.

(15) Li, X.; Wang, Z.; Xia, H. Ultrasound Reversible Response Nanocarrier Based on Sodium Alginate Modified Mesoporous Silica Nanoparticles. *Front. Chem.* **2019**, *7*.

(16) Li, X.; Xie, C.; Xia, H.; Wang, Z. PH and Ultrasound Dual-Responsive Polydopamine-Coated Mesoporous Silica Nanoparticles for Controlled Drug Delivery. *Langmuir* **2018**, *34*, 9974–9981.

(17) Wang, X.; Qiao, L.; Yu, X.; Wang, X.; Jiang, L.; Wang, Q. Controllable Formation of Ternary Inorganic-Supramolecular-Polymeric Hydrogels by Amidation-Fueled Self-Assembly and Enzymatic Post-Cross-Linking for Ultrasound Theranostic. *ACS Biomater. Sci. Eng.* **2019**, *5*, 5888–5896.

(18) Zhang, K.; Xu, H.; Jia, X.; Chen, Y.; Ma, M.; Sun, L.; Chen, H. Ultrasound-Triggered Nitric Oxide Release Platform Based on Energy Transformation for Targeted Inhibition of Pancreatic Tumor. *ACS Nano* **2016**, *10*, 10816–10828.

(19) Deng, T.; Zhang, L.; Wu, H. H.; Zink, J. I. A Nanoparticle Enabled Focused Ultrasound-Stimulated Magnetic Resonance Imaging Spotlight. *Chem. Commun.* **2019**, *55*, 10261–10264.

(20) Oerlemans, C.; Bult, W.; Bos, M.; Storm, G.; Nijsen, J. F. W.; Hennink, W. E. Polymeric Micelles in Anticancer Therapy: Targeting, Imaging and Triggered Release. *Pharm. Res.* **2010**, *27*, 2569–2589.

(21) Tang, Z.; He, C.; Tian, H.; Ding, J.; Hsiao, B. S.; Chu, B.; Chen, X. Polymeric Nanostructured Materials for Biomedical Applications. *Prog. Polym. Sci.* **2016**, *60*, 86–128.

(22) Vijayan, V. M.; Muthu, J. Polymeric Nanocarriers for Cancer Theranostics. *Polym. Adv. Technol.* **2017**, *28*, 1572–1582.

(23) Bodratti, A. M.; Alexandridis, P. Formulation of Poloxamers for Drug Delivery. *J. Funct. Biomater.* **2018**, *9*.

(24) Bromberg, L.; Alakhov, V. Y.; Hatton, T. A. Self-Assembling Pluronic®-Modified Polycations in Gene Delivery. *Curr. Opin. Colloid Interface Sci.* **2006**, *11*, 217–223.

(25) Guiraud, S.; Alimi-Guez, D.; van Wittenberghe, L.; Scherman, D.; Kichler, A. The Reverse Block Copolymer Pluronic 25R2 Promotes DNA Transfection of Skeletal Muscle. *Macromol. Biosci.* **2011**, *11*, 590–594.

(26) Husseini, G. A.; Rapoport, N. Y.; Christensen, D. A.; Pruitt, J. D.; Pitt, W. G. Kinetics of Ultrasonic Release of Doxorubicin from Pluronic P105 Micelles. *Colloids Surfaces B Biointerfaces* **2002**, *24*, 253–264.

(27) Wu, P.; Jia, Y.; Qu, F.; Sun, Y.; Wang, P.; Zhang, K.; Xu, C.; Liu, Q.; Wang, X. Ultrasound-Responsive Polymeric Micelles for Sonoporation-Assisted Site-Specific Therapeutic Action. *ACS Appl. Mater. Interfaces* **2017**, *9*, 25706–25716.

(28) Munshi, N.; Rapoport, N.; Pitt, W. G. Ultrasonic Activated Drug Delivery from Pluronic P-105 Micelles. *Cancer Lett.* **1997**, *118*, 13–19.

(29) Manzano, M.; Vallet-Regí, M. Ultrasound Responsive Mesoporous Silica Nanoparticles for Biomedical Applications. *Chem. Commun.* **2019**, *55*, 2731–2740.

(30) Zhang, L.; Armstrong, T.; Li, X.; Wu, H. H. A Variable Flip Angle Golden-angle-ordered 3D Stack-of-radial MRI Technique for Simultaneous Proton Resonant Frequency Shift and T1-based Thermometry. *Magn. Reson. Med.* **2019**.

(31) Zhang, L.; Armstrong, T.; Wu, H. Dynamic PRF and T1-Based 3D Thermometry in the Liver Using a Variable Flip Angle Stack-of-Radial Technique.; ISMRM 28th Annual Meeting p. 102, 2020.

(32) Winkelmann, S.; Schaeffter, T.; Koehler, T.; Eggers, H.; Doessel, O. An Optimal Radial Profile Order Based on the Golden Ratio for Time-Resolved MRI. *IEEE Trans. Med. Imaging* **2006**, *26*, 68–76.

(33) Song, H. K.; Dougherty, L. Dynamic MRI with Projection Reconstruction and KWIC Processing for Simultaneous High Spatial and Temporal Resolution. *Magn. Reson. Med. An Off. J. Int. Soc. Magn. Reson. Med.* **2004**, *52*, 815–824.

(34) Poorter, J. De; Wagter, C. De; Deene, Y. De; Thomsen, C.; Ståhlberg, F.; Achten, E. Noninvasive MRI Thermometry with the Proton Resonance Frequency (PRF) Method: *In Vivo* Results in Human Muscle. *Magn. Reson. Med.* **1995**, *33*, 74–81.

(35) Ishihara, Y.; Calderon, A.; Watanabe, H.; Okamoto, K.; Suzuki, Y.; Kuroda, K.; Suzuki, Y. A Precise and Fast Temperature Mapping Using Water Proton Chemical Shift. *Magn. Reson. Med.* **1995**, *34*, 814–823.

(36) Ruehle, B.; Clemens, D. L.; Lee, B.-Y.; Horwitz, M. A.; Zink, J. I. A Pathogen-Specific Cargo Delivery Platform Based on Mesoporous Silica Nanoparticles. *J. Am. Chem. Soc.* **2017**, *139*, 6663–6668.

(37) Sezgin, Z.; Yüksel, N.; Baykara, T. Preparation and Characterization of Polymeric Micelles for Solubilization of Poorly Soluble Anticancer Drugs. *Eur. J. Pharm. Biopharm.* **2006**, *64*, 261–268.

(38) Gudbjartsson, H.; Patz, S. The Rician Distribution of Noisy MRI Data. *Magn. Reson. Med.* **1995**, *34*, 910–914.

(39) Macovski, A. Noise in MRI. *Magn. Reson. Med.* **1996**, *36*, 494–497.

(40) Song, H. K.; Dougherty, L. K-Space Weighted Image Contrast (KWIC) for Contrast Manipulation in Projection Reconstruction MRI. *Magn. Reson. Med. An Off. J. Int. Soc. Magn. Reson. Med.* **2000**, *44*, 825–832.

(41) Svedin, B. T.; Payne, A.; Jr, B. D. B.; Parker, D. L. Multiecho Pseudo-Golden Angle Stack of Stars Thermometry With High Spatial and Temporal Resolution Using k-Space Weighted Image Contrast. **2018**, *1419*, 1407–1419.

(42) Roemer, P. B.; Edelstein, W. A.; Hayes, C. E.; Souza, S. P.; Mueller, O. M. The NMR Phased Array. *Magn. Reson. Med.* **1990**, *16*, 192–225.

(43) Twieg, D. B. The K-trajectory Formulation of the NMR Imaging Process with Applications in Analysis and Synthesis of Imaging Methods. *Med. Phys.* **1983**, *10*, 610–621.

(44) Hennig, J. K-Space Sampling Strategies. *Eur. Radiol.* **1999**, *9*, 1020–1031.

(45) Larkman, D. J.; Nunes, R. G. Parallel Magnetic Resonance Imaging. *Phys. Med. Biol.* **2007**, *52*, R15.

(46) Lustig, M.; Donoho, D.; Pauly, J. M. Sparse MRI: The Application of Compressed Sensing for Rapid MR Imaging. *Magn. Reson. Med. An Off. J. Int. Soc. Magn. Reson. Med.* **2007**, *58*, 1182–1195.

(47) Cline, H. E.; Hynynen, K.; Schneider, E.; Hardy, C. J.; Maier, S. E.; Watkins, R. D.; Jolesz, F. A. Simultaneous Magnetic Resonance Phase and Magnitude Temperature Maps in Muscle. *Magn. Reson. Med.* **1996**, *35*, 309–315.

(48) Kuroda, K.; Mulkern, R. V; Oshio, K.; Panych, L. P.; Nakai, T.; Moriya, T.; Okuda, S.; Hynynen, K.; Joles, F. A. Temperature Mapping Using the Water Proton Chemical Shift: Self-referenced Method with Echo-planar Spectroscopic Imaging. *Magn. Reson. Med. An Off. J. Int. Soc. Magn. Reson. Med.* **2000**, *43*, 220–225.

Chapter 5. Tailored Thermo-Responsive Nanoparticle Spotlight to Enable Focused Ultrasound-Stimulated Magnetic Resonance Imaging Contrast Enhancement at Physiological Temperature

5.1 Introduction

Magnetic resonance imaging (MRI) guided high intensity focused ultrasound (HIFU) is a therapeutic tool and has been applied in the clinic for cancer treatment for decades.[1–3] With the focal point of 1.5 mm^3, HIFU can realize precise spatial and temporal control and perform tissue ablation under the guidance of MRI. An improved MRI contrast can expand the capability of MRI-guided HIFU (MRIgHIFU) to treat detailed tissue structure, such as a tumor margins or a metastatic tumors.[4–6] Mesoporous silica nanoparticles (MSNs) are biocompatible drug delivery platforms and have been applied in MRI contrast enhancement.[7–9] In our previous proof-of-concept work (see Chapter 3), a "Spotlight technique" was introduced that utilized MSNs functionalized with poly(*N*-isopropylacrylamide) (PNIPAm) and gadolinium-diethylenetriamine pentaacetic acid (Gd-DTPA). PNIPAm is a thermo-responsive polymer with a lower critical solution temperature (LCST) at 32 °C and Gd-DTPA is the effective component in the commercialized MRI contrast agent Magnevist©. With functionalized MSNs, the spotlight technique enhanced the MRI contrast almost 100-fold.[10] However, PNIPAm is not suited to be triggered by local temperature changes *in vivo*, as its LCST is below physiological temperature (37 °C). The PNIPAm functionalized MSNs require HIFU-induced temperature modulation around LCST to alternate water access to Gd-DTPA on MSN surface, so that it can only generate periodic MRI contrast change and enhance MRI contrast around 32 °C. If applied to humans, the temperature is always above the LCST of

PNIPAm, and the MRI contrast cannot be modulated. Therefore, a polymer with LCST higher than 37 °C is essential for the application of the spotlight technique. In addition, the LCST cannot be too high (usually no higher than 45 °C), or the hyperthermia will damage the healthy tissue.[11] So the ability to fine tune the LCST to be in the appropriate range is crucial.

A promising thermo-responsive polymer with a tunable LCST is poly(2-oxazoline) (POx). POxs are peptidomimetic polymers and can be synthesized via a controlled ring-opening polymerization.[12] The molecular structure of POx is similar to PNIPAm: they both have amides in the repeating units, while POx has amide in its backbones and PNIPAm has amide in the side-chain. Like PNIPAm, POx can transit from a hydrated soluble state (coil) to an aggregated insoluble state (globule) across LCST as shown in **Figure 5.1 (a)**. The LCST can be tuned by modifying the architectures of side-chains and/or copolymer composition.[13] The hydrophilicity difference of the side-chain has a large impact on the LCST. For example, homopolymers derived from the extremely hydrophilic 2-methyl-2-oxazoline (MeOx) display no observable LCST, while poly(2-butyl-2-oxazoline)s are insoluble in water at ambient conditions.[13] Between these extremes, erivatives of 2-ethyl-2-oxazoline (EtOx) exhibit LCSTs from 60 to 100 °C, and derivatives of (2-isopropyl-2-oxazoline) (iPrOx) exhibit LCSTs from 45 to 50 °C, depending on molar mass, concentration, and composition of (co)polymers.[12] In addition, the POx polymers can be end-capped with various functional groups, thus can be conjugated onto various substrates and surfaces. Therefore, we chose to pursue EtOx and iPrOx-containing polymers such that the LCST could be tailored by polymer structure and architecture.

In this work, we developed a nanoparticle functionalized with both POx with an LCST at 40 °C and Gd-DTPA. As shown in **Figure 5.1 (b)**, both POx and Gd-DTPA were coupled on the outer surface of MSNs. When applying periodic HIFU under the guidance of MRI, the nanoparticles

enabled reversible MRI T_1 contrast change: when HIFU was off, the local temperature was below LCST, and the POx was hydrophilic and allows water access to the Gd-DTPA; when HIFU was on and the local temperature rises above LCST, the POx became hydrophobic and eliminated water access to the Gd-DTPA, thus leading to a longer T_1 value and a lower intensity in a T_1-weighted (T_1W) image. When HIFU is off again, the local temperature drops below the LCST, the POx becomes hydrophilic again, allowing more water access to the Gd-DTPA, and reverse T_1 back to the starting point. Using the spectral analysis applied on the periodic T_1 modulation versus time, MRI contrast is enhanced on the reconstructed modulation enhancement map (MEM). The local thermal heating *via* HIFU could selectively trigger the reversible contrast change from nanoparticle at the physiologically relevant temperature.

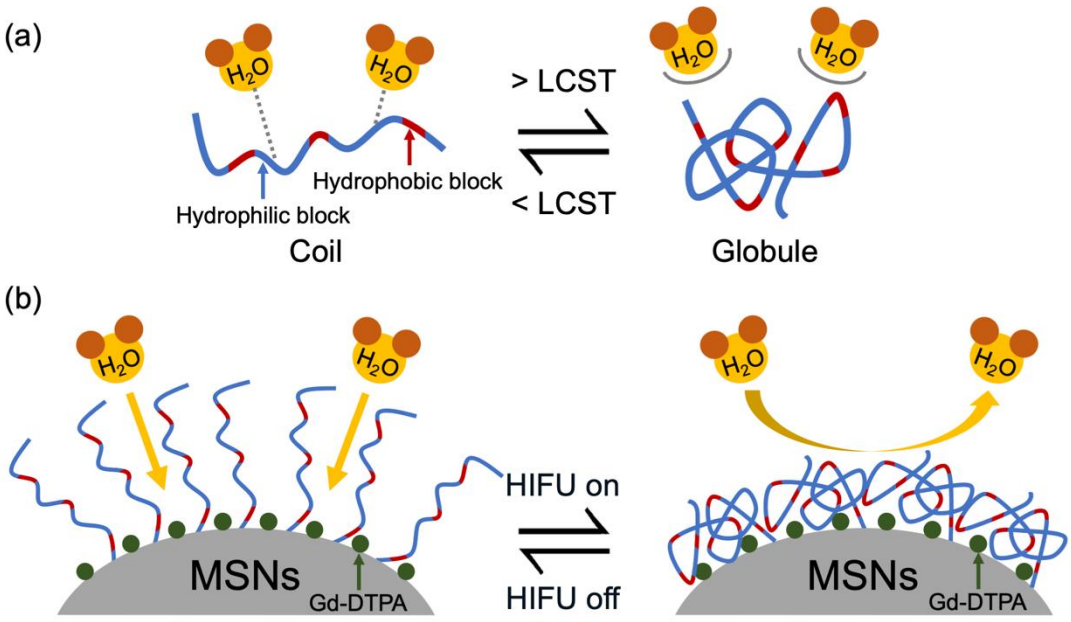

Figure 5.1 (a) POx polymer with transitions from a hydrated soluble state (coil) to an aggregated insoluble state (globule); (b) Mechanism of MSNs modified with POx and Gd-DTPA that causes reversible MRI contrast changes.

5.2 Results and Discussion

First, the POx with fine-tuned LCST was synthesized. The side-chains of POx can be easily modified, and chain lengths of aliphatic groups can be gradually extended in order to modify the LCST. One such polymer is poly(2-isopropyl-2-oxazoline (PiPrOx, **2**) as shown in **Figure 5.2 (a)**, a structural analogue of PNIPAm (**1**) with an LCST of around 45 – 50 °C.[14,15] Additionally, copolymer ratios of these monomers can be modified in order to vary the LCST. For instance, one can gradually increase the feed ratio of more hydrophobic monomers (*e.g.*, 2-butyl-2-oxazoline, BuOx) versus hydrophilic monomers (*e.g.*, iPrOx) to reduce the LCST as desired. Rainer Jordan and coworkers previously reported the influence of these copolymerizations, demonstrating that $P(iPrOx)_{25-n}$-$P(BuOx)_n$ statistical copolymers varied in their LCSTs from 25 – 50 °C when n = 0, 1, 2, 3 or 5.[14] The drastic shift in LCST through incorporation of only a handful of hydrophobic BuOx monomers demonstrates the sensitivity of these structure-property relationships. As such, to develop functional copolymers with an LCST slightly above physiological temperature we chose to pursue $P(iPrOx)_{25}$-$P(BuOx)_4$ (**3**) scaffold end-capped with a thioacetate functionality for eventual thiol-maleimide coupling to MSN surfaces as shown in **Figure 5.2 (a)**. Additionally, homopolymer poly(2-ethyl-2-oxazoline (PEtOx, **4**) end-capped with thioacetate was included as a control polymer with an LCST far above physiological temperature.

The synthesis of $P(iPrOx)_{25}$-$P(BuOx)_4$-*t*-SAc (**3**) is shown in **Figure 5.2 (b)**, and the detailed method is presented in the Experimental section. In short, after the simultaneous addition of both monomers (iPrOx and BuOx), the microwave-assisted polymerization was run and terminated with potassium thioacetate (KSAc).This procedure is analogous to the thioacetate end-capping strategy discussed in our previous work.[16] A similar synthetic procedure is followed for simple homopolymer $P(EtOx)_{50}$-*t*-SAc (**4**) abbreviated within **Figure 5.2 (c)**. The polymer structure of **3**

and **4** were confirmed by NMR as shown in **Figure S 5.1** and **S 5.2**, and the molecular weight of **3** was characterized by gel permeation chromatography (GPC) to be 3 kDa with a PDI (*Đ*) of 1.03.

To characterize the LCST of free polymers, temperature-dependent UV-Vis analysis was then performed on polymers solubilized in the MilliQ water, as described in the Experimental section. As shown in **Figure 5.2 (d)**, the LCSTs of **3** and **4** were determined to be 40 and 92 °C, respectively. The reversibility of the hydrophobicity change is also supported by the UV-Vis analysis with multiple heating and cooling cycles (**Figure S 5.4**) that the LCST is stable between 40 – 44 °C with an average at 41.9 °C.

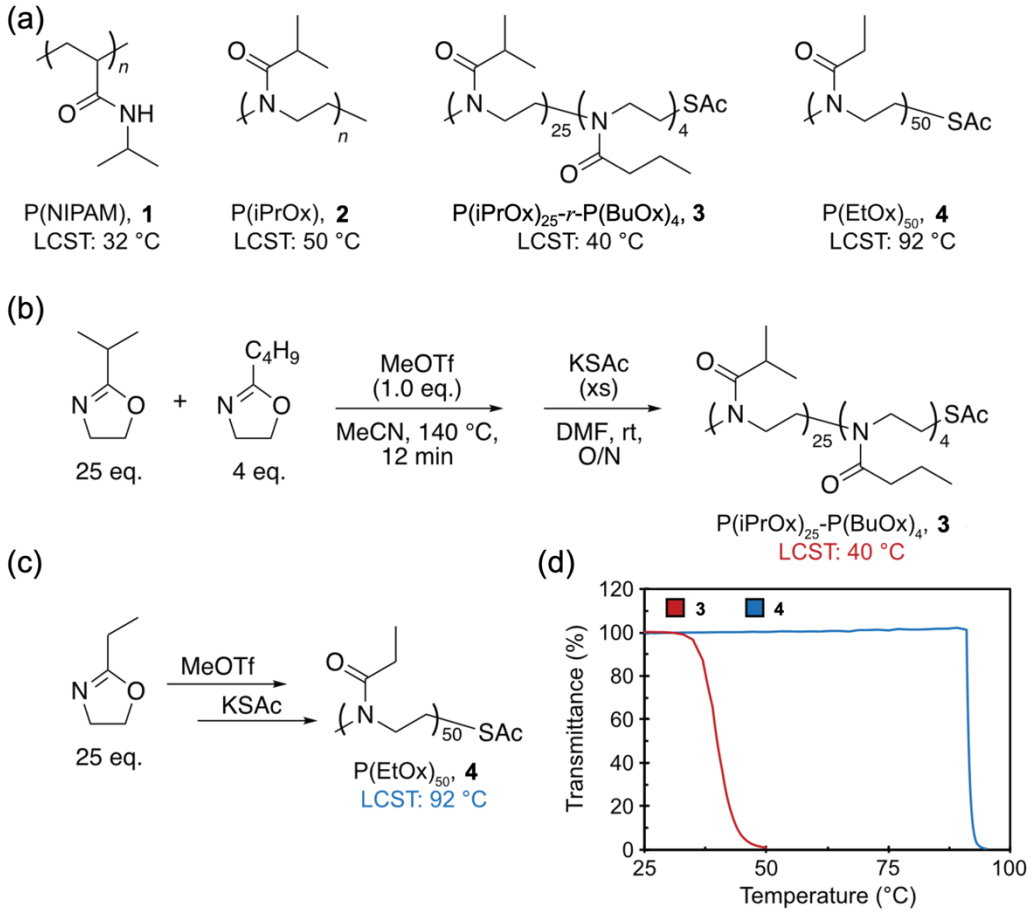

Figure 5.2 (a) Molecular structures of PNIPAm and POx polymer. Variations in the hydrophilicity of the side-chain can significantly modulate or even eliminate the LCST; (b) Synthesis route of

$P(iPrOx)_{25}$-$P(BuOx)_4$-*t*-SAc copolymer (**3**); (c) Abbreviated synthesis of homopolymer $P(EtOx)_{50}$-*t*-Sac (**4**); (d) UV-Vis transmittance of **3** and **4** at temperature gradients. The LCST of **3** and **4** are 40 and 92 °C, respectively.

After the successful synthesis of POx polymer with desired LCST, a synthesis route to conjugate both POx and Gd-DTPA to the surface of MSNs was proposed. Two kinds of nanoparticles with POx are designed: one is conjugated with $P(iPrOx)_{25}$-$P(BuOx)_4$ (**3**), and the other is conjugated with $P(EtOx)_{50}$ (**4**). The latter one is a control to examine if the appropriate LCST will realize better contrast enhancement. The conjugating route using $P(iPrOx)_{25}$-$P(BuOx)_4$ is shown in **Scheme 5.1**, and the $P(EtOx)_{50}$ conjugation is completed in the same protocol. The MSNs was synthesized and post-grafted with amine functionalization following the same method published previously.[17] From transmission electron microscopy (TEM) images shown in **Figure 5.3 (a)**, the MSNs have diameters of 100 – 120 nm with well-defined 2 nm mesopores. Then the Gd-DTPA and 6-maleimidohexanoic acid (EMCA) were coupled to the amine functionalized MSNs (MSNs-NH_2) by EDC/NHS reaction to produce Gd-DTPA and EMCA functionalized MSNs (MSNs-Gd-EMCA) in a one-pot reaction. The ratio of Gd-DTPA to EMCA was tuned by varying the concentration of each molecule to reach a higher yield. Next, the POx was coupled to the EMCA on MSNs after deprotecting the thiol terminal group to produce Gd-DTPA and POx functionalized MSNs (MSNs-Gd-POx-**3** and MSNs-Gd-POx-**4**). The conjugation of Gd-DTPA and **3** is characterized by FTIR as shown in **Figure 5.2 (c)**. The MSNs-NH_2 has a peak at 3391 cm^{-1}, and it is the N-H stretch of primary amine. After the Gd-DTPA and EMCA conjugation, the C=O stretch of maleimide amide at 1702 cm^{-1} appears.[18] After $P(iPrOx)_{25}$-$P(BuOx)_4$ conjugation, the POx amide group at 1628 cm^{-1}, C-H stretch at 1480 cm^{-1} and (C=O)-C-H at 1440 cm^{-1} appear.[19,20] The appearance of the characteristic peaks of each molecular indicates the successful

conjugation. The thermogravimetric analysis (TGA, **Figure S 5.5**) also supports successful conjugation: after the conjugation of Gd-DTPA and EMCA, the weight loss increased from 15.7% to 23.0%, and after $P(iPrOx)_{25}$-$P(BuOx)_4$ conjugation, the weight loss further increased to 33.2%. The weight percentage of Gd-DTPA coupled on MSN surfaces was also quantified by ICP-OES, and for MSNs-Gd-POx-**3**, the Gd-DTPA was 0.89%. In addition, we also prepared MSNs conjugated with both PNIPAm and Gd-DTPA (MSNs-Gd-PNIPAm) following the method in our previous work,[10] which is another control sample to verify if the LCST at body temperature can lead to a higher contrast enhancement.

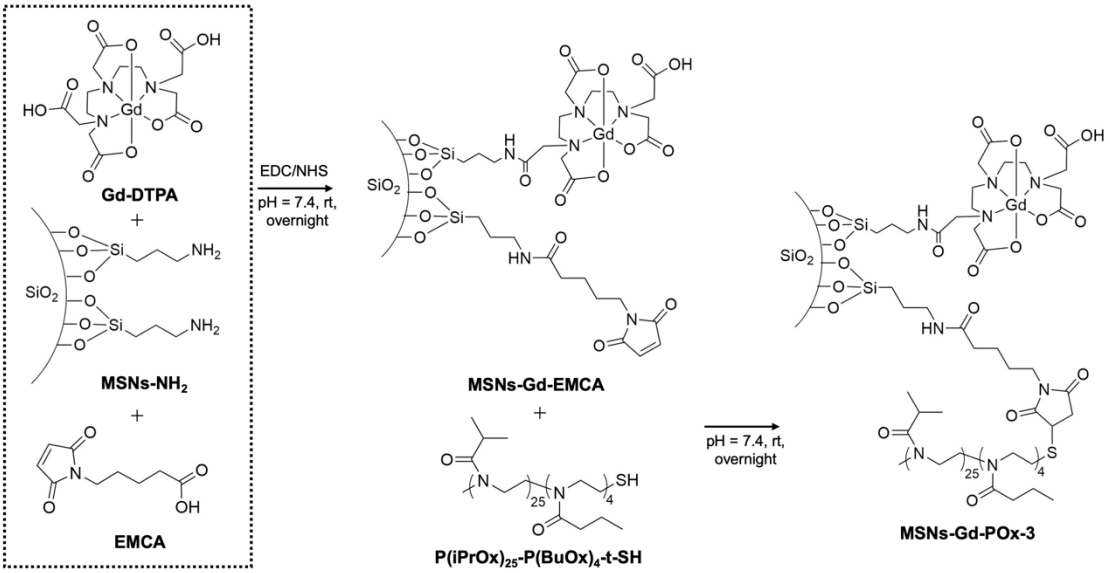

Scheme 5.1 MSNs functionalized with POx-**3** and Gd-DTPA.

To characterize the LCST of conjugated POx polymer, we performed dynamic light scattering (DLS) measurements of diluted MSNs-Gd-POx in PBS buffer. The plots of PDI and z-average of MSNs-Gd-POx-**3** are shown in **Figure 5.3 (b)**. The increase of z-average diameter indicates the aggregation of nanoparticles due to hydrophobic POx above LCST, and the increase of PDI indicates wide nanoparticle size distribution caused by their aggregation. Using this method,

we can ensure the LCST after conjugation is still in the desired range, which is around 40 °C. The LCST of conjugated **4** is confirmed to be around 65 – 75 °C using DLS (**Figure S 5.6**).

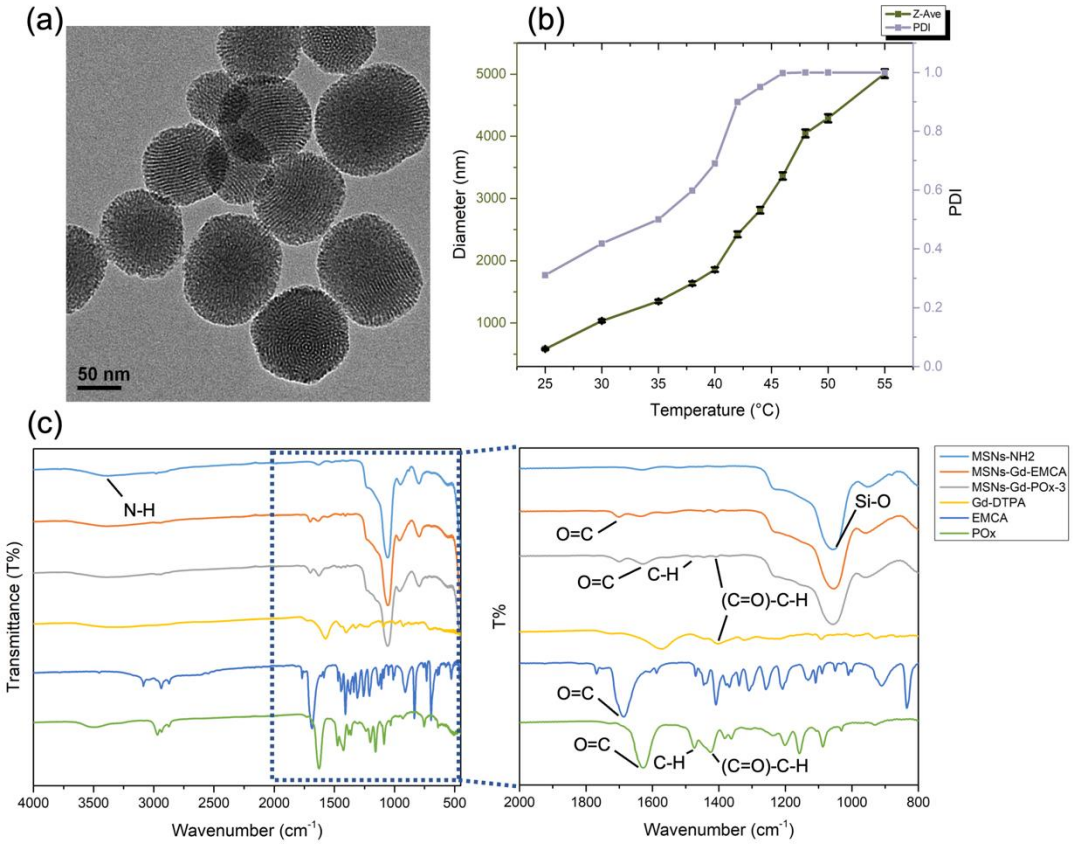

Figure 5.3 Characterization of POx modified MSNs. (a) TEM image of MSNs; (b) DLS results of MSNs-Gd-DTPA-P(iPrOx)$_{25}$-P(BuOx)$_4$ (MSNs-Gd-POx-**3**); (c) FTIR spectra of MSNs at each modification step (left) and zoom in (right).

After confirming the nanoparticles' successful synthesis, the POx and PNIPAm modified MSNs were then tested under MRIgHIFU. The nanoparticles were dispersed in the tissue-mimicking gel and milk, and placed in agarose phantom as reported in our previous work.[10] Magnevist (Mgv), the commercial T_1 contrast agent, was used as a control, and the Gd-DTPA concentration in Mgv was the same as that in MSNs-Gd-POx-**3**. The samples were treated with the same HIFU sequence as shown in **Figure 5.4 (a)**: 25 s warm up followed by 10 cycles of 5 s

on, 5 s off (0.1 Hz) modulation, both at 50% amplitude (20 W). The warm-up sequence raised the baseline temperature from room temperature (21 °C) to near body temperature (35 °C), so temperature oscillation in a small range (around 3 °C) was enough to trigger the reversible contrast change of nanoparticles. During the HIFU modulation of MSNs-Gd-POx-**3** as shown in **Figure 5.4 (a)** right, when HIFU was on, the temperature increased, and T_1W intensity decreased. It matches our hypothesis that when HIFU raises the temperature above LCST, the POx becomes hydrophobic and reduces the water access to the Gd-DTPA on the nanoparticle surfaces, so the T_1 value increases, leading to the lower T_1W intensity. Within the 10 cycles, no T_1 modulation amplitude decrease was observed, which indicated the good reversibility of nanoparticles and matched our previous reversibility test of free POx polymers. Next, we performed Fourier transform on the T_1W intensity over time on every pixel in the field of view. **Figure 5.4 (b)** shows the frequency domain spectrum of the pixel at the HIFU focal point. In the zoom in view on the top right, a peak at 0.1 Hz can be observed, which is the HIFU modulation frequency. Using this peak intensity, we mapped throughout the field of view and reconstruct the modulation enhancement map (MEM) shown in **Figure 5.4 (c)**. On the MEM, only the pixels that undergo T_1 contrast change at 0.1 Hz show intensity above the baseline, and from the color map, we can observe that all pixels with enhancement are within the sample area. The pixels at the HIFU focal point show the highest intensity because the temperature modulation there is the most intense, thus it triggers the T_1 contrast change at the highest amplitude.

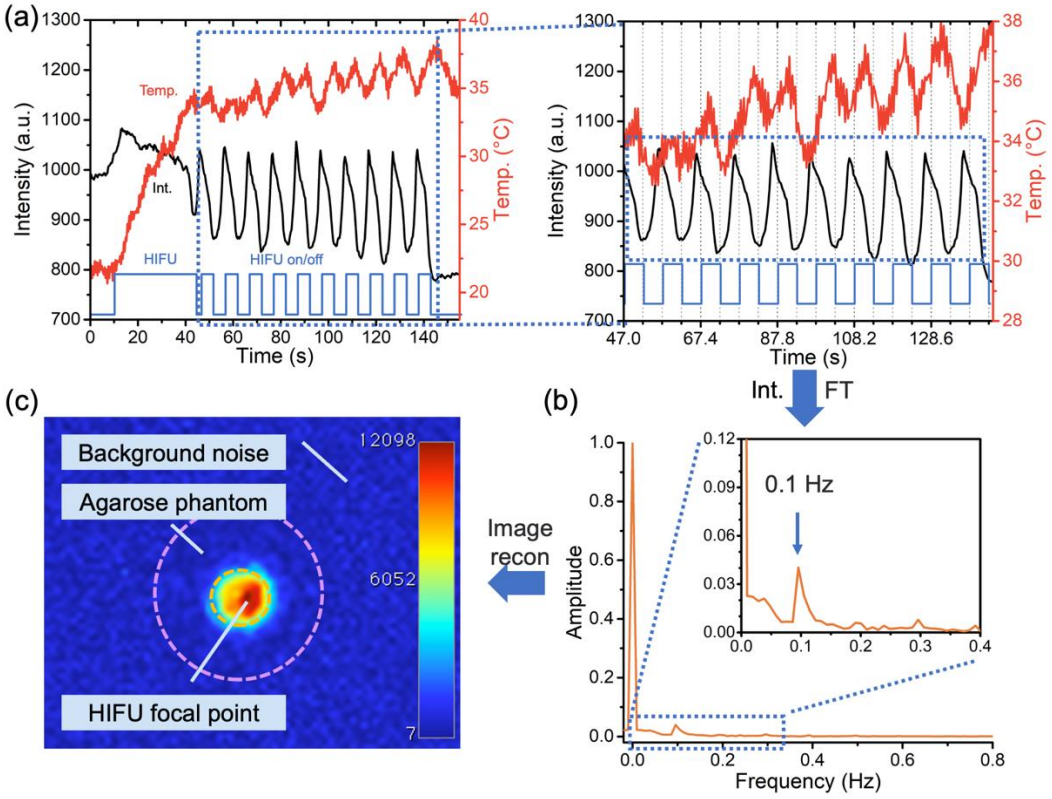

Figure 5.4 (a) Plots of T_1W signal intensity and temperature change over time (left) and zoomed-in view of the HIFU modulation time period (right); (b) Temporal Fourier transform (FT) is performed on T_1W signal intensity vs. time from (a) to generate Fourier transform spectrum; (c) Reconstructed MEM using the peak intensity of the spectral component at the HIFU modulation frequency for each pixel location (MEM displayed in color scale).

Next, the enhancement between samples and controls are compared. In **Figure 5.5**, we show the overlay of T_1W image and MEM of (a) MSNs-Gd-POx-**3** (b) Mgv control (c) MSNs-Gd-POx-**4** (d) MSNs-Gd-PNIPAm. From the overlay with T_1W image, we can observe both the outline of the target object (agarose phantom) and contrast enhancement at the HIFU focal point from MEM. With the same color scale, we can observe that MSNs-Gd-POx-**3** shows the highest enhancement at the sample region. To quantify the enhancement, we calculate contrast-noise-ratio (CNR) using the **Equation 5-1** below. Higher CNR stands for better enhancement. The CNR of the MEM of

MSNs-Gd-POx-**3** is 32.2, which is 38.8-fold higher than that of its T_1W image (CNR = 0.83). MSNs-Gd-POx-**3** also shows better enhancement compared to the two polymer control samples: its CNR is 3-fold higher than the CNR of MSNs-Gd-POx-**4**, and 1.7-fold higher than MSNs-Gd-PNIPAm. The enhancement occurs because the LCST of the two control samples are higher or lower than HIFU modulation temperature, so the hydrophobicity of the majority of the polymers on nanoparticles do not change, thus the contrast change is not significant. The results show that POx-**3** with LCST at human body temperature is essential to obtain a high enhancement fold at body temperature compared to POx-**4** and PNIPAm, which have LCST far above and below body temperature respectively. In addition, the Mgv control also shows a CNR of 10.3 and a 4.4-fold enhancement compared to its T_1W image (CNR = 2.36), which indicates that our spotlight technique can be utilized with pure thermal effect of HIFU without nanoparticles. However, the enhancement fold of MSNs-Gd-POx-**3** is 3-fold higher than that of the Mgv control, which means our functionalized nanoparticles can further enlarge the T_1 modulation range and bring a higher enhancement fold.

$$\mathbf{CNR} = \frac{|\text{Intensity of region of interest} - \text{Intensity in reference area}|}{\text{Background noise standard deviation}} \quad \text{Equation 5-1}$$

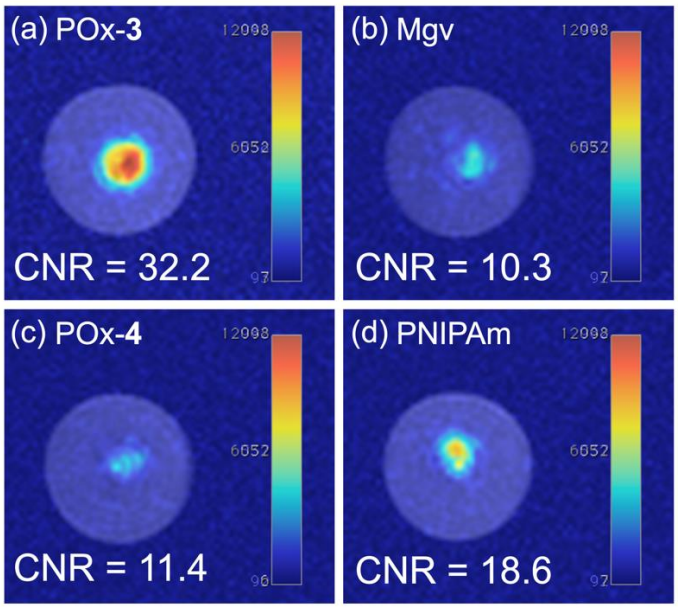

Figure 5.5 Overlay of MEM and T_1W image of (a) MSNs-Gd-POx-**3** (b) Mgv control (c) MSNs-Gd-POx-**4** (d) MSNs-Gd-PNIPAm.

To verify the mechanism of MRI contrast change of MSNs-Gd-POx, we performed Cartesian T_1 mapping and measured the T_1 value before and during HIFU stimuli. The results are shown in **Figure S 5.7**. We calculate T_1 increase percentage using **Equation 5-2** below to characterize the relative T_1 change upon HIFU stimuli. The T_1 increase percentage of MSNs-Gd-POx-**3** is 106%, which is the higher than 68%, 72% and 80% for Mgv control, MSNs-Gd-POx-**4**, and MSNs-Gd-PNIPAm respectively. The T_1 increase of Mgv control is due to the temperature increase by HIFU, and T_1 increase of MSNs-Gd-POx-**3** is from both the temperature increase and the hydrophobicity change of POx. It matches our nanoparticle design, which is the Gd-DTPA on MSN surfaces get less water access during HIFU due to the hydrophobicity of POx.

$$T_1 \text{ increase\%} = \frac{T_1 \text{ during HIFU} - T_1 \text{ before HIFU}}{T_1 \text{ before HIFU}} \quad \text{Equation 5-2}$$

5.3 Conclusions

In this work, we successfully synthesized a POx polymer with a desired LCST at 40 °C, and functionalized MSNs with POx and Gd-DTPA to realize reversible MRI T_1 contrast change with periodic HIFU. We demonstrate that MSNs-Gd-POx-**3** applied with our spotlight technique is able to bring contrast enhancement at human body temperature within a small temperature oscillation range (3 °C) and in a relatively fast data acquisition time (100 s). The contrast enhancement is 38.8-fold higher than that of the T_1W image, 3-fold higher than Mgv, and also higher than MSNs modified with polymers with LCST higher or lower human body temperature, proving that the tailored LCST is essential to bring significant contrast enhancement. This nanoparticle design brings the spotlight technique closer to clinic translation as it can work at human body temperature, and it is promising for biomedical applications such as detect tumor margins.

5.4 Experimental Section

Chemicals

Chemical reagents were purchased from Sigma-Aldrich, Alfa Aesar, Fisher Scientific, and Acros Organics and used without purification unless noted otherwise. Tetraethylorthosilicate (TEOS; 99%, Aldrich), cetyltrimethylammonium bromide (CTAB; 98%, Aldrich), sodium hydroxide (99%, Fisher Scientific), ethanol (200 proof, Aldrich). 3-aminopropyl triethoxysilane (APTES; 99%, Aldrich), EDC•HCl (99%, Covachem), sulfo-NHS (99%, Covachem), diethylenetriaminepentaacetic acid gadolinium(III) dihydrogen salt hydrate (Gd-DTPA; 97%, Aldrich), hydrochloric acid (Fisher Scientific), nitric acid (TraceMetal grade, Fisher), 6-maleimidohexanoic acid (90%, GC, Aldrich), methyl cellulose (4000 cP, Sigma), agarose BP160-100 (Molecular Biology Grade, Fisher) were used as received. Anhydrous toluene was obtained by distillation from CaH_2 under dry nitrogen.

Anhydrous and deoxygenated solvents dichloromethane (DCM), acetonitrile (MeCN), and methanol (MeOH) were dispensed from a Grubb's-type Phoenix Solvent Drying System. Thin layer chromatography was performed using Silica Gel 60 F254 (EMD Millipore) plates. Flash chromatography was executed with technical grade silica gel with 60 Å pores and 40 – 63 μm mesh particle size (Sorbtech Technologies). Solvent was removed under reduced pressure with a Büchi Rotovapor with a Welch self-cleaning dry vacuum pump and further dried with a Welch DuoSeal pump. Bath sonication was performed using a Branson 3800 ultrasonic cleaner.

All reactions were performed in glass 10 mL microwave reactor vials purchased from CEM with silicone/PTFE caps. Flea micro PTFE-coated stir bars were used in the vials with magnetic stirring set to high and 15 seconds of premixing prior to the temperature ramping. All microwave reactions were carried out at 140 °C with the pressure release limit set to 250 psi (no reactions exceeded this limit to trigger venting) and the maximum wattage set to 250W (the power applied was dynamically controlled by the microwave instrument and did not exceed this limit for any reactions). Irradiation with light was performed with BI365 nm Inspection UV LED lamp, purchased from Risk reactor (Output power density >5000μW/cm² at 15" (38cm), voltage range 90-265V ac, output power: 3×325 mW at 365 nm peak).

POx synthesis

Synthesis of poly(2-oxazoline) block copolymer **3**

To a flame dried microwave vial, MeCN (0.7 mL, anhydrous), iPrOx (200 μL, 0.200 g, 1.77 mmol, 24 equiv.), and BuOx (19 μL, 0.019 g, 0.15 mmol, 2 equiv.) were added. After purging with nitrogen, MeOTf (8.3 μL, 12 mg, 0.07 mmol, 1.0 equiv.) was added and the mixture was heated at 140 °C in the microwave. After 17 minutes, the polymerization was quenched with potassium thioacetate (64 mg, 0.55 mmol, 7.5 equiv.), and stirred at room temperature overnight.

The following day, the reaction mixture was evaporated to dryness to yield crude polymer **3** as a yellow-brown solid. Polymer **3** was purified by precipitation by dissolving in a minimal amount of DCM and dropwise addition to cold hexanes (20:1 v/v%) three times, collected and evaporated to dryness, yielding the pure product **3** as an off-white solid (120 mg, 60% yield).^{1}H NMR (500 MHz, $CDCl_3$):δ 3.46 (m, 111H), 3.07 (m, 3H), 2.91 (m, 21H), 2.66 (m, 10H), 2.36 (m, 8H), 2.27 (m, 3H), 1.35 (m, 9H), 1.11 (s, 152H), 0.92 (m, 12H).

Synthesis of poly(2-oxazoline) block copolymer **4**

To a flame dried microwave vial, MeCN (750 μL, anhydrous) and EtOx (250 μL, 0.250 g, 2.52 mmol, 50.0 equiv.) were added. MeOTf (5.7 μL, 8.3 mg, 0.050 mmol, 1.0 equiv.) was added and the mixture was heated at 140 °C in the microwave. After 16 minutes, the polymerization was quenched with potassium thioacetate (43 mg, 0.38 mmol, 7.5 equiv.), and stirred at room temperature overnight. The reaction mixture was evaporated to dryness to yield crude polymer (**4**) as a yellow-brown solid. Polymer **4** was purified by precipitation by dissolving in a minimal amount of DCM and dropwise addition to cold Et_2O (20:1 v/v%), collected and evaporated to dryness (152 mg, 61% yield). ^{1}H NMR (500 MHz, $CDCl_3$):δ 3.45 (m, 200H), 3.02 (m, 3H), 2.40–2.14 (m, 101H), 1.11 (t, 149H).

Synthesis of Gd-DTPA and POx functionalized MSNs (MSNs-Gd-DTPA-POx)

a. Synthesis of mesoporous silica nanoparticles (MSNs)

0.25 g CTAB and 875 μL of sodium hydroxide solution (2 M) were dissolved in 120 mL of water under stirring. The solution was heated at 80 °C for 30 minutes, followed by the addition of 1.5 mL of TEOS and 0.79 mL ethyl acetate under vigorous stirring. Stirring was continued for 2 h at 80 °C, and then the solution was cooled to room temperature. The nanoparticles were collected by centrifugation (15 min at 7830 rpm), washed 2 times with DI water and 3 times with ethanol

(3×30 mL) and dispersed in 20 mL ethanol for further use. Approximately 300 mg of MSNs was obtained in each batch.

b. Amine functionalization of MSNs

Around 200 mg unfunctionalized MSNs were washed 3 times with toluene (3×30 mL) and redispersed in 30 mL of dry toluene stirring in a flame-dried 50 mL round bottom flask under nitrogen. Then 120 μL (3-aminopropyl)triethoxysilane was added drop by drop and the resulting mixture was refluxed in a 110 °C oil bath under nitrogen overnight. The amine-modified MSNs were collected by centrifugation (10 min at 7830 rpm) and washed 3 times with ethanol (3×30 mL). The product was redispersed in 20 mL ethanol for further use.

c. CTAB extraction of amine functionalized MSNs (MSNs-NH_2)

The APTES-functionalized MSNs dispersed in toluene were washed twice with ethanol (2×30 mL). To extract the organic template from the pores, the nanoparticles were dispersed in 80 mL of an acidic ethanolic solution (EtOH:HCl= 90/10 (v/v)), refluxed for 1 h, and collected by centrifugation (10 min at 7830 rpm). This procedure was repeated one more time. The product was washed twice with ethanol (2×30 mL) and stored in ethanol.

d. Gd-DTPA and 6-maleimidohexanoic acid (EMCA) functionalization on MSNs

50 mg MSNs-NH_2 dispersed in ethanol were washed 3 times with DI water (3×10 mL), then were dispersed in 5 mL HEPES buffer (pH=7.4) for future use. 0.4 mL of Gd-DTPA water solution (0.10 g/mL, pH=6.7) was mixed with 2 mL MES buffer (100 mM, pH = 6.0), 13 mg EDC•HCl and 10 mg sulfo-NHS, and the mixture was stirred for 20 min. At the same time, 8 mg EMCA was dissolved in 2 mL MES buffer (100 mM, pH = 6.0), then 10 mg EDC and 7 mg sulfo-NHS mixture were added to the solution and mixed for 20 min. Next, MSNs-NH_2 dispersion, Gd-DTPA and EMCA solution were mixed and stirred in room temperature for 24 h. Gd-DTPA and EMCA

functionalized MSNs (MSNs-Gd-DTPA-EMCA) products were washed 3 times with DI water (3×10 mL).

e. POx conjugation on MSNs-Gd-DTPA-EMCA

10 mg MSNs-Gd-DTPA-EMCA were dispersed in 5 mL HEPES buffer (pH=7.4). 5 mg POx polymer was dissolved in 1 mL DI water and 2 uL NaOH (2 M) was added. Then the solution was mixed and stirred at room temperature for 1 h. Next, 2 uL HNO_3 (2 M) was added to neutralize the pH to 7. The POx solution was added to MSNs-Gd-DTPA-EMCA dispersion and stirred at room temperature overnight. The MSNs-Gd-DTPA-POx were washed 3 times with DI water (3×10 mL).

Tissue mimicking gel and MRI-guided HIFU sample preparation

1 g methyl cellulose was slowly added to 15 mL boiled water and stirred for 3 min. Then 25 mL condensed milk was added followed by 10 mL cold water. The mixture was stored in a refrigerator overnight to eliminate air bubbles. 2 mg nanoparticles were dispersed in 0.5 mL water and then mixed with 1 mL gel/milk mixture, resulting in a 1.3 mg/mL nanoparticle gel/milk mixture. The Mgv control was made in a similar manner and the Gd-DTPA concentration was the same as nanoparticle samples. Mgv was first diluted to 0.5 mL water and then mixed with 1 mL gel/milk mixture.

Agarose phantom

17.5 g agarose was slowly added to 500 mL hot water with stirring. Then the solution was heated up to boiling, and then poured into a sample holder mold. After agarose was solidified under room temperature, it was stored in a refrigerator for further use.

Material Characterization

Transmission electron microscopy (TEM)

TEM images were recorded on a Tecnai T12 Quick CryoEM at an accelerating voltage of 120 kV. A suspension (8 μL) of nanoparticles in ethanol was dropped on a 200-mesh carbon coated copper grid and the solvent was allowed to evaporate at room temperature.

Dynamic light scattering (DLS)

Size analysis: The nanoparticle solution was diluted in MilliQ H_2O at 50 μg/mL in a plastic 1 cm cuvette. Size was analyzed with a Malvern Zetasizer Nano dynamic light scattering. In each measurement temperature, there are 10 runs, 10 seconds/run, three measurements, no delay between measurements, and each temperature has 120 second equilibration time. Collection parameters: Lower limit = 0.6, Upper limit = 1000, Resolution = High, Number of size classes = 70, Lower size limit = 0.4, Upper size limit = 1000, Lower threshold = 0.05, Upper threshold = 0.01. Temperature ranges from 25 to 55 °C for MSNs-Gd-POx-**3**, and 25 to 75 °C for MSNs-Gd-POx-**4**.

UV-Vis

Transmittance profiles of polymers were obtained in MilliQ water at 5 mg/mL polymer. Analyzed from 25 to 90 °C with 0.1 °C increments, 15 second equilibration between measurements, blanked versus polymer solution at room temperature (~25 °C). Spectra was taken from 300–700 nm in a 0.3 mL quartz cuvette without stirring. Temperature controlled via UV-Vis equipped with air-cooled Peltier. Analysis was performed at 600 nm. The LCST was defined as the temperature at which transmittance falls to 50%.

NMR

Nuclear magnetic resonance (^{1}H NMR) spectra were taken on Bruker Avance 500 (^{1}H NMR and ^{13}C NMR) or AV-300 (^{19}F NMR) instruments and processed with MestReNova software. All ^{1}H NMR peaks are reported in reference to $CDCl_3$ at 7.26 ppm.

GPC

Size Exclusion Chromatography (SEC)/Gel Permeation Chromatography (GPC), unless otherwise noted, was conducted on a Shimadzu high performance liquid chromatography (HPLC) system with a refractive index detector RID-10A, one Polymer Laboratories PLgel guard column, and two Polymer Laboratories PLgel 5 μm mixed D columns. Eluent was DMF with LiBr (0.1 M) at 50 °C (flow rate: 0.80 mL/min). Calibration was performed using near-monodisperse poly(methyl-methacrylate) PMMA standards from Polymer Laboratories. Masses for analytical measurements were taken on a Sartorius MSE6.6S-000-DM Cubis Micro Balance. Microwave reactions were performed using a CEM Discover SP microwave synthesis reactor.

Thermogravimetric analysis (TGA)

TGA was performed using a Perkin-Elmer Pyris Diamond TG/DTA under air (200 mL/min). Approximately 5 mg of sample was loaded into aluminum pans. The sample was held at 100 °C for 30 minutes, and then the data were recorded during a temperature scan from 100 to 600 °C at a scan rate of 10 °C/min and an isothermal process of 600 °C for 80 min. The plotted values are normalized to the weight at 100 °C. An empty aluminum pan was used as a reference.

Quantification of Gd-DTPA by inductively coupled plasma atomic emission spectroscopy (ICP-OES)

ICP-OES measurements were made using ICPE-9000 Shimadzu. 0.1 mL of sodium hydroxide solution (2 M) was added to approximately 0.5-1 mg nanoparticle samples dispersed in

0.05 mL of Milli-Q water, and the mixture was sonicated for 1 h. Then 0.1 mL of nitric acid (2 M) was added, and the mixture was sonicated for 1h. The solution was then diluted to 10 mL with 2% nitric acid for measurement.

MRIgHIFU experiments

MRIgHIFU

All MRI-guided HIFU experiments were conducted using a research-dedicated HIFU system (Image Guided Therapy, Bordeaux, France) integrated with a whole-body 3 T MRI scanner (MAGNETOM Prisma, Siemens Healthineers, Erlangen, Germany). The HIFU system had an 8-element annular transducer array with a diameter of 25 mm, frequency of 2.5 MHz, a focal point of $0.7\times0.7\times3mm^3$ in size, and a peak electrical power output of 80 W.

MRI Data Acquisition

Golden-angle-ordered 3D stack-of-radial multi-echo spoiled gradient echo sequence was used to acquire rapid dynamic MRI images. Such sequence has been proved to provide a balance between spatial and temporal resolution, while still maintaining high volumetric coverages and SNR from our previous study.[21] The data were acquired in axial view with the following parameters: field of view = $109\times109\times18$ mm^3, matrix size $96\times96\times6$, 4 echoes, TE1/ΔTE = 1.59/1.29, TR = 7.79 ms, flip angle = 6°.

T_1-weighted gradient-echo images were acquired with both transversal (Field of view [FOV]=$213\times213\times48mm^3$, matrix size=$192\times192\times24$, flip angle=15°, TE=2.15ms, TR=4.6ms) and coronal (FOV=$180\times180\times64mm^3$, matrix size=$192\times192\times32$, flip angle=15°, TE=2.15ms, TR=4.6ms) orientations to locate the natural focal point of the HIFU beam, which was used throughout the experiment without any electronic or mechanical steering.

3D Cartesian variable flip angle (VFA) T1 mapping method was used to estimate the T1 value before and after HIFU stimuli. Parameters for VFA were flip angles = 1°, 2°, 5°, 7°, 9°, Field of view [FOV]=180×180×48mm, matrix size = 192×192×16, TE = 2.29 ms, TR = 6 ms. B_1^+ field variation was measured with a vender-recommended protocol, and the resulting B_1^+ maps were used in a standard VFA fitting procedure to provide T_1 maps.

Image Reconstruction

Image reconstruction was performed offline with MATLAB R2017b (MathWorks. Natick, MA). To further improve temporal resolution of our dynamic MRI images and enhance SNR, a k-space weighted imaging contrast (KWIC) filter was applied on the acquired radial k-space data following a sliding window fashion[22,23], where the most recently acquired data filling the innermost annulus. Two key reconstruction parameters, temporal resolution (Tr), which stands for the time to acquire innermost k-space data in a KWIC filter, and temporal footprint (Tf), which stands for the time to acquire the entire k-space data in a KWIC filter, were set to 0.37 s and 10.9 s, respectively, after being carefully optimized based on spatial sharpness. Gridding, 3D density compensation, coil combination and coil combination were then performed to reconstructed dynamic images. Details MR acquisition and reconstruction parameters are listed in **Table 5.1**.

MR Temperature Measurement

A fast and accurate dynamic temperature measurement is crucial for (1) monitoring if the target temperature during is within physiological condition, and (2) validating the thermo-responsive mechanism of our designed nanoparticles. Proton resonance frequency (PRF)-based MR thermometry was used, where the relationship between relative temperature change and MR phase change is described by **Equation 5-3**, where $\phi(T)$ and $\phi(T_0)$ are the phase value at the

current time point and at a reference time point, γ is gyromagnetic ratio, α is a constant PRF change coeeficient =-0.01ppm/°C, B_0 is magnetic field strength, and τ is echo time.

$$\Delta T = \frac{\phi(T)-\phi(T_0)}{\gamma \alpha B_0 \tau}$$ Equation 5-3

Table 5.1 MRI Acquisition and Reconstruction Parameters

Parameter name	Parameter Value
Field of view (mm^3)	109×109×18
Matrix size	96×96×6
Resolution (mm^3)	1.13×1.13×3
Flip Angle (°)	6
TR (ms)	7.79
No. TE/TE_1/ΔTE (ms)	6/1.59/1.29
No. of radial spokes in center a KWIC filter	8
No. of total radial spokes in a KWIC filter	233
Temporal resolution (s)	0.37
Temporal footprint (s)	10.9

5.5 Supporting Information

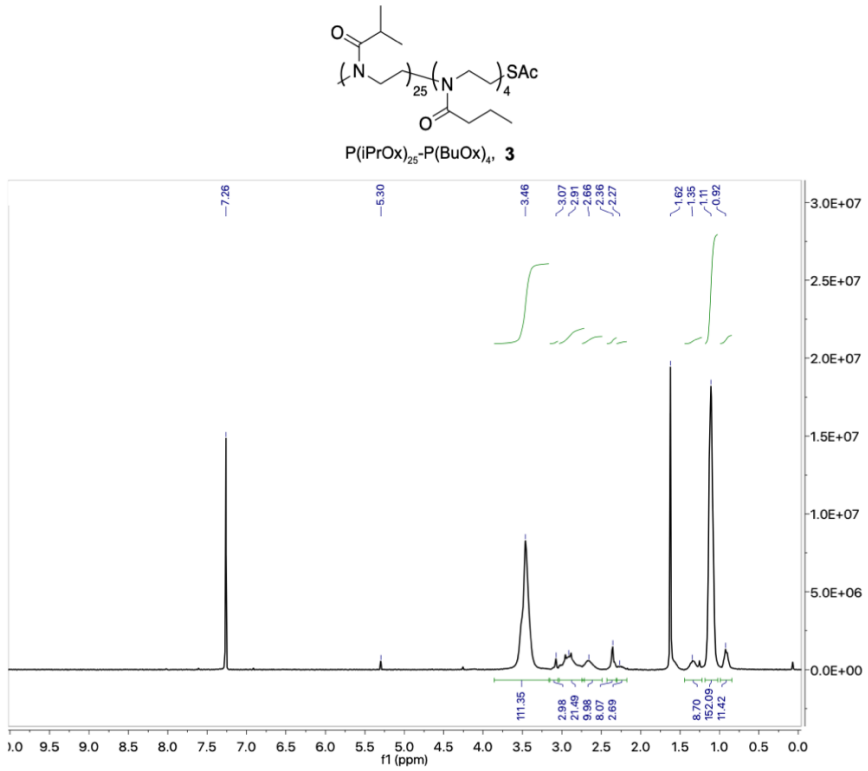

Figure S 5.1 ^{1}H NMR (500 MHz, $CDCl_3$) of copolymer (P(iPrOx)$_{25}$-*r*-P(BuOx)$_4$)-*t*-Sac (**3**).

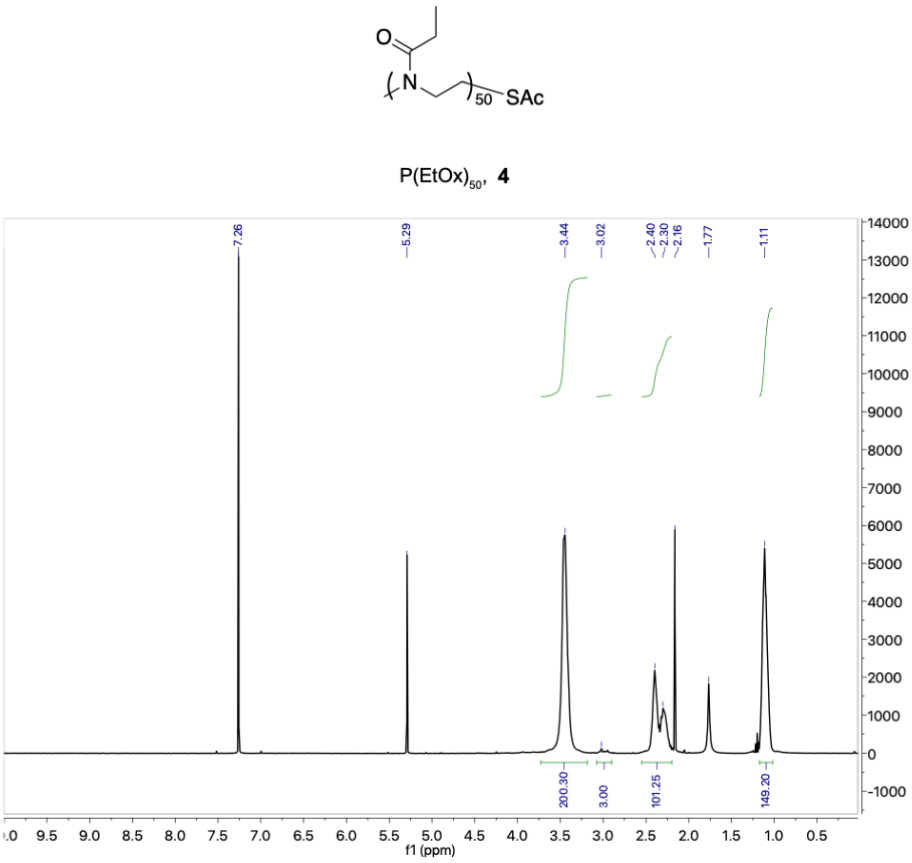

Figure S 5.2 ^{1}H NMR (500 MHz, $CDCl_3$) of copolymer P(EtOx)$_{50}$-*t*-Sac (**4**).

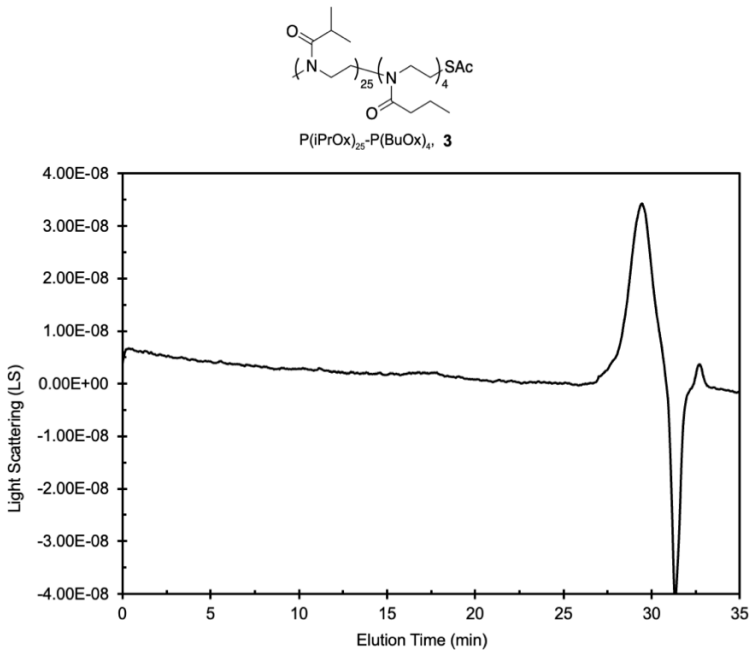

Figure S 5.3 Gel permeation chromatography (GPC) results of copolymer **3** ($P(iPrOx)_{25}$-*r*-$P(BuOx)_4$)-*t*-SAc.

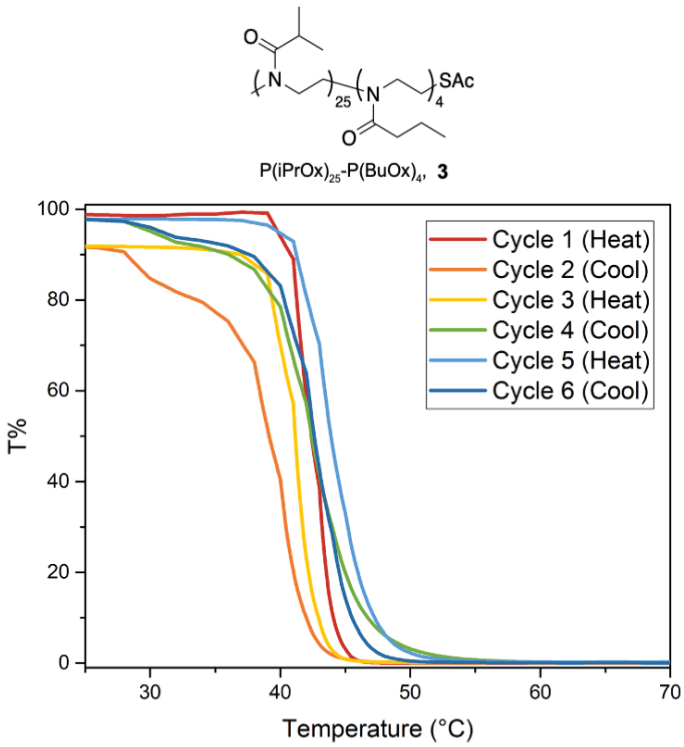

Figure S 5.4 Temperature-dependent UV-Vis transmittance of **3** with 6 heating and cooling cycles. The LCST of cycle 1-6 is 42.3 °C, 39.1 °C, 41.1 °C, 42.4 °C, 43.9 °C, and 42.6 °C. The average LCST among 6 cycles is 41.9 ± 1.6 °C.

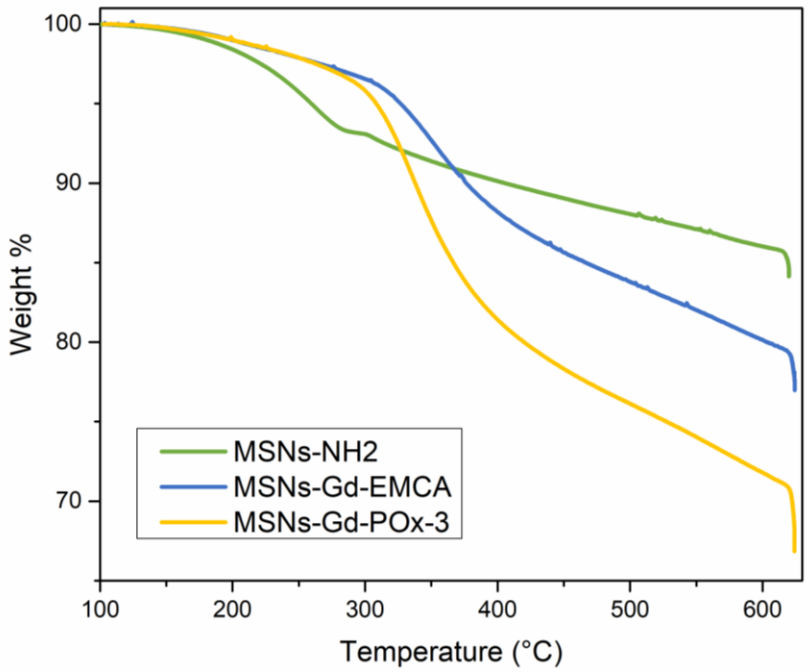

Figure S 5.5 TGA results of MSNs-NH_2, MSNs-Gd-EMCA, and MSNs-Gd-POx-**3**

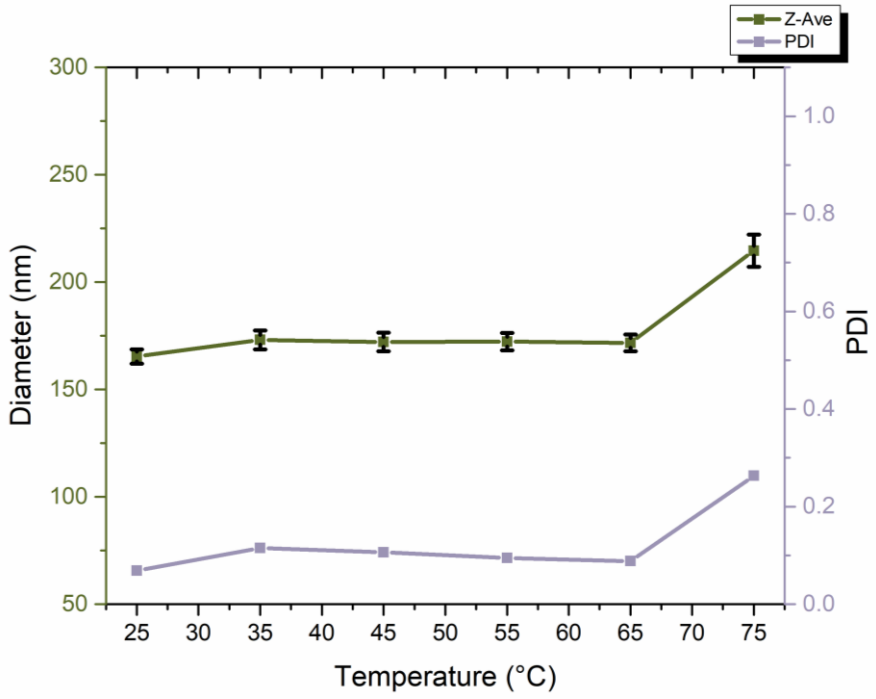

Figure S 5.6 DLS results of MSNs-Gd-DTPA-PEtOx (MSNs-Gd-POx-**4**).

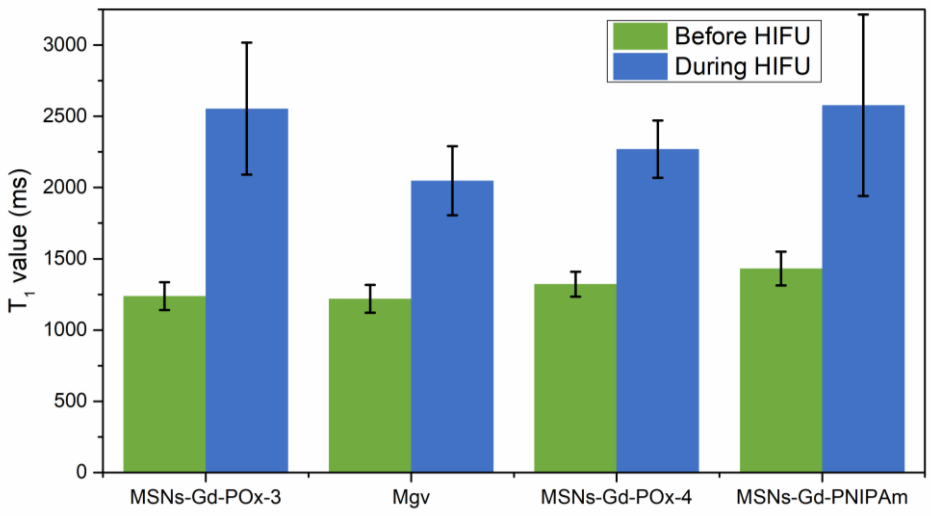

Figure S 5.7 T_1 value of samples and controls before and during HIFU stimuli. The T_1 increase percentage of MSNs-Gd-POx-**3**, Mgv control, MSNs-Gd-POx-**4**, and MSNs-Gd-PNIPAm are 106%, 68%, 72% and 80%.

5.6 References

(1) de Senneville, B. D.; Moonen, C.; Ries, M. MRI-Guided HIFU Methods for the Ablation of Liver and Renal Cancers. *Therapeutic Ultrasound* **2016**; 43–63.

(2) Chen, Y.; Chen, H.; Sun, Y.; Zheng, Y.; Zeng, D.; Li, F.; Zhang, S.; Wang, X.; Zhang, K.; Ma, M.; He, Q.; Zhang, L.; Shi, J. Multifunctional Mesoporous Composite Nanocapsules for Highly Efficient MRI-Guided High-Intensity Focused Ultrasound Cancer Surgery. *Angew. Chemie - Int. Ed.* **2011**, *50*, 12505–12509.

(3) Hynynen, K. MRIgHIFU: A Tool for Image-Guided Therapeutics. *J. Magn. Reson. Imaging* **2011**, *34*, 482–493.

(4) Huisman, M.; Lam, M. K.; Bartels, L. W.; Nijenhuis, R. J.; Moonen, C. T.; Knuttel, F. M.; Verkooijen, H. M.; van Vulpen, M.; van den Bosch, M. A. Feasibility of Volumetric MRI-Guided High Intensity Focused Ultrasound (MR-HIFU) for Painful Bone Metastases. *J. Ther. Ultrasound* **2014**, *2*, 1–10.

(5) Hurwitz, M. D.; Ghanouni, P.; Kanaev, S. V.; Iozeffi, D.; Gianfelice, D.; Fennessy, F. M.; Kuten, A.; Meyer, J. E.; Leblang, S. D.; Roberts, A.; Choi, J.; Larner, J. M.; Napoli, A.; Turkevich, V. G.; Inbar, Y.; Tempany, C. M. C.; Pfeffer, R. M. Magnetic Resonance-Guided Focused Ultrasound for Patients with Painful Bone Metastases: Phase III Trial Results. *J. Natl. Cancer Inst.* **2014**, *106*, 1–9.

(6) Maloney, E.; Hwang, J. H. Emerging HIFU Applications in Cancer Therapy. *Int. J. Hyperth.* **2015**, *31*, 302–309.

(7) Lin, F. C.; Xie, Y.; Deng, T.; Zink, J. I. Magnetism, Ultrasound, and Light-Stimulated Mesoporous Silica Nanocarriers for Theranostics and Beyond. *J. Am. Chem. Soc.* **2021**, *143*, 6025–6036.

(8) Cheng, C.-A.; Chen, W.; Zhang, L.; Wu, H. H.; Zink, J. I. Magnetic Resonance Imaging of High-Intensity Focused Ultrasound-Stimulated Drug Release from a Self-Reporting Core@ Shell Nanoparticle Platform. *Chem. Commun.* **2020**, *56*, 10297–10300.

(9) Cheng, C. A.; Chen, W.; Zhang, L.; Wu, H. H.; Zink, J. I. A Responsive Mesoporous Silica Nanoparticle Platform for Magnetic Resonance Imaging-Guided High-Intensity Focused Ultrasound-Stimulated Cargo Delivery with Controllable Location, Time, and Dose. *J. Am. Chem. Soc.* **2019**, *141*, 17670–17684.

(10) Deng, T.; Zhang, L.; Wu, H. H.; Zink, J. I. A Nanoparticle Enabled Focused Ultrasound-Stimulated Magnetic Resonance Imaging Spotlight. *Chem. Commun.* **2019**, *55*, 10261–10264.

(11) Zhu, L.; Altman, M. B.; Laszlo, A.; Straube, W.; Zoberi, I.; Hallahan, D. E.; Chen, H. Ultrasound Hyperthermia Technology for Radiosensitization. *Ultrasound Med. Biol.* **2019**, *45*, 1025–1043.

(12) Hoogenboom, R.; Thijs, H. M. L.; Jochems, M. J. H. C.; Van Lankvelt, B. M.; Fijten, M. W. M.; Schubert, U. S. Tuning the LCST of Poly(2-Oxazoline)s by Varying Composition and Molecular Weight: Alternatives to Poly(N-Isopropylacrylamide)? *Chem. Commun.* **2008**, 44, 5758–5760.

(13) Hoogenboom, R.; Schlaad, H. Thermoresponsive Poly(2-Oxazoline)s, Polypeptoids, and Polypeptides. *Polym. Chem.* **2017**, *8*, 24–40.

(14) Huber, S.; Jordan, R. Modulation of the Lower Critical Solution Temperature of 2-Alkyl-2-Oxazoline Copolymers. *Colloid Polym. Sci.* **2008**, *286*, 395–402.

(15) Luxenhofer, R.; Schulz, A.; Roques, C.; Li, S.; Bronich, T. K.; Batrakova, E. V.; Jordan, R.; Kabanov, A. V. Doubly Amphiphilic Poly(2-Oxazoline)s as High-Capacity Delivery Systems for Hydrophobic Drugs. *Biomaterials* **2010**, *31*, 4972–4979.

(16) Estabrook, D. A.; Day, R. A.; Sletten, E. M. Redox-responsive Gene Delivery from Perfluorocarbon Nanoemulsions through Cleavable Poly(2-oxazoline) Surfactants. *Angew. Chemie* **2021**.

(17) Ruehle, B.; Clemens, D. L.; Lee, B.-Y.; Horwitz, M. A.; Zink, J. I. A Pathogen-Specific Cargo Delivery Platform Based on Mesoporous Silica Nanoparticles. *J. Am. Chem. Soc.* **2017**, *139*, 6663–6668.

(18) Sahatsapan, N.; Rojanarata, T.; Ngawhirunpat, T.; Opanasopit, P.; Tonglairoum, P. 6-Maleimidohexanoic Acid-Grafted Chitosan: A New Generation Mucoadhesive Polymer. *Carbohydr. Polym.* **2018**, *202*, 258–264.

(19) De Macedo, C. V.; Da Silva, M. S.; Casimiro, T.; Cabrita, E. J.; Aguiar-Ricardo, A. Boron Trifluoride Catalyzed Polymerisation of 2-Substituted-2-Oxazolines in Supercritical Carbon Dioxide. *Green Chem.* **2007**, *9*, 948–995.

(20) Ozkose, U. U.; Altinkok, C.; Yilmaz, O.; Alpturk, O.; Tasdelen, M. A. In-Situ Preparation of Poly(2-Ethyl-2-Oxazoline)/Clay Nanocomposites via Living Cationic Ring-Opening Polymerization. *Eur. Polym. J.* **2017**, *88*, 586–593.

(21) Zhang, L.; Armstrong, T.; Li, X.; Wu, H. H. A Variable Flip Angle Golden-angle-ordered 3D Stack-of-radial MRI Technique for Simultaneous Proton Resonant Frequency Shift and T1-based Thermometry. *Magn. Reson. Med.* **2019**.

(22) Song, H. K.; Dougherty, L. Dynamic MRI with Projection Reconstruction and KWIC Processing for Simultaneous High Spatial and Temporal Resolution. *Magn. Reson. Med. An Off. J. Int. Soc. Magn. Reson. Med.* **2004**, *52*, 815–824.

(23) Song, H. K.; Dougherty, L. K-Space Weighted Image Contrast (KWIC) for Contrast Manipulation in Projection Reconstruction MRI. *Magn. Reson. Med. An Off. J. Int. Soc. Magn. Reson. Med.* **2000**, *44*, 825–832.

Chapter 6. High-Intensity Focused Ultrasound Responsive Hydrophobic Drug Delivery Based on Large Pore Mesoporous Silica Nanoparticles

6.1 Introduction

Delivery of hydrophobic drugs has been a research focus for decades. The hydrophobic drug cannot be directly dissolved in aqueous solution, so the bioavailability in patients is a concern.[1] Chemists have designed all kinds of delivery vehicles on the nano scale to realize efficient drug transportation in tissue and on-demand drug release, such as liposomes[2,3], micelles[4,5], hydrogels[6,7], and nanoparticles with various functionalizations[8–11]. High-intensity focused ultrasound (HIFU) is a non-invasive therapeutic technique, and there is much research focusing on HIFU triggered drug release.[12–15] Because the thermal and/or mechanical effects of HIFU can open the capping molecules on the nanoparticle's surface and accelerate the drug molecule diffusion[16,17], HIFU is promising to trigger hydrophobic drug release. There have been studies about ultrasound-responsive hydrophobic drug release from hydrogels[18] and nanodroplets attached microbubbles[19].

In this work, we demonstrated HIFU responsive hydrophobic drug (Docetaxel) release from large-pore mesoporous silica nanoparticles (LPMSNs) in biological-relevant media. The drug release capacity was high, the nanoparticles showed good dispersibility after drug loading, and the nanoparticles stayed intact afterward. In addition, we studied and compared the drug delivery performance of two functionalization on LPMSNs, and the influence on solvent and HIFU parameters.

6.2 Results and Discussion

Docetaxel molecule has a molecular weight of 807.9 $g \cdot mol^{-1}$, and it is a relatively large molecule compared to the 2 nm pores at regular mesoporous silica nanoparticles (MSNs). In a preliminary study, we have tried to load docetaxel into the MSNs with regular pores, but the loading capacity was around 6 wt%. We hypothesized that larger pores were needed to effectively load Docetaxel. To synthesize the nanoparticles with enlarged pores, we used trimethylbenzene (TMB) as a pore swelling agent and ammonia as a base. After the synthesis, cetyltrimethylammonium bromide (CTAB) and TMB were extracted. As shown in the TEM images in **Figure 6.1 (a)**, the diameter of LPMSNs is around 90 nm. The pores are radial instead of parallel, and the size of the pore opening near the LPMSN surfaces is around 8 – 10 nm. The LPMSNs showed good dispersibility, and it was further characterized by dynamic light scattering (DLS) that the hydrodynamic radius is 96.2 ± 8.9 nm.

To explore if the surface charge and functionalization will affect drug loading performance, we also design two kinds of LPMSNs with amine functionalization. The pure LPMSNs are negatively charged (-30.94 ± 1.28 mV), and the amine functional group is positively charged, so it can help study the influence from the surface charge. Also, the amine functional group can be further functionalized, for example with a fluorescent label or Gd-DTPA as an MRI T_1 contrast agent. One method of introducing the amine functional group is to co-condense (3-aminopropyl)triethoxysilane (APTES) into the silica backbone. The synthesis is similar to LPMSNs' synthesis route, but instead of adding TEOS, TEOS is mixed with APTES first before adding to the solution. By this method, the product LPMSNs-NH_2 has evenly distributed amine functional groups both on the outer surface and in the pore wall. The advantage of this method is that it is a one-pot reaction, and it does not require additional modification steps. The disadvantage

is that the morphology of the nanoparticle changes. As shown in the TEM image in **Figure 6.1 (b)**, the diameter of nanoparticles reduced to 50 nm. The pore structure was radial and similar to the LPMSNs, but with a smaller diameter of the nanoparticles, the size of the pore opening reduced to around 6 – 8 nm. The hydrodynamic diameter from DLS was 52.0 ± 4.6 nm, which matched the TEM result. The zeta-potential was 22.28 ± 1.2 mV, and it showed the successful introduction of the amine functional group. The other method of amine functionalization is post-grafting. It requires an APTES grafting step in toluene after the LPMSNs is synthesized and surfactant is extracted, but the morphology of LPMSNs is retained. The TEM image in **Figure 6.1 (c)** shows that the diameter of the nanoparticles after post-grafting was still around 90 nm, and the pore structure stayed intact. The DLS result showed the diameter was 186.2 ± 3.4 nm, and the zeta-potential was 34.35 ± 0.92 mV.

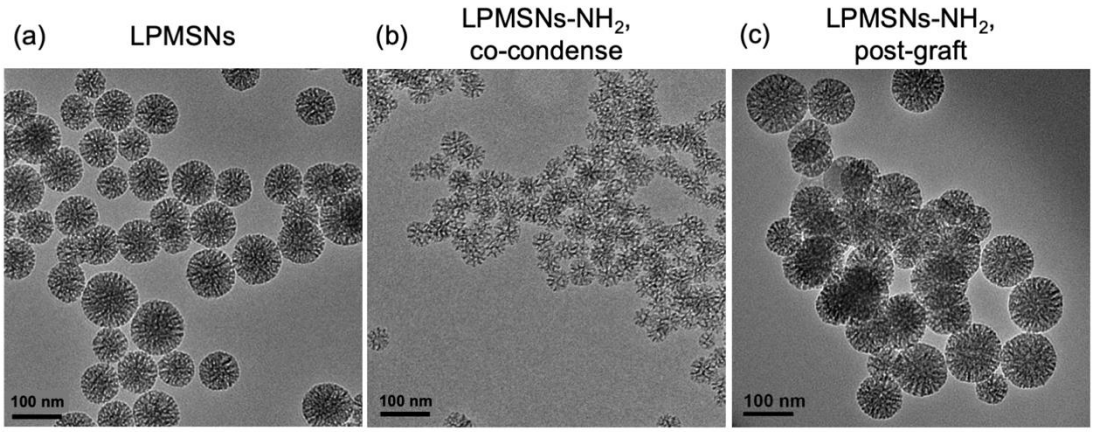

Figure 6.1 TEM images of (a) LPMSNs; (b) LPMSNs-NH_2 co-condense; (c) LPMSNs-NH_2 post-grafting. The scale bars in all images are 100 nm.

To load hydrophobic drugs into the LPMSNs, we design the solvent evaporation process to maximize the drug loading capacity. After dispersing nanoparticles in the drug solution, we aim to slowly evaporate the solvent so that small crystal/precipitate will form inside the large pores instead of forming large crystal/precipitate outside of the pores. In this way, the majority of

hydrophobic drug molecules are inside the pores, so that the nanoparticles retain their dispersibility in the aqueous solution. The drug we use was Docetaxel in this study. Docetaxel has very low solubility in water (6 – 7 μg/mL), but relatively high solubility in ethanol and dimethyl sulfoxide (DMSO). Ethanol can be evaporated at room temperature easily, so we chose ethanol as the solvent for drug loading. the drug loading process was terminated when 10% solvent was left because at this point the drug molecule was concentrated enough to form crystallized/precipitated inside the pores. We do not wait until the solvent is 100% evaporated because it may cause larger crystal/precipitate to form outside of the nanoparticles, resulting in poor nanoparticle dispersibility. After the drug loading, the nanoparticles were washed with DI water to prevent the drug leakage and to wash out the remaining ethanol in the pores.

To characterize the drug release performance, ethanol was used to extract the Docetaxel loaded and **Equation (6-1)** was used to calculate the release capacity. **Figure 6.2 (a)** shows the release results of Docetaxel-loaded LPMSNs, and the total release capacity is 40.9%. To confirm that the drug is loaded inside of the pore instead of forming large crystal/precipitate outside of nanoparticles, we checked the TEM images of Docetaxel-loaded LPMSNs dispersed in water. As shown in **Figure 6.2 (b)**, the nanoparticles stay intact after drug loading, and the pore structure is still well-defined. **Figure 6.2 (c)** shows a large field of view, and we can observe that there was no nanoparticle aggregation or large crystal/precipitate after drug loading. It indicates that the drug loading capacity is truly from the drug loaded inside of the pores, not from the crystal/precipitate of the free drug. From DLS results (202.4 ± 0.79 nm), we do not find any aggregation, either. The zeta-potential was -28.35 ± 1.51 mV, which was similar to that before drug loading. After confirming that the solvent evaporation method can load Docetaxel and realize a high release capacity, we loaded the drug into LPMSNs with amine modification using the same method.

$$Release\ capacity = \frac{Weight\ of\ drug\ released}{Weight\ of\ nanoparticle} \times 100\% \quad \text{Equation}(6-1)$$

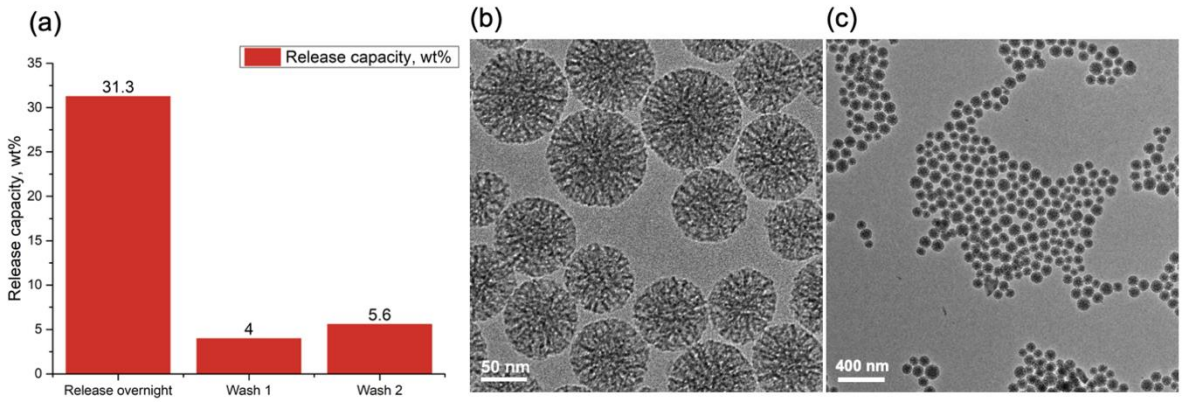

Figure 6.2 Characterizations after Docetaxel was loaded into LPMSNs. (a) Release results of Docetaxel-loaded LPMSNs in ethanol, the total release capacity is 40.9%; (b) – (c) TEM images of Docetaxel-loaded LPMSNs. The pore structure is clear and there is no crystal/precipitate observed in the zoom-out view. The scale bar in (b) is 50 nm, and the one in (c) is 400 nm.

Next, the drug release performance was tested with the HIFU triggers, and all the results are summarized in **Table 6.1**. Because the HIFU trigger will generate heat in the solution, and ethanol can be easily evaporated and bring error to the concentration measurement, a DMSO and water mixture (1:1) was chosen as the release media in the HIFU experiments. Nanoparticles were dispersed in water before the HIFU experiment to avoid pre-mature release, and DMSO was mixed right before the HIFU experiments. To calibrate the drug release due to the heating from the solvent mixture, and the diffusion of nanoparticles into the agarose phantom, we set up a control sample, LPMSNs no HIFU, that underwent the exact same experimental procedures, including being placed in agarose phantom for the same amount of time, except the HIFU treatment. The Docetaxel release results treated by 50% HIFU amplitude (22 W) for 2 min are shown in **Figure 6.3 (a)**. The release in phantom refers to the release caused by HIFU for HIFU treated samples. Because wash 1 was finished within 10 min after the release in phantom measurement, and it was mainly to wash

out the released drug from HIFU treatment, it could also be regarded as release by HIFU. Therefore, the HIFU triggered release capacity in Table 1 is the sum of release in phantom and wash 1. The total release capacity is the sum of the release in phantom and the release capacity in all washes. We can observe that the release capacity triggered by HIFU is 64.5%, whereas the release capacity of the control sample is 24.5% in the same timeframe, indicating the difference of 40% is contributed by the HIFU trigger. Both samples show continuous release after being rocked overnight. The total release capacity of LPMSNs with HIFU is 75.4%, and that of LPMSNs no HIFU is 35.6%, indicating the Docetaxel release is HIFU responsive. To characterize the stability of LPMSNs after the HIFU trigger, we checked the TEM images after the HIFU trigger at 50% amplitude for 2 min as shown in **Figure 6.3 (b)**. The nanoparticles stayed intact, and the pore structure was still well-defined. We also checked the DLS and the diameter after the HIFU trigger was 195.6 ± 4.5 nm, and the zeta-potential was -21.82 ± 0.58 mV, indicating the no aggregation was observed. These results indicate that LPMSNs are stable upon HIFU stimuli in our current setting.

Table 6.1 Docetaxel release capacity of different nanoparticles, HIFU parameters, and solvents.

Nano-particles	HIFU amplitude	HIFU duration (s)	Solvent	Tempera-ture	HIFU triggered release capacity	Total release capacity
LPMSNs	No HIFU		Ethanol	NA	NA	40.9%
	50%, 22 W	120	DMSO/H_2O	35 °C	64.5%	75.4%
	No HIFU		DMSO/H_2O	NA	NA	35.6%
	50%, 22 W	30	DMSO/H_2O	25 °C	55.3%	60.1%
	25%, 5.5 W	120	DMSO/H_2O	26 °C	66%	70.8%
	No HIFU		DMSO/H_2O	35 °C	NA	61.2%
	No HIFU		DMSO/H_2O	26 °C	NA	48.4%
	50%, 22 W	120	PBS/DMSO	25 °C	15.9%	19.2%

	50%, 22 W	240	PBS/DMSO	31 °C	32.0%	33.9%
LPMSNs-NH_2	50%, 22 W	120	DMSO/H_2O	36 °C	13.8%	14.3%
co-condense	No HIFU		DMSO/H_2O	NA	NA	9.0%
LPMSNs-NH_2	No HIFU		DMSO/H_2O	35 °C	NA	166.2%
post-graft	50%, 22 W	240	PBS/DMSO	NA	45.0%	56.0%

Then we test the HIFU responsive release with different amplitude and duration. Since the temperature increase of 50% HIFU amplitude for 2 min was around 15 °C, we applied a shorter duration or lower amplitude to minimize the temperature increase. With 50% amplitude (22 W) and 30 s duration, the temperature increase was around 5 °C, and with 25% (5.5 W) amplitude and 2 min (120 s) duration, the temperature increase was around 6 °C. The release results are shown in **Figure 6.3 (c)**. For the HIFU triggered release, the 50% amplitude and 30 s duration results show the HIFU triggered release capacity of 55.3%, and 25% amplitude and 2 min duration results show the HIFU triggered release capacity of 66%. We can observe that the latter parameter set leads to higher release capacity, indicating the duration instead of amplitude contributes more to the release capacity. Also, compared with the HIFU triggered release capacity of 64.5% at 50% amplitude and 2 min duration, the release capacity is at the same level, indicating with the same HIFU trigger duration, 25% amplitude is enough to trigger drug release.

In order to further explore the mechanism of HIFU responsive release, we designed the bulk heating triggered release experiments. The common mechanism of HIFU-triggered drug release is thermal and/or mechanic effect, and it is usually the synergy of both mechanisms. We tested the thermal effect by designing a bulk heating experiment. We set up the temperature of the water bath to be 35 °C and 26 °C, which were the temperature after 50% amplitude for 2 min and 25% amplitude and 2 min HIFU triggers. The release results are shown in **Figure 6.3 (d)**. Unlike the

release results with HIFU, where most of the drug was released during HIFU stimulation, the drug release in the water bath was slower: only around 20 – 40% of the drug was released when the sample tubes were merged in the water bath, and more drug was released overnight and after one day. The total release capacities of both samples were lower than that of samples at the same temperature with HIFU, indicating HIFU triggered drug release was not only from the thermal effect but also from the mechanical effect, such as turbulence in solution and vibration of drug molecules in pores caused by ultrasound.

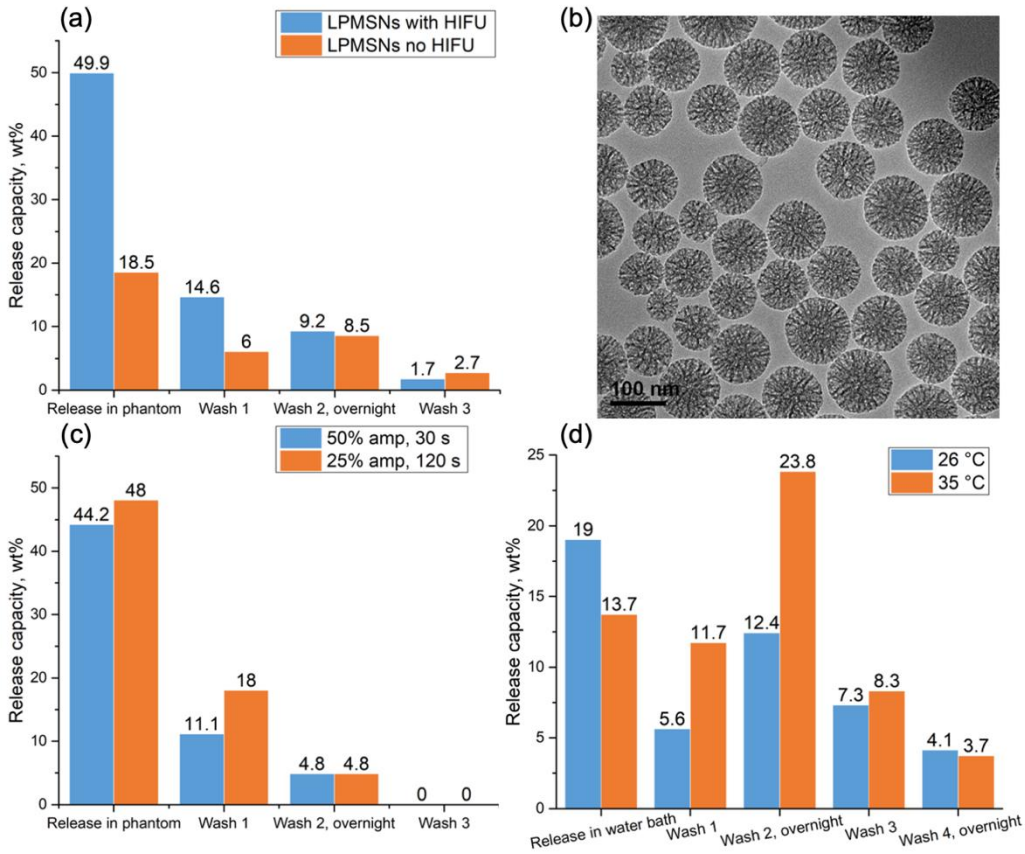

Figure 6.3 (a) Release results of Docetaxel-loaded LPMSNs treated with HIFU at 50% amplitude for 2 min in DMSO/water mixture. The total release capacity of LPMSNs with HIFU is 75.4%, and that of LPMSNs no HIFU is 35.6%; (b) TEM image of LPMSNs after HIFU triggered drug release, the morphology of nanoparticles stays intact. The scale bar is 100 nm; (c) Release results

of Docetaxel-loaded LPMSNs treated with different HIFU amplitudes and durations, the total release capacity of LPMSNs with 50% amplitude for 30 s is 60.1%, and that of LPMSNs with 25% amplitude for 2 min is 70.8%; (d) Release results of Docetaxel-loaded LPMSNs in the water bath, the total release capacity of 26 °C treatment is 48.4%, and that of 35 °C treatment is 61.2%.

To explore the influence of the amine functional group, we also test the HIFU responsive release from LPMSNs-NH_2 co-condense and post-grafting. The release results of LPMSNs-NH_2 co-condense are shown in **Figure 6.4 (a)**. With HIFU trigger at 50% amplitude for 2 min, the HIFU triggered release is 13.8%, and the total release capacity is 14.3%. The control sample without an HIFU trigger shows a total release capacity of 9.0%. The release capacity is only 19% of the LPMSNs release capacity at the same HIFU amplitude and duration. The TEM image after HIFU is shown in **Figure 6.4 (b)**. In the field of view, more than 50% of the nanoparticles were fragmented, and they formed a silica film with a dimension of hundreds of nanometers. The DLS result after the HIFU trigger matches our observation in TEM: the hydrodynamic diameter is 812.3 ± 12.3 nm, indicating severe aggregation as a result of fragmentation and re-condensation. The zeta-potential after HIFU was -0.93 ± 0.81 mV, indicating the overall surface charge was neutral. It is possible that the positively charged amine groups and negatively charged silanol groups on fragments attract each other and form the aggregation, so the overall charge is neutralized. To further investigate the stability of LPMSNs-NH_2 co-condense, we checked the TEM images after the HIFU trigger with a lower amplitude (25%) for 2 min in water. As shown in **Figure 6.4 (c)**, fragmentation can still be observed, but the ratio of fragmented nanoparticles in the field of view was below 50%. It indicates that with lower HIFU amplitude, fewer nanoparticles are fragmented, but the overall stability of these nanoparticles is not good enough for further HIFU study. Therefore, we do not use it in the following HIFU triggered drug release study.

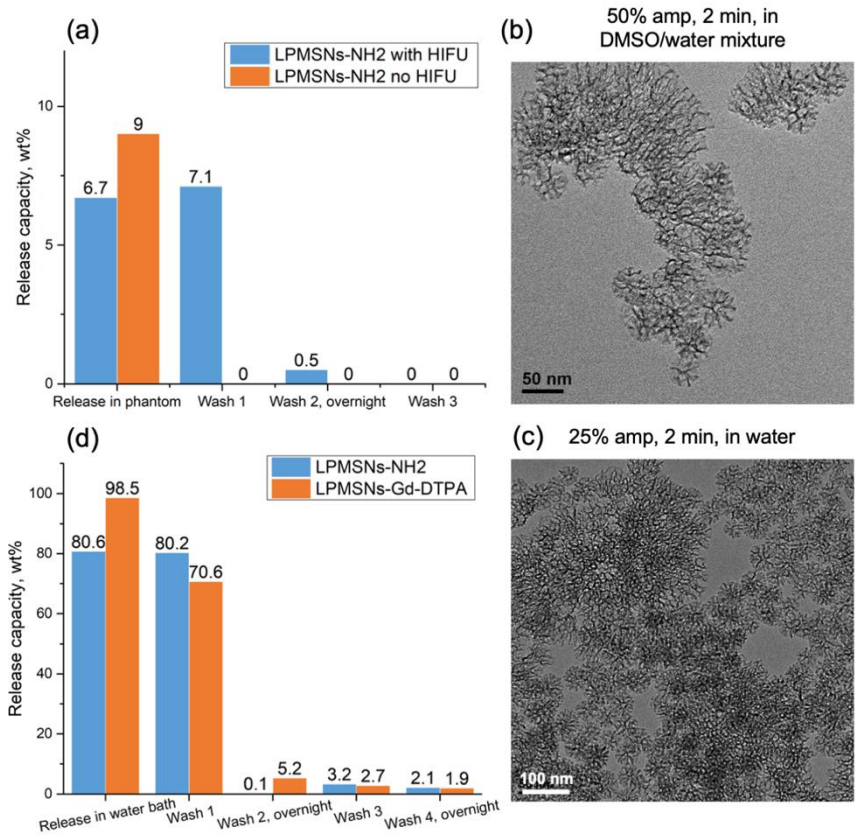

Figure 6.4 (a) Release results of Docetaxel-loaded LPMSNs-NH_2 co-condense treated with HIFU at 50% amplitude for 2 min in DMSO/water mixture. The total release capacity of LPMSNs with HIFU is 14.3%, and that of LPMSNs no HIFU is 9.0%; (b) – (c) TEM images of LPMSNs-NH_2 co-condense after HIFU at different levels, the nanoparticles are fragmented; (d) Release results of Docetaxel-loaded LPMSNs-NH_2 post-graft and LPMSNs-Gd-DTPA in 35°C water bath for 5 min in DMSO/water mixture, the total release capacity is 166.2% and 178.9%.

The release results of LPMSNs-NH_2 post-grafting are shown in **Figure 6.4 (d)**. Immersed in a 35 °C water bath for 5 min, it shows a release capacity of 160.8% and a total release capacity of 166.2%. The release capacity is almost doubled compared to that of LPMSNs. The LPMSNs-NH_2 post-graft was further derivatize with Gd-DTPA by EDC/NHS reaction, so that the nanoparticles will have T_1 contrast in MRI. The Docetaxel release results of LPMSNs modified with Gd-DTPA

(LPMSNs-Gd-DTPA) after immersing in a 35 °C water bath for 5 min is shown in **Figure 6.4 (d)**. It shows a release capacity of 169.1% and a total release capacity of 178.9%. The over 100% release capacity indicates higher loading capacity, since the ratio of nanoparticles to drug is 1:2, so the maximum loading and release capacity is 200%.

Next, we test the HIFU responsive release in biologically relevant media. We choose PBS with 2.5 vol% DMSO as the release media, because PBS is an aqueous buffer at the physiological pH value, and 2.5 wt% DMSO can dissolve the released Docetaxel so that we can quantify it in the supernatant. **Figure 6.5 (a)** shows the release results of LPMSNs loaded with Docetaxel. Triggered by HIFU at 50% amplitude for 2 min, the release capacity is 15.9%, and the total release capacity is 19.2%. The TEM image shown in **Figure 6.5 (b)** shows the nanoparticles stay intact after HIFU. The control sample does not show any release in phantom, and the total release capacity is 2.5%. It indicates that the nanoparticles show no premature drug release in the phantom, and with a HIFU trigger, Docetaxel can be released in biologically relevant media.

To further increase the release capacity, we double the HIFU trigger time to 4 min based on our previous finding that a longer duration can help increase release capacity. To prevent overheating, we leave a 1 min interval after 2 min HIFU. On the TEM image after HIFU shown in **Figure 6.5 (c)**, we observe that most of the nanoparticles stay intact after the HIFU trigger, but there are around 5% of nanoparticles in the field of view are fragmented as labeled with red arrows. It may be because the HIFU duration is too long. As shown in **Figure 6.5 (d)**, the HIFU triggered release for LPMSNs is 32.0%, and the total release capacity is 33.9%. We also test the Docetaxel release from LPMSNs-NH_2 post-graft under the same condition, and as shown in **Figure 6.5 (d)**, the HIFU triggered release is 45.0%, and the total release capacity is 56.0%, which is higher than the release capacity of LPMSNs. Compared with TEM image before HIFU shown in **Figure 6.5**

(e), we also observe around 5% of nanoparticles in the field of view are fragmented as shown in **Figure 6.5 (f)** labeled with red arrows. These results indicate that although a longer HIFU duration causes higher release capacity, the nanoparticles tend to degrade. Therefore, when choosing the HIFU parameter, we need to consider the tradeoff between the drug release capacity and nanoparticle integrity.

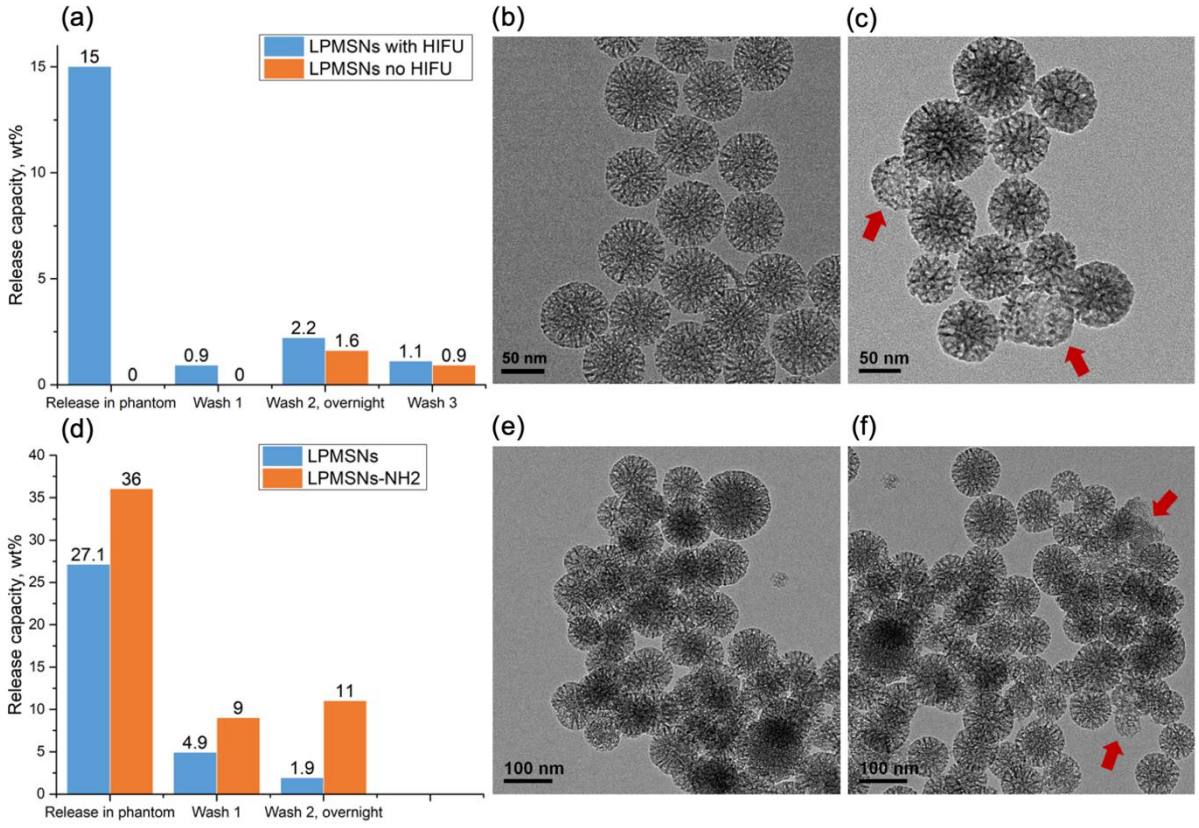

Figure 6.5 (a) Release results of Docetaxel-loaded LPMSNs treated with HIFU at 50% amplitude for 2 min in PBS, the nanoparticles triggered with HIFU shows a total release capacity of 19.2%, and the no HIFU control shows a total release capacity of 2.5%; (b) TEM image after Docetaxel-loaded LPMSNs was treated with HIFU at 50% amplitude for 2 min in PBS; (c) TEM image after Docetaxel-loaded LPMSNs was treated with HIFU at 50% amplitude for 4 min in PBS, the fragmented nanoparticles are labeled with red arrows; (d) Release results of Docetaxel-loaded LPMSNs and LPMSNs-NH_2 post-graft with HIFU at 50% amplitude for 4 min in PBS, the total

release capacity is 33.9% and 56.0%; (e) TEM image of LPMSNs-NH_2 post-graft with Docetaxel loaded before HIFU; (f) TEM image of LPMSNs-NH_2 post-graft after HIFU at 50% amplitude for 4 min in PBS, the fragmented nanoparticles are labeled with red arrows.

To further characterize the pore structure of LPMSNs with and without amine functionalization and before and after drug loading, we use nitrogen absorbtion and desorbtion and BET to characterize these four samples. The isotherm and pore size distribution results are shown in **Figure 6.6**. From the isotherm, we can observe the capillary condensation at higher pressures is weaken after drug loading. From the pore size distribution, we can observe that pore size is around 5 – 10 nm, which matches the TEM observation. The pore size decreases 2 – 3 nm after drug loading, indicating the drug crystallizes or precipitates inside the pores. From the calculated BET surface area shown in **Table 6.2**, all of the samples have surface areas above 200 m^2/g, which is much less than our regular MSNs with 2 nm pores (usually around 1000 m^2/g). It matches the fact that nanoparticles with larger pore have smaller surface area compared to nanoparticles at the same dimension with smaller pores. Loaded with drugs and/or amine functionalization, the surface area further decreases by around 10%. We also calculate the pore volume of the pores under 20 nm in size so that we can avoid calculating the volume between nanoparticles. As shown in **Table 6.2**, all of the samples have pore volume around 0.4 cc/g, which is much less than our regular MSNs with 2 nm pores (usually 1 cc/g). With drug loading and/or amine functionalization, the pore volume decrease is less than 20%. The subtle decrease in surface area and pore volume also suggests no large crystals/precipitates blocking the pore opening or between the samples, otherwise we will observe a much larger decrease in surface area and pore volume (usually around 50% – 3 times based on our experiences).

Table 6.2 BET surface area and pore volume of LPMSNs and derivatives.

	BET surface area m^2/g,	Pore volume, cc/g
LPMSNs	279.147	0.44
LPMSNs, Docetaxel loaded	249.206	0.41
LPMSNs-NH_2	257.885	0.43
LPMSNs-NH_2, Docetaxel loaded	226.346	0.35

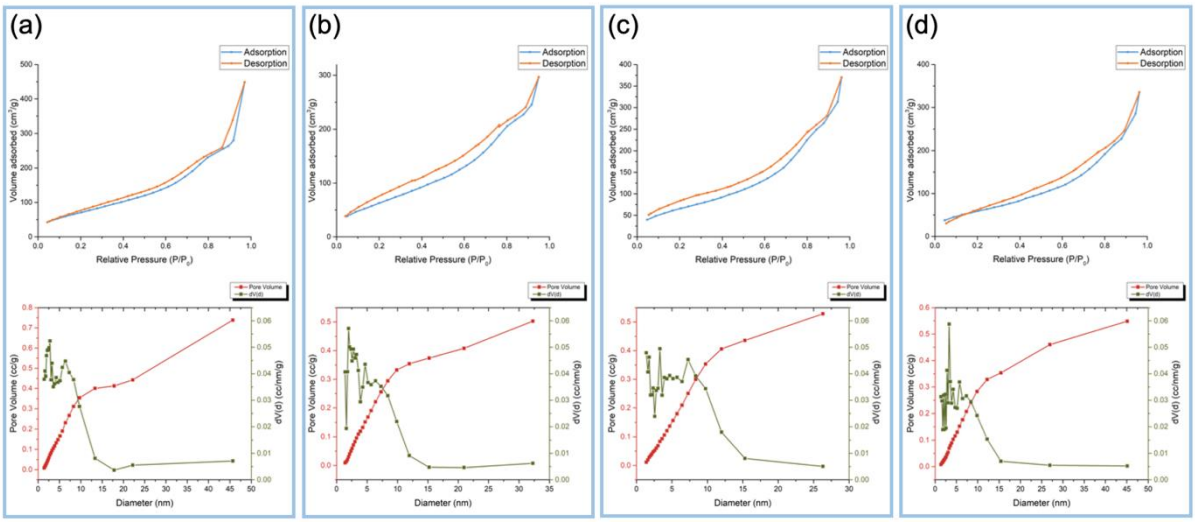

Figure 6.6 Isotherms and pore size distributions of (a) LPMSNs; (b) LPMSNs loaded with Docetaxel; (c) LPMSNs-NH_2 post-graft; (d) LPMSNs-NH_2 post-graft loaded with Docetaxel.

6.3 Conclusions

In this work, we successfully synthesized LPMSNs that have diameters around 100 nm and pore sizes of 8 – 10 nm. Two methods were used to functionalize them with amine groups and the post-grafting method was shown to be better since it realized higher drug loading and release capacity and better stability after HIFU trigger. Using the solvent evaporation method, we were able to load a hydrophobic drug, Docetaxel, into the pores, and good dispersibility of the nanoparticle remained in aqueous media. With the HIFU trigger with various parameters, a release

capacity of 60 – 166 wt% in DMSO/water mixture was realized, and a higher release capacity compared to the control samples without an HIFU trigger was demonstrated. In a biological relevant solvent, the release capacity of 56 % was realized with HIFU trigger at 50% amplitude and 4 min from LPMSNs-NH_2 post-graft. Without HIFU, little pre-mature release was observed in the HIFU trigger timeframe. The systematic study of LPMSNs synthesis and HIFU triggered release conditions and parameters will help the study of hydrophobic drug delivery *in vitro* and *in vivo* in the near future.

6.4 Experimental Section

Chemicals

Chemical reagents were purchased from Sigma-Aldrich, Alfa Aesar, Fisher Scientific, or Acros Organics and used without purification unless noted otherwise. Tetraethylorthosilicate (TEOS; 99%, Aldrich), cetyltrimethylammonium bromide (CTAB; 98%, Aldrich), sodium hydroxide (99%, Fisher Scientific), ethanol (200 proof, Aldrich). 3-aminopropyl triethoxysilane (APTES; 99%, Aldrich), EDC•HCl (99%, Covachem), sulfo-NHS (99%, Covachem), diethylenetriaminepentaacetic acid gadolinium(III) dihydrogen salt hydrate (Gd-DTPA; 97%, Aldrich), hydrochloric acid (Fisher Scientific), Docetaxel (InvivoChem), Dimethyl sulfoxide (DMSO; 99%, Fisher), Phosphate-buffered saline (PBS; Sigma, pH = 7.4), 1,3,5-trimethylbenzene (TMB, mesitylene; 98%, Aldrich). Anhydrous toluene was obtained by distillation from CaH_2 under dry nitrogen.

LPMSNs synthesis

200 mg CTAB was add into 50 mL DI water in a 100 mL round-bottom flask, then dissolved by warming up the flask on top of a hotplate. Then 1220 μL TMB was added into the CTAB solution, and was sonicated in water bath for 30 min. The emulsion was milk-like after sonication.

Then the flask was placed in the oil bath at 85 °C, and 50 μL NaOH and 224 μL 100 mg/mL NH_4Cl were added. After stabilizing for 10 min, 750 μL TEOS was added drop by drop, and reacted for 2 h. After the reaction was complete, the solution was cooled down to room temperature, and centrifuged to collect the nanoparticles. Before doing the centrifuge, 20 mL ethanol was added to 20 mL solution, so it was easier to spin the nanoparticles down. Wash 3 times using 35×3 mL ethanol. The yield for each batch was around 30 – 50 mg.

LPMSNs-NH_2 co-condense synthesis

200 mg CTAB was add into 50 mL DI water in a 100 mL round-bottom flask, then dissolved by warming up the flask on top of a hotplate. Then 1220 μL TMB was added into the CTAB solution, and was sonicated in water bath for 30 min. The emulsion was milk-like after sonication. Then the flask was placed in the oil bath at 85 °C, and 50 μL NaOH and 224 μL 100 mg/mL NH_4Cl were added. 712 μL TEOS was mix with 38 μL APTES. After stabilizing for 10 min, 750 μL TEOS was added drop by drop, and reacted for 2 h. After the reaction was complete, the solution was cooled down to room temperature, and centrifuged to collect the nanoparticles. Before doing the centrifuge, 20 mL ethanol was added to 20 mL solution, so it was easier to spin the nanoparticles down. Wash 3 times using 35×3 mL ethanol. The yield for each batch was around 50 mg.

CTAB extraction

After LPMSNs or LPMSNs-NH_2 co-condense were synthesized and washed, one batch of nanoparticles was dispersed in 50 mL ethanol. 3 mL 12 M HCl was added and refluxed at 85 °C for 1 h. Then the nanoparticles were spun down and redispersed in 50 mL ethanol. 3 mL 12 M HCl was added and reflux at 85 °C for overnight. After the reaction was done, the nanoparticles were washed with 35×3 mL ethanol 3 times.

LPMSNs-NH_2 post-graft

One batch of LPMSNs after CTAB extraction was used and wash it with 30 mL toluene 3 times. Then the nanoparticles were dispersed in 20 mL toluene and 30 μL APTES was added. Reflux overnight at 110 °C with N_2 protection. After the reaction was done, the nanoparticles were washed with 35×3 mL ethanol 3 times.

LPMSNs-Gd-DTPA

20 μL Gd-DTPA solution (0.10 g/mL) was added to 0.5 mL MES buffer (pH = 6.0). After mixing, 5 mg EDC and 2 mg Sulfo-NHS was added. The solution was stirred for 20 min at room temperature. 10 mg of LPMSNs-NH_2 post-graft was dispersed in 4 mL HEPES buffer (pH = 7.4). Then the Gd-DTPA solution was mixed with nanoparticles and reacted at room temperature for 24 h. Then the nanoparticles were collected and washed with DI water 3 times.

Material Characterizations

The size and morphology of MSNs were investigated by transmission electron microscopy (TEM, Tecnai T12). The N_2 adsorption-desorption isotherms of MSNs were obtained at liquid N2 temperature (77K) on a Autosorb-iQ (Quantachrome Instruments) apparatus. MSNs were degassed at 110 °C overnight before the measurement. The surface area and pore size distribution of MSNs were determined by Brunauer-Emmett-Teller (BET) and Barrett- Joyner-Halenda (BJH) methods. The dynamic light scattering (DLS) size and zeta potential of MSNs were measured by a laser particle analyzer LPA-3100 at room temperature.

Docetaxel loading into nanoparticles

Nanoparticles was dispersed in ethanol at 2 mg/mL, and Docetaxel was dissolved at 10 mg/mL in ethanol. Nanoparticles and Docetaxel were mixed at the weight ratio of 1:1 in ethanol (for LPMSNs-NH_2 post-graft and LPMSNs-Gd-DTPA, the ratio is 1:2). The solution was stirred

for 2 days until only 10% solution volume was remained. The nanoparticles were spun down and the supernatant was disposed, then the nanoparticles were washed 3 times with DI water.

Docetaxel release from nanoparticles using ethanol

2 mg drug-loaded nanoparticles were dispersed in 1.5 mL ethanol and were rocked overnight at room temperature. Then the nanoparticles were spun down and the supernatant was collected. The nanoparticles were washed twice with 1.5 mL ethanol and the supernatant was collected.

Docetaxel release in DMSO/water mixture under HIFU trigger

2 mg nanoparticles loaded with Docetaxel was dispersed in 0.75 mL water and mixed with 0.75 mL DMSO right before the HIFU experiment. Then the nanoparticles in DMSO/water mixture were added to the agarose phantom and placed above the HIFU transducer. After treated with HIFU, the mixture after HIFU was collected and spun down and the supernatant was collected. Then the nanoparticles were washed 3 times using 1.5 mL DMSO/water mixture, including 1 wash immediately after HIFU, 1 wash by rocking overnight, and 1 wash immediately after rocking overnight. For the control sample, the nanoparticle concentration and treatment were exactly the same except the control sample was not treated by HIFU. It was mixed with DMSO, placed in its individual agarose phantom, and collected at the same time as the HIFU treated sample, and undergoes the same wash steps.

Docetaxel release in PBS/DMSO under HIFU trigger

PBS was mixed with 2.5 vol% DMSO. 2 mg nanoparticles loaded with Docetaxel were dispersed in 1.5 mL PBS/DMSO solution right before the HIFU experiment. Then the nanoparticles in PBS/DMSO mixture were added to the agarose phantom and placed above the HIFU transducer. After treated with HIFU, the mixture after HIFU was collected and spun down and the supernatant was collected. Then the nanoparticles were washed 2 times using 1.5 mL

PBS/DMSO mixture, including 1 wash immediately after HIFU, 1 wash by rocking overnight. Collect the supernatant of all wash. For the control sample, the nanoparticle concentration and treatment were exactly the same except the control sample was not treated by HIFU.

Quantify Docetaxel concentration using UV-Vis plate reader

Docetaxel concentration was quantified with the SpectraMax Plus 384 Microplate Reader by Molecular Devices. The standard curves in different solvents and wavelengths are shown in **Figure 6.7**. 0.3 mL supernatant was added in each well in a 96-well plate, and the absorbance was measured the under the end point mode. For Docetaxel in ethanol, the absorbance was measured at 290 nm, and the concentration was calculated using the calibration curve in **Figure 6.7 (a)**. For Docetaxel in DMSO/water mixture and PBS/DMSO mixture, the absorbance was measured at 310 nm, and the concentration is calculated using the calibration curve in **Figure 6.7 (b)** and **(c)**.

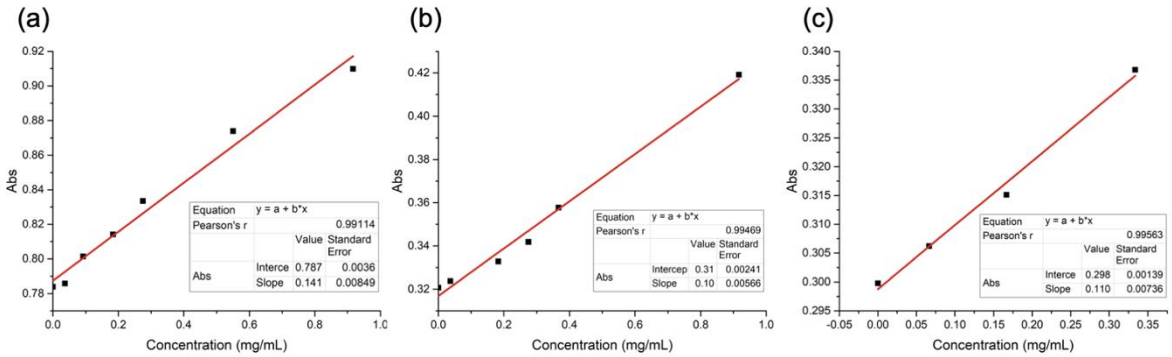

Figure 6.7 Calibration curve of Docetaxel in different solvents and wavelength (a) ethanol at 290 nm; (b) DMSO/water mixture at 310 nm; (c) PBS/DMSO mixture at 310 nm.

6.5 References

(1) Kalepu, S.; Nekkanti, V. Insoluble Drug Delivery Strategies: Review of Recent Advances and Business Prospects. *Acta Pharm. Sin. B* **2015**, *5*, 442–453.

(2) Okamoto, Y.; Taguchi, K.; Sakuragi, M.; Imoto, S.; Yamasaki, K.; Otagiri, M. *In Vivo* Drug Delivery Efficiency of Albumin-Encapsulated Liposomes as Hydrophobic Drug Carriers. *J.*

Drug Deliv. Sci. Technol. **2018**, *47*, 62–66.

(3) Hardiansyah, A.; Yang, M. C.; Liu, T. Y.; Kuo, C. Y.; Huang, L. Y.; Chan, T. Y. Hydrophobic Drug-Loaded PEGylated Magnetic Liposomes for Drug-Controlled Release. *Nanoscale Res. Lett.* **2017**, *12*.

(4) Li, Z.; Johnson, L. M.; Ricarte, R. G.; Yao, L. J.; Hillmyer, M. A.; Bates, F. S.; Lodge, T. P. Enhanced Performance of Blended Polymer Excipients in Delivering a Hydrophobic Drug through the Synergistic Action of Micelles and HPMCAS. *Langmuir* **2017**, *33*, 2837–2848.

(5) Li, C.; Chen, R.; Xu, M.; Qiao, J.; Yan, L.; Guo, X. D. Hyaluronic Acid Modified Mpeg-b-Pae Block Copolymer Aqueous Micelles for Efficient Ophthalmic Drug Delivery of Hydrophobic Genistein. *Drug Deliv.* **2018**, *25*, 1258–1265.

(6) Larrañeta, E.; Stewart, S.; Ervine, M.; Al-Kasasbeh, R.; Donnelly, R. F. Hydrogels for Hydrophobic Drug Delivery. Classification, Synthesis and Applications. *J. Funct. Biomater.* **2018**, *9*, 13.

(7) Gou, M. L.; Li, X. Y.; Dai, M.; Gong, C. Y.; Wang, X. H.; Xie, Y.; Deng, H. X.; Chen, L. J.; Zhao, X.; Qian, Z. Y.; Wei, Y. Q. A Novel Injectable Local Hydrophobic Drug Delivery System: Biodegradable Nanoparticles in Thermo-Sensitive Hydrogel. *Int. J. Pharm.* **2008**, *359*, 228–233.

(8) Yang, G.; Liu, Y.; Wang, H.; Wilson, R.; Hui, Y.; Yu, L.; Wibowo, D.; Zhang, C.; Whittaker, A. K.; Middelberg, A. P. J. Bioinspired Core–Shell Nanoparticles for Hydrophobic Drug Delivery. *Angew. Chemie* **2019**, *131*, 14495–14502.

(9) Banerjee, S. S.; Chen, D.-H. Magnetic Nanoparticles Grafted with Cyclodextrin for Hydrophobic Drug Delivery. *Chem. Mater.* **2007**, *19*, 6345–6349.

(10) Shubhra, Q. T. H.; Tóth, J.; Gyenis, J.; Feczkó, T. Poloxamers for Surface Modification of Hydrophobic Drug Carriers and Their Effects on Drug Delivery. *Polym. Rev.* **2014**, *54*, 112–138.

(11) Ferris, D. P.; Lu, J.; Gothard, C.; Yanes, R.; Thomas, C. R.; Olsen, J. C.; Stoddart, J. F.; Tamanoi, F.; Zink, J. I. Synthesis of Biomolecule-Modified Mesoporous Silica Nanoparticles for Targeted Hydrophobic Drug Delivery to Cancer Cells. *Small* **2011**, *7*, 1816–1826.

(12) Cheng, C.-A.; Chen, W.; Zhang, L.; Wu, H. H.; Zink, J. I. Magnetic Resonance Imaging of High-Intensity Focused Ultrasound-Stimulated Drug Release from a Self-Reporting Core@ Shell Nanoparticle Platform. *Chem. Commun.* **2020**, *56*, 10297–10300.

(13) Zhang, S.; Qian, X.; Zhang, L.; Peng, W.; Chen, Y. Composition–Property Relationships in Multifunctional Hollow Mesoporous Carbon Nanosystems for PH-Responsive Magnetic Resonance Imaging and on-Demand Drug Release. *Nanoscale* **2015**, *7*, 7632–7643.

(14) Li, X.; Xie, C.; Xia, H.; Wang, Z. PH and Ultrasound Dual-Responsive Polydopamine-Coated Mesoporous Silica Nanoparticles for Controlled Drug Delivery. *Langmuir* **2018**, *34*, 9974–9981.

(15) Cheng, C. A.; Chen, W.; Zhang, L.; Wu, H. H.; Zink, J. I. A Responsive Mesoporous Silica Nanoparticle Platform for Magnetic Resonance Imaging-Guided High-Intensity Focused Ultrasound-Stimulated Cargo Delivery with Controllable Location, Time, and Dose. *J. Am. Chem. Soc.* **2019**, *141*, 17670–17684.

(16) Li, X.; Wang, Z.; Xia, H. Ultrasound Reversible Response Nanocarrier Based on Sodium Alginate Modified Mesoporous Silica Nanoparticles. *Front. Chem.* **2019**, *7*.

(17) Liu, J.; Detrembleur, C.; Mornet, S.; Jérôme, C.; Duguet, E. Design of Hybrid Nanovehicles

for Remotely Triggered Drug Release: An Overview. *J. Mater. Chem. B* **2015**, *3*, 6117–6147.

(18) Li, G.; Wang, Y.; Wang, S.; Jiang, J. A Tough Composite Hydrogel Can Controllably Deliver Hydrophobic Drugs under Ultrasound. *Macromol. Mater. Eng.* **2018**, *303*, 1–6.

(19) Charalambous, A.; Mico, V.; McVeigh, L. E.; Marston, G.; Ingram, N.; Volpato, M.; Peyman, S. A.; McLaughlan, J. R.; Wierzbicki, A.; Loadman, P. M.; Bushby, R. J.; Markham, A. F.; Evans, S. D.; Coletta, P. L. Targeted Microbubbles Carrying Lipid-Oil-Nanodroplets for Ultrasound-Triggered Delivery of the Hydrophobic Drug, Combretastatin A4. *Nanomedicine Nanotechnology, Biol. Med.* **2021**, *36*, 102401.

Chapter 7. HIFU-Stimulated Delivery of a Magnetic Resonance Image Contrast Agent Based on Mesoporous Silica Nanoparticles Functionalized with Thermo-Responsive Polymer

7.1 Introduction

Magnetic resonance imaging (MRI) has increasingly being used in clinical practice to guide therapies, and it is often used to guide high-intensity focused ultrasound (HIFU).[1–3] There have been many studies about using MRI-guided HIFU (MRIgHIFU) to realize cargo delivery.[4–6] As the demand for detailed diagnostic and therapy increases, the on-command contrast enhancement will be in need.[7] Poly(N-isopropylacrylamide) (PNIPAm) is a thermo-responsive polymer with a lower critical solution temperature (LCST) of 32 °C.[8,9] PNIPAm changes its hydrophilicity reversibly: it is hydrophilic under LCST and hydrophobic over LCST.[10] When PNIPAm is hydrophobic, the size of a single molecule will decrease by 90% due to the repulsion from surrounding water molecules.

In this work, we take advantage of the reversible hydrophobicity change of PNIPAm as a capping molecule on mesoporous silica nanoparticles (MSNs). After the PNIPAm modified MSNs are synthesized, we first explored the mechanism of the capping system and identified the best cargo loading and release conditions. Then the cargo loading condition was optimized to maximize the loading capacity of Magnevist, a commercial-available MRI contrast agent. In the MRIgHIFU experiments, the HIFU responsive cargo release performance was tested by observing the T_1 contrast change caused by cargo release.

7.2 Results and Discussions

Material synthesis and characterizations

The PNIPAm modified MSNs (PNIPAm-MSNs) were successfully synthesized and characterized. The MSNs were around 120 nm in diameter and were modified with amine group on the surface. Amine modification was done by the post synthesis grafting method, which was grafting of (3-Aminopropyl)triethoxysilane (APTES) on the MSN surface after MSNs were synthesized as shown in **Figure 7.1**.

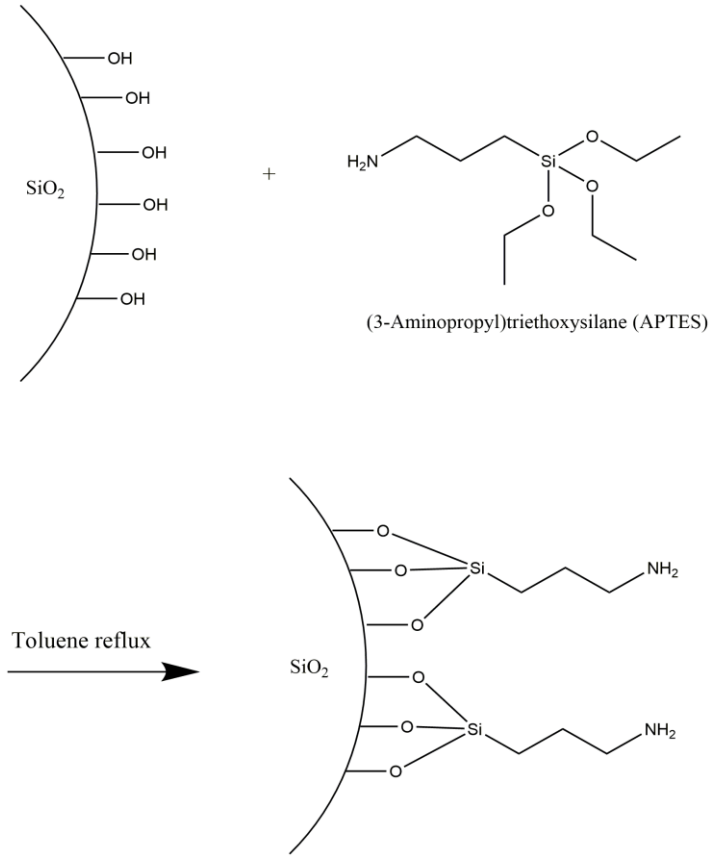

Figure 7.1 Synthesis route of post-grafting amine modification on MSNs.

PNIPAm was attached to the amine group on MSNs by the EDC/NHS reaction shown in **Figure 7.2**. TEM images in **Figure 7.3** show that the PNIPAm-MSNs stayed intact but looked blurry because of the PNIPAm modification. The DLS results shown in **Figure 7.4** show

increasing diameter indicating aggregation due to the hydrophobicity of PNIPAm above LCST. The zeta-potential of the MSNs changed from negative to positive (amine modification), then to neutral (PNIPAm-MSNs).

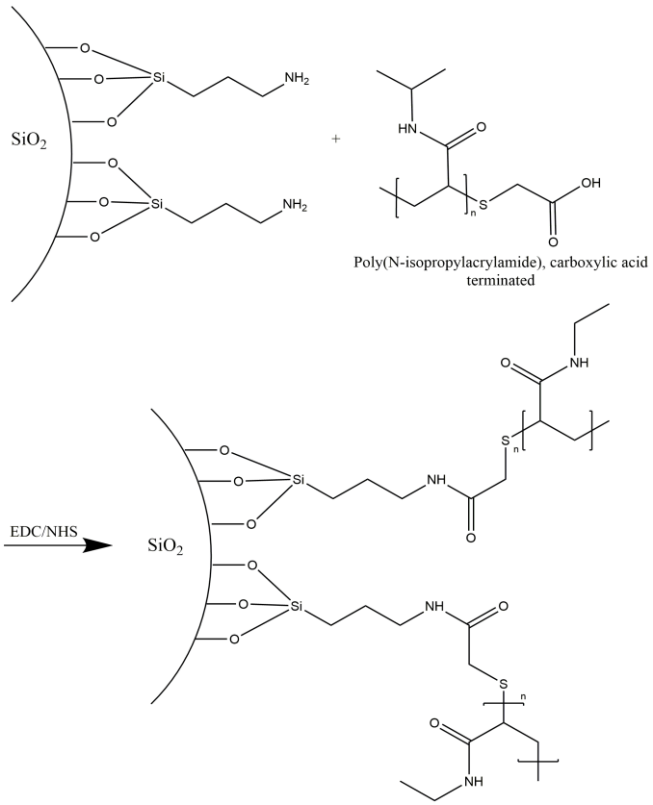

Figure 7.2 Synthesis route of PNIPAm modification on amine modified MSNs.

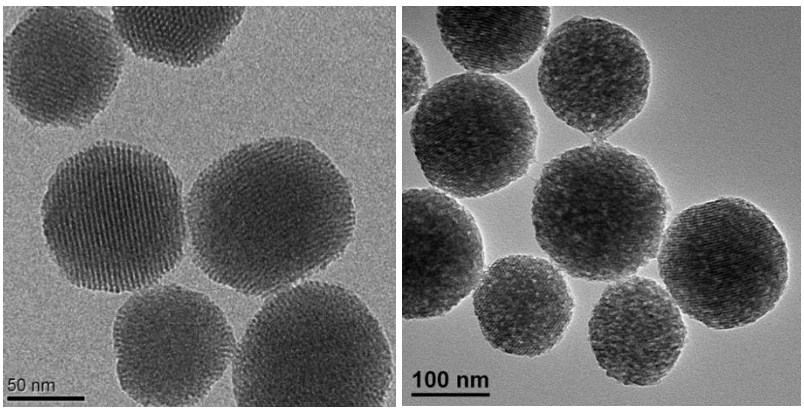

Figure 7.3 TEM images of unmodified MSNs (left) and PNIPAm-MSNs (right).

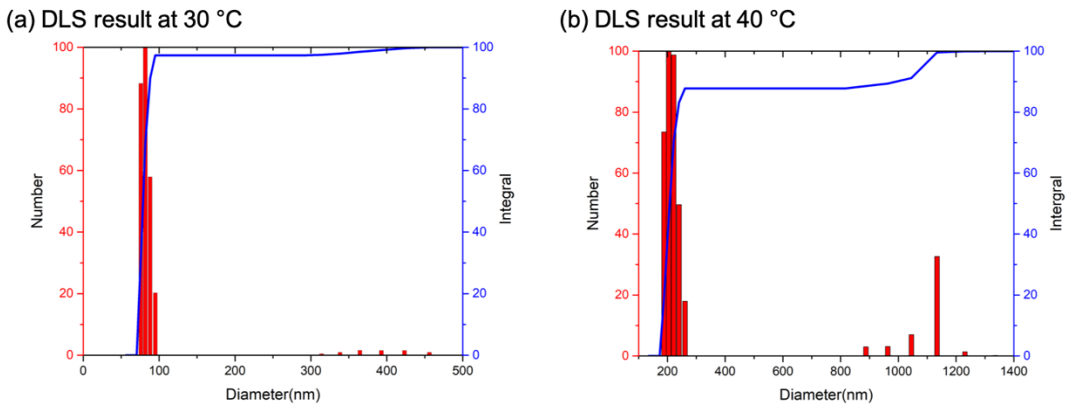

Figure 7.4 Hydrodynamic diameter distribution of PNIPAm-MSNs at different temperatures.

Mechanism exploration of PNIPAm-MSNs cargo delivery

Since the hydrophobicity change and the volume change of PNIPAm can lead to two opposite cargo delivery mechanism, two hypotheses are proposed. One hypothesis is based on the hydrophobicity change. When the temperature is above LCST, PNIPAm will become hydrophobic, and if the cargo is hydrophilic and dissolved in water, it is difficult to diffuse out of the hydrophobic PNIPAm layer. It means that the cap is closed at high temperature. At lower temperature, PNIPAm is hydrophilic, so the dissolved cargo can diffuse out of pores easily, thus the cap is open below LCST. The second hypothesis is based on the volume change of PNIPAm. When temperature increases to be above the LCST, the polymer will shrink and expose the pore opening, thus the cap is open in higher temperature. When temperature drops below the LCST, the PNIPAm is hydrophilic and swollen, so it will block the pore opening, thus close the cap at low temperature. The experiments were designed to test both hypotheses. Tris(bipyridine)ruthenium(II) chloride ($[Ru(bpy)_3]Cl_2$) was chosen to be the cargo in these experiments for the following reasons. First, it has a positive charge, so it is not attracted to MSN surfaces with positively charged modification by electrostatic interaction. Second, it has visible absorbance, which makes it easy to quantify its concentration. **Table 7.1** shows the experimental design, where RT refers to room

temperature, which is below LCST, and HC refers to cap in water bath above LCST. The aim of these experiments was to compare the loading and release capacity in each loading and release temperature. For example, if higher loading and release capacity are achieved when loading cargo at room temperature and releasing cargo at hot water bath, it will support hypothesis 1.

Table 7.1 Experimental design of the drug delivery mechanism experiments

Hypothesis	Sample name	Sample description
1	RT loading, HC (RLHC)	Load in RT, cap in hot water bath, release in RT
	RT loading, no capping (RLNC)	In RT all the time, control sample for capping
	RT blank (RB)	In RT all the time, control sample for polymer
2	Hot loading, RT capping (HLRC)	Load in hot water bath, cap by cooling down to RT, release in hot water bath
	Hot loading, no capping (HLNC)	In hot water bath all the time, control sample for capping
	Hot blank (HB)	In hot water bath all the time, control sample for polymer

The results of the experiments proposed in **Table 7.1** are shown in **Table 7.2**. The Uptake capacity% means the cargo that is taken up, which consists of cargo being loaded inside the pores, and the free cargo that sticks to the nanoparticles. The wash capacity% is the amount of cargo that is washed out, and a higher value indicates more leakage of the cargo delivery system. Loading capacity% measures the cargo that is loaded in the pores, and the release capacity% measures the cargo being released. The release% measures the percentage of the drug loaded that is released. Higher loading and release capacity and release% is the goal of the desired delivery system. According to **Table 7.2**, the HLRC sample has the highest loading capacity and release capacity,

and it means the best loading/release procedure was adopted. It can be concluded that higher temperature leads to “cap open”, because capping above LCST causes more leakage during washing, and release above LCST leads to higher release percentage. Diffusion rates under different temperature can be calibrated by 2 samples without polymer (HB and RB), and from comparing the HB and RB samples, it can be observed that HB has lower uptake and release, which means that high temperature did not lead to much higher loading and release capacity as expected. All samples with PNIPAm have similar uptake, and their uptake is higher than samples without PNIPAm, which supports that PNIPAm is functionalized as a capping molecule. We learn from these results that the volume change in PNIPAm plays a major role in the cargo delivery process: more cargo is loaded when the temperature is above LCST and PNIPAm is shrunk, and PNIPAm below LCST can cap more cargo molecule compared with that above LCST.

Table 7.2 Result of $[Ru(bpy)_3]Cl_2$ delivery experiments of PNIPAm-MSNs

Capacity%	HLRC	HLNC	HB	RLHC	RLNC	RB
Uptake	2.85%	2.73%	1.59%	2.66%	2.85%	1.85%
Wash	1.34%	2.01%	0.60%	2.33%	1.59%	1.47%
Loading	1.51%	0.72%	0.99%	0.33%	1.26%	0.38%
Release (Release%)	0.66% (43%)	0.29% (40%)	0.38% (38%)	0.07% (21%)	0.34% (27%)	0.46% (NA)

To confirm that the cargo is loaded into the pores, not in the PNIPAm layer, the following experiments were designed using Stöber silica nanoparticles (Stöber SNP). Stöber SNP is spherical, non-porous silica nanoparticle with the same functional groups on surface as the MSNs, which makes the surface modification consistent with that on MSNs. In this study, the diameter of Stöber SNP is 120 nm, which was the same as that of the MSNs we used. The same surface modification

and characterization were applied on Stöber SNP, and the delivery experiment procedure and design were the same as well. Herein, every MSNs sample has a corresponding control sample with Stöber SNP modified with PNIPAm.

The results of Stöber SNP are shown in **Table 7.3**. The loading and release procedure are the same as previous experiment with MSNs, but the loading and release is extremely low. It indicates that although the PNIPAm is grafted on the surface, it does not contribute to a significant amount of cargo loading or release. It means the MSN pores instead of the PNIPAm polymer chain contribute to most of the loading capacity.

Table 7.3 Result of $[Ru(bpy)_3]Cl_2$ loading and release experiments of Stöber SNP

Capacity%	HLRC	HLNC	HB	RLHC	RLNC	RB
Uptake	0.74%	0.68%	0.68%	0.58%	0.60%	0.47%
Wash	0.31%	0.48%	0.29%	0.38%	0.29%	0.17%
Loading	0.43%	0.20%	0.38%	0.19%	0.31%	0.30%
Release	0.04%	0	0	0	0	0

Next, the loading and release of Magnevist (Mgv) into PNIPAm-MSNs were tested. Mgv is commercially available MRI T_1 contrast agent, and it has been widely used in the clinic. Once Mgv is loaded in PNIPAm-MSNs, we can monitor the HIFU-responsive Mgv release by observing the T_1 contrast change. To confirm the cargo delivery condition with Mgv, we measured the loading and release capacity using the same loading and release conditions above. From the result shown in **Table 7.4**, “hot load, RT cap”, meaning load Mgv in the water bath above LCST and cap the pore by cooling down in room temperature, had the highest loading capacity, which matched

the previous results with $[Ru(bpy)_3]Cl_2$. Therefore, this condition was used in all following experiments for optimization.

Table 7.4 Results of Magnevist loading and release experiments using PNIPAm-MSNs

Capacity%	Hot load, RT cap	Hot load, hot cap	Hot load, no polymer	RT load, hot cap	RT load, RT cap	RT load, no polymer
Uptake	9.01%	8.40%	2.42%	7.27%	4.30%	2.79%
Wash	1.70%	2.63%	2.11%	2.77%	1.74%	1.66%
Loading	7.32%	5.77%	0.30%	4.51%	2.56%	1.12%
Release	0.055%	0.044%	0.017%	0.037%	0.065%	0.026%

Optimization of Magnevist loading capacity of PNIPAm-MSNs delivery system

In order to maximize the loading capacity of PNIPAm-MSNs, various optimization strategies were adapted. First, we tested the influence from the cargo loading and release solvent, and we used ethanol and water as solvents. The hypothesis is that the polymer volume change in different solvents is different. However, the results were similar between water and ethanol, so we kept using water as the cargo loading and release solvent.

We also tested strategies to increase the concentration of Mgv loading solution. The concentration difference is the cause of cargo diffusion, and we expect that a loading solution with higher cargo concentration will lead to higher loading capacity. **Table 7.5** shows the results of using a loading solution with 10 times and 100 times higher concentration as the one shown before. Loading capacity from 100× concentrated increased significantly, thus this concentration is used for the following two optimization methods.

We also tried to modify pore walls with more amine groups. Gd-DTPA shows negative charge at neutral pH, and amine group shows positive charge. Loading capacity may be improved

by electrostatic attraction between Gd-DTPA and amine group modified in pores. However, the loading capacity did not increase as expected (**Table 7.5**), so such modification was not adapted in the following experiments.

Finally, we tried to load Mgv before PNIPAm modification. After PNIPAm is grafted, even when the polymer is at the open state, there will still be spatial hindrance for cargo diffusion. Therefore, Mgv was loaded before PNIPAm was grafted, then PNIPAm NHS-ester was added to graft on MSN surface and cap the pore. As shown in **Table 7.5**, the loading capacity was increased as expected.

Table 7.5 Results of Mgv loading capacity optimization.

Capacity%	Before optimization	10× concentrated	100× concentrated	Amine in pores	Load before grafting
Uptake	9.01%	24.11%	71.50%	56.99%	78.24%
Wash	1.70%	13.08%	23.10%	30.39%	23.28%
Loading	7.32%	11.03%	48.41%	26.61%	54.96%

In summary, higher loading concentration and PNIPAm grafting after loading are two strategies that successfully increased Magnevist loading capacity. The optimized loading condition was used to prepare sample in the following MRI and HIFU experiments.

MRIgHIFU experiments

Figure 7.5 shows the results of the MRIgHIFU experiments. The Mgv control and PNIPAm-MSNs have the same amount of Mgv, and they are treated with HIFU at the same power (18 W) and duration (5 min). After the first HIFU, the T_1 of PNIPAm-MSNs became longer significantly, which implied the Mgv release. After the second HIFU, T_1 showed a further increase. **Figure 7.6** shows the T_1 increase% of both samples, and we can observe that after the first HIFU, the T_1

increase% are similar. After the second HIFU, PNIPAm-MSNs showed a higher T_1 increase%, which stood for further Mgv release. It indicates that the thermal effect of HIFU can open the cap on PNIPAm-MSNs and lead to cargo release, and the release dose is dependent to the HIFU dose.

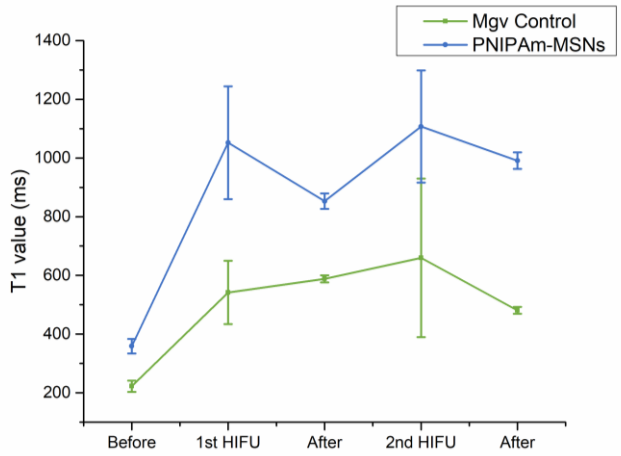

Figure 7.5 T_1 value of Mgv loaded PNIPAm-MSNs before, during and after HIFU trigger. Mgv control refers to Mgv water solution, and PNIPAm-MSNs is loaded with Mgv using the optimized method.

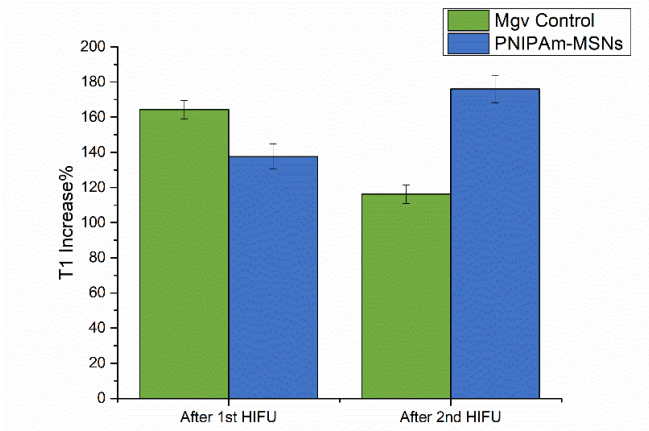

Figure 7.6 T_1 increase% of Mgv loaded PNIPAm-MSNs after the 1st and 2nd HIFU trigger. Mgv control refers to Mgv water solution, and PNIPAm-MSNs was loaded with Mgv using the optimized method.

7.3 Conclusions

The PNIPAm capped MSNs were successfully synthesized and characterized, and the mechanism of the capping system was identified from a series of cargo loading and release experiments. The volume change due to the hydrophobicity changes in PNIPAm was the key for the capping mechanism: the cap was open when the temperature was above LCST and PNIPAm was shrunk, and the cap was closed when the temperature dropped below LCST and PNIPAm was swollen. Therefore, the best cargo loading and release conditions were to load the cargo above LCST, then cap the pores and wash the nanoparticles below the LCST, followed by releasing above LCST. Then the loading capacity of Mgv was optimized by increasing its concentration in loading condition and grafting PNIPAm after Mgv loading. In the MRIgHIFU experiments, the HIFU responsive T_1 contrast change caused by cargo release was observed, and T_1 increase% of PNIPAm-MSNs was higher than Mgv control. This study would help the design of the future thermo-responsive cargo delivery system that can realize on-command delivery of MRI contrast agent.

7.4 Experimental Section

Chemicals

Tetraethylorthosilicate (TEOS; 99%, Aldrich), cetyltrimethylammonium bromide (CTAB; 98%, Aldrich), sodium hydroxide (99%, Fisher Scientific), absolute ethanol (EtOH; Aldrich). 3-aminopropyl triethoxysilane (APTES; 99%, Aldrich), poly(N-isopropylacrylamide) (PNIPAm, carboxylic acid terminated, Mn=7000, Aldrich), EDC•HCl (99%, Covachem), sulfo-NHS (99%, Covachem), , nitric acid (TraceMetal grade, Fisher), methyl cellulose (4000 cP, Sigma), agarose BP160-100 (Molecular Biology Grade, Fisher) were used as received. Anhydrous toluene was obtained by distillation from CaH_2 under dry nitrogen.

Synthesis of mesoporous silica nanoparticles (MSNs)

0.25 g of CTAB and 875 μL of sodium hydroxide solution (2 M) were dissolved in 120 mL of water under stirring. The solution was heated at 80 °C for 30 minutes, followed by the addition of 1.2 mL of TEOS and 0.79 mL of ethyl acetate under vigorous stirring. Stirring was continued for 2 h at 80 °C, and then the solution was allowed to cool to room temperature. The nanoparticles were collected by centrifugation (15 min at 7830 rpm), washed 3 times with ethanol (3×30 mL) and dispersed in 20 mL ethanol for further use. Approximately 200 mg of MSNs are collected in each batch.

Synthesis of amine modified MSNs

Around 200 mg unfunctionalized MSNs were washed twice with toluene (2x 30 mL), and redispersed in 30 mL of dry toluene stirring in a flame-dried 50 mL round bottom flask under nitrogen. Then 80 μL (3-aminopropyl)triethoxysilane (APTES) was added drop by drop and the resulting mixture was refluxed in 110 °C oil bath under nitrogen overnight. The amine-modified MSNs were collected by centrifugation (10 min at 7830 rpm) and washed 3 times with ethanol (3×30 mL). For Stöber SNP amine modification, the same procedure was followed too. The product was redispersed in 20 mL ethanol for further use.

Synthesis of PNIPAm-MSNs

160 mg amine-modified MSNs were washed in DI water for 2 times (2×20 mL) and one time in 1× PBS buffer (20 mL). They were redispersed in 5 mL PBS buffer for further use. 80 mg PNIPAm was dissolved in MES buffer and stir for 15 min, then 27.4 mg EDC and 40.9 mg NHS were added. After stiring for one hour, dispersed MSNs were added, kept stirring for 24 h, and collected by centrifugation (15 min at 7830 rpm). The nanoparticles were washed 8 times with cold DI water and centrifuged at 20 °C at all times.

Tissue mimicking gel and MRIgHIFU sample preparation

One gram of methyl cellulose was slowly added to 15 mL boiled water and stirred for 3 min. Then 25 mL condensed milk was added followed by 10 mL cold water. The mixture was stored in refrigerator overnight to eliminate air bubbles. 3 mg of PNIPAm-MSNs were dispersed in 0.5 mL water and then mixed with 1 mL gel/milk mixture, resulting a 2 mg/mL PNIPAm-MSNs gel/milk mixture. The Mgv control was made by a similar method. Mgv was first diluted to 0.5 mL water, then was mixed with 1 mL gel/milk mixture.

Agarose Phantom

17.5 g of agarose was slowly added to hot water with stirring. Then the solution was heated up to boiling, and then poured to sample holder mold. After agarose was solidified under room temperature, it was stored in a refrigerator for further use.

Characterization

Transmission electron microscopy (TEM) images were recorded on a Tecnai T12 Quick CryoEM at an accelerating voltage of 120 kV. A suspension (8 μL) of nanoparticles in ethanol was dropped on a 200-mesh carbon coated copper grid and the solvent was allowed to evaporate at room temperature.

Zeta-potential analysis and DLS were carried out on a ZetaSizer Nano (Malvern Instruments Ltd., Worcestershire, U.K.) in DI water.

ICP-OES measurements were made using ICPE-9000 Shimadzu. 0.1 mL of sodium hydroxide solution (2 M) was added to approximately 0.5-1 mg nanoparticle samples dispersed in 0.05 mL of Milli-Q water, and the mixture was sonicated for 1 h. Then 0.1 mL of nitric acid (2 M) was added, and the mixture was sonicated for 1h. The solution was then diluted to 10 mL with 2% nitric acid for measurement.

Cargo loading and release

The delivery performance experiments focus on uptake, loading and release capacity. The protocol is described as following.

(a) Load: 10 – 15 mg washed MSNs was dispersed in 1–2 mL cargo solution, stirred under desired temperature for certain amount of time. Then "cap" the delivery system by changing temperature, and trap drug inside MSNs. MSNs were centrifuged down and saved the supernatant for concentration measurement. Uptake capacity can be obtained from the **Equation 7-1** below:

$$Uptake\ capacity = \frac{(c_0 - c_1) \times V_0}{m_{MSN}} \times 100\% \quad \text{Equation 7-1}$$

$$c_0 - drug\ concentration\ before\ loading, mg/mL$$

$$c_1 - drug\ concentration\ after\ loading, mg/mL$$

$$V_0 - volume\ of\ drug\ solution, mL$$

$$m_{MSN} - weight\ of\ MSNs, mg$$

(b) Wash: MSNs were dispersed in DI water, then spun down and saved the supernatant for concentration measurement. The mentioned procedures were repeated 3–4 times or until the drug concentration in last wash supernatant reached zero. Loading capacity, which shows the amount of drug actually trapped in MSN, is calculated after this step using the **Equation 7-2** below:

$$Loading\ capacity = uptake\ capacity - \frac{\sum c_i V_i}{m_{MSN}} \times 100\% \quad \text{Equation 7-2}$$

$$c_i - drug\ concentration\ in\ wash\ solution, mg/mL$$

$$V_i - volume\ of\ wash\ solution, mL$$

(c) Release: the washed MSNs were dispersed in DI water and stirred for certain amount of time. Then MSNs were centrifuged down and saved the supernatant for concentration measurement. One or two washes were usually applied after to ensure all released drug was

collected. Release capacity is calculated using **Equation 7-3** as shown below. The concentration of $[Ru(bpy)_3]Cl_2$ and Magnevist were measured quantitatively by UV-Vis or ICP-OES.

$$Release\ capacity = \frac{c_2V_2+\sum c_iV_i}{m_{MSN}} \times 100\% \quad \text{Equation 7-3}$$

$$c_2 - drug\ concentration\ after\ release, mg/mL$$

$$V_2 - volume\ of\ release\ solution, mL$$

MRIgHIFU experiments

All MRI-guided HIFU experiments were conducted using a research-dedicated HIFU system (Image Guided Therapy, Bordeaux, France) integrated with a whole-body 3 T scanner (Prisma, Siemens Healthineers, Erlangen, Germany). The HIFU system had an 8-element annular transducer array with a diameter of 25 mm, frequency of 2.5 MHz, a focal point of 0.7×0.7×3 mm^3 in size, and a peak electrical power output of 200 W.

T_1-weighted images are acquired before and after HIFU stimulation with a 3D Cartesian gradient-echo sequence using the following parameters: field of view (FOV)=280×140×54 mm^3, matrix size=256×128×18, echo time (TE)=1.89 ms, repetition time (TR)=5 ms, flip angle=10°. T_1 relaxation times are measured before, during, and after HIFU stimulation using a Cartesian variable flip angle sequence with the following parameters: FOV=180×90×48 mm^3, matrix size=192×96×16, TE=2.29 ms, TR=6 ms, flip angles=1, 2, 5, 7 and 9°. To correct B_1+ field variations, a separate B_1 mapping protocol is run before, during, and after HIFU with matching FOV and matrix size with the T_1 mapping protocol and TE=1.87 ms, TR=2 s and flip angle=10°. These images are reconstructed in-line with the scanner software. A standard variable flip angle T_1 fitting algorithm is then carried out in an offline MATLAB 2018a (MathWorks, Natwick, MA) script to produce 3D T_1 maps. They are saved as DICOM images and imported into Horos where

regions of interest (ROIs) of 9 voxels in size are carefully drawn to exclude the thermal probe and/or air bubbles inside the heated region of the sample to compute the average T_1 value.

MSNs were dispersed in gel/milk and the mixture was placed in an agarose phantom. The power and duration of HIFU had been adjusted to 18 W and 5 min, which ensured the temperature during HIFU was at least 34 ℃, so that it is higher than LCST of PNIPAm according to the temperature mapping results.

7.5 References

(1) Hynynen, K. MRIgHIFU: A Tool for Image-Guided Therapeutics. *J. Magn. Reson. Imaging* **2011**, *34*, 482–493.

(2) Wang, Z.; Qiao, R.; Tang, N.; Lu, Z.; Wang, H.; Zhang, Z.; Xue, X.; Huang, Z.; Zhang, S.; Zhang, G.; Li, Y. Active Targeting Theranostic Iron Oxide Nanoparticles for MRI and Magnetic Resonance-Guided Focused Ultrasound Ablation of Lung Cancer. *Biomaterials* **2017**, *127*, 25–35.

(3) Fisher, D. G.; Price, R. J. Recent Advances in the Use of Focused Ultrasound for Magnetic Resonance Image-Guided Therapeutic Nanoparticle Delivery to the Central Nervous System. *Front. Pharmacol.* **2019**, *10*, 1–14.

(4) Ishida, J.; Alli, S.; Bondoc, A.; Golbourn, B.; Sabha, N.; Mikloska, K.; Krumholtz, S.; Srikanthan, D.; Fujita, N.; Luck, A. MRI-Guided Focused Ultrasound Enhances Drug Delivery in Experimental Diffuse Intrinsic Pontine Glioma. *J. Control. Release* **2021**, *330*, 1034–1045.

(5) Jain, A.; Tiwari, A.; Verma, A.; Jain, S. K. Ultrasound-Based Triggered Drug Delivery to Tumors. *Drug Deliv. Transl. Res.* **2018**, *8*, 150–164.

(6) Centelles, M. N.; Wright, M.; So, P.-W.; Amrahli, M.; Xu, X. Y.; Stebbing, J.; Miller, A.

D.; Gedroyc, W.; Thanou, M. Image-Guided Thermosensitive Liposomes for Focused Ultrasound Drug Delivery: Using NIRF-Labelled Lipids and Topotecan to Visualise the Effects of Hyperthermia in Tumours. *J. Control. Release* **2018**, *280*, 87–98.

(7) Lin, F. C.; Xie, Y.; Deng, T.; Zink, J. I. Magnetism, Ultrasound, and Light-Stimulated Mesoporous Silica Nanocarriers for Theranostics and Beyond. *J. Am. Chem. Soc.* **2021**, *143*, 6025–6036.

(8) Yu, E.; Lo, A.; Jiang, L.; Petkus, B.; Ileri, N.; Stroeve, P. Biointerfaces Improved Controlled Release of Protein from Expanded-Pore Mesoporous Silica Nanoparticles Modified with Co-Functionalized Poly (n -Isopropylacrylamide) and Poly (Ethylene Glycol) (PNIPAM-PEG). *Colloids Surfaces B Biointerfaces* **2017**, *149*, 297–300.

(9) Chang, J. H.; Kim, J.; Lee, H. PNIPAm Grafted Amino-Functionalized Mesoporous Silica for Thermo-Responsive Chromium Elimination. *Appl. Surf. Sci.* **2017**, *424*, 115–121.

(10) You, Y. Z.; Kalebaila, K. K.; Brock, S. L.; Oupický, D. Temperature-Controlled Uptake and Release in PNIPAM-Modified Porous Silica Nanoparticles. *Chem. Mater.* **2008**, *20*, 3354–3359.